| | |
|---|---|
| Title | Development and Applications of Electron Conductivity Calculation Method for Open-Shell Molecules |
| Author(s) | Nakanishi, Yasuyuki |
| Citation | 大阪大学, 2011, 博士論文 |
| Version Type | VoR |
| URL | https://hdl.handle.net/11094/27644 |
| rights | |
| Note | |

# Development and Applications of Electron Conductivity Calculation Method for Open-Shell Molecules

**Yasuyuki Nakanishi**

Department of Chemistry
Graduate School of Science
Osaka University

**2011**

# Development and Applications of Electron Conductivity Calculation Method for Open-Shell Molecules
# （開殻系分子の電気伝導計算手法の開発とその展開）

**Yasuyuki Nakanishi**

Department of Chemistry
Graduate School of Science
Osaka University

**2011**

# Acknowledgment

The present work in this thesis has been completed under the supervision of Prof. Mitsutaka Okumura at the Department of Chemistry, Graduate School of Science, Osaka University. The author would like to express sincere gratitude to him for many valuable discussions, suggestions and encouragement throughout this study. The author would like to express sincere gratitude to Dr. Yasutaka Kitagawa for many discussion, suggestions and encouragement. The author could carry out many studies through his help, and could complete this thesis. The author would like to express sincere gratitude to Dr. Takashi Kawakami for many discussion, suggestion, encouragement and the maintenance of the work station. The author could study through his daily maintenance of the work station. The author would like to express sincere gratitude to Dr. Shunsuke Yamanaka for many discussion, suggestion, encouragement.

Many thanks are given to all the members and secretaries of the quantum chemistry laboratory, Graduate School of Science, Osaka University. Especially, Mr. Toru Saito have given fruitful advice to the author. The author really appreciate your kindness. The author thanks Dr. Kazuyuki Okazaki, Mr. Isamu Shigemoto, Mr. Yusuke Kataoka, Mr. Keiji Kinoshita, Mr. Keita Kanda, Miss. Natsumi Yasuda, Mr. Akira Ito, Mr. Kohei Sakata, Mr. Kohei Tada, Dr. Satoru Yamada, Dr. Hiroshi Isobe and Mrs. Eriko Kambayashi. The author also thanks the graduate students of this laboratory, Mr. Hirotaka Yabushita, Mr. Masahide Ito, Mr. Satomichi Nishihara, Mr. Mineo Yagura and Mr. Tomohiro Watanabe.

The author was also helped by other groups. The author would like to express sincere gratitude to Assoc. Prof. Yasuteru Shigeta and Dr. Toru Matsui at the Division of Chemical Engineering, Department of Materials Engineering Science, Graduate School of Engineering Science, Osaka University. They gave many advices, suggestions and encouragement to the author. Without their help, this thesis could not be completed.

The author has been supported by the Global COE (center of excellence) Program "Global Education and Research Center for Bio-Environment Chemistry" of Osaka University.

Finally, the author would like to express sincere gratitude to the author's family.

# Contents

# Part I

# General Introduction

# Chapter 1

# General Introduction

Interest in molecular devices has been increasing over the past few decades since Aviram and Ratner proposed the first molecular-based diode in 1974 [1]. Metal-molecule-metal junctions are being investigated for their application as key elements in future nano-electronics. Owing to synthetic techniques and the development of measuring techniques, it is now possible to measure current flow though single molecules attached between two electrodes. Mechanically controlled break junction (MCBJ) [2, 3] and scanning tunneling microscope (STM) [4–6] techniques have been widely used to measure the current flow of the metal-molecule-metal junctions. Electron conductivity in the synthesized organic single molecules as benzene-dithiol (BDT) and its derivative molecules have been reported by using the MCBJ and the STM approaches.

The spin degree of freedom of the electron has attracted much attention in a spintronics, which is a coexistence of localized spins and conduction electrons. It is well known that tetrathiafulvalene (TTF) derivatives containing redox active $\pi$ electrons show the electron conductivity. If such molecules can be combined with localized spin species, one will obtain coexistent systems of localized spins and conduction electrons. The electron conductivity of the extended metal atom chains (EMAC) complexes containing various organic inorganic compounds was reported by Peng et al. [8]. In this complexes, the metal atoms arrange linearly, so that it is expected to the candidates for the molecular wire.

There are not only the reports of the synthesized molecules but also the reports of the biological molecules as the deoxyribonucleic acid (DNA). DNA consists of polymeric nucleotides. The nucleotides are composed of a deoxyribose, a phosphate and a nucleobase i. e. adenine (A), thymine (T), cytosine (C) and guanine (G). The DNA double helix is made from complementary base paring called Watson-Crick base pairing and stabilized by $\pi$-$\pi$ stacking interaction between adjacent base pairs. Therefore, utilizing the $\pi$-$\pi$ stacking interaction, we can flow the current though the DNA .The breakthrough is the report of the photoinduced long-range electron transfer through DNA proposed by Barton et al. [9]. In order to utilize DNA for the molecular wire, a large number of studies on the mechanism of the electron transfer in DNA molecule have been reported [9–19]. However, little is known about whether DNA is a conductor or not.

Tanaka et al. and Clever et al. succeed in synthesis of a novel DNA containing the metal ions [20, 21]. This novel DNA is called artificial metal-DNA (M-DNA). It is expected the realization of the spintronics materials by DNA because M-DNA contains the spin sites. The magnetism of the M-DNA have been reported by several groups, but the electron conductivity have not been reported. Wagenknecht states the importance of the artificial M-DNA as the follow [22]. The formation of a magnetic chain by the self-assembled alignment of metal centers within a DNA-like double helix is of great importance to the field of nanotechnology as it provides the basis for novel nanodevices such as semiconductors, molecular magnets, and wires.

In this sense, the importance of the electron conductivity of the molecules containing the spins increases in recent years. Theoretical studies of the electron conductivity in the closed-shell systems have enough reports. However, there are almost no theoretical reports of the electron conductivity in the open-shell systems.

The aim of this thesis is development and applications of the electron conductivity calculation method for open-shell molecules. Especially, I focus on the investigation of the electron conductivity in the artificial M-DNA, because the conductivity has never reported, so that it is interesting from the scientific viewpoints.

This thesis consists of five parts. In part II, I describe the theoretical background of the quantum chemistry and quantum transport. In part III, I describe the development the electron conductivity calculation method in the open-shell molecules. In part IV, I describe the application of the developed method to the benzene-dithiol molecules and the artificial M-DNA. In part V, I describe the magnetism of the artificial M-DNA because the magnetism of the artificial M-DNA has been reported by Tanaka et al. [20]. Finally, in part VI I describe the general conclusion of this thesis.

# Part II

# Theoretical Background

# Chapter 2

# Quantum Chemisty

*"From all we have learnt about the structure of living matter, we must be prepared to find it working in a manner that cannot be reduced to the ordinary laws of physics. And that not on the ground that there is any 'new force' or what not, directing the behavior of the single atoms within a living organism, but because the construction is different from anything we have yet tested in the physical laboratory."*
*— Erwin Schrödinger*

In order to investigate the physical properties of matter in theory, Schrödinger suggested the fundamental equation. Thereafter, the equation is called Schrödinger equation. The solutions to the Schrödinger equation are called *wave functions.* We will understand that a wave function gives a complete quantum-mechanical description of any system. Solving the Schrödinger equation for the two-body system like hydrogen atom, we can give a strict solution to the system. However, we cannot solve the equation for many-body problem, which is the problem for three or more interacting bodies. Much of the matter existing in our earth is the many-body system, so that it is difficult to understand the physical properties of the matter. Therefore, many alternative methods have been presented to answer the issue. The well-known and important alternative methods are *Hartree-Fock* and *Density Functional* methods. In the following sections, I will survey those methods.

## 2.1 Hartree-Fock Theory

The Hartree-Fock theory is the standard first approximation for all atomic and molecular calculations in modern quantum chemistry. So far various theories based on the Hartree-Fock theory has developed and we can easily calculate the physical properties of molecules by utilizing the appropriate theories for investigating the information of the molecules, because there are a number of commercial and even free computer programs available. In this section I summarize the main results obtained in a derivation of the Hartree-Fock equation [23].

### 2.1.1 Hartree-Fock Equations

The Hamiltonian operator for an $N$-electron molecule in the field of $M$ point charges in the Born-Oppenheimer approximation is given by

$$\hat{H} = -\frac{1}{2}\sum_{i=1}^{N}\nabla_i^2 - \sum_{i=1}^{N}\sum_{A=1}^{M}\frac{Z_A}{r_{iA}} + \sum_{i=1}^{N}\sum_{j>i}^{N}\frac{1}{r_{ij}}. \tag{2.1}$$

The first term in Eq.(2.1) represents the kinetic energy of the electrons, the second term represents the coulomb attraction between electron and $M$ point charge, the fourth term represents the repulsion between electrons.

The wave function $\Psi$ is approximated as an antisymmetrized product of normalized $N$ spin orbitals $\chi_i(\mathbf{x})$. Each spin orbital is a product of a spatial orbital $\phi_k(r)$ and a spin function $\sigma(s) = \alpha(s)$ or $\beta(s)$. This antisymmetrized is called Slater determination

$$\Psi_0(\mathbf{x}_1,\ldots,\mathbf{x}_N) = \frac{1}{\sqrt{N!}}\begin{vmatrix} \chi_1(\mathbf{x}_1) & \cdots & \chi_N(\mathbf{x}_1) \\ \vdots & \ddots & \vdots \\ \chi_1(\mathbf{x}_N) & \cdots & \chi_N(\mathbf{x}_N) \end{vmatrix}. \tag{2.2}$$

The Hartree-Fock approximation is the method, which is found the orthonormal orbital $\chi_i$ minimized the energy of the system for this determinant $\Psi$. According to the variational principle, the "best" spin orbitals are those which minimized the electronic energy

$$E_0 = \langle\Psi_0|\hat{H}|\Psi_0\rangle = \sum_{i=1}^{N} H_i + \frac{1}{2}\sum_{i,j=1}^{N}(J_{ij} - K_{ij}) \tag{2.3}$$

where

$$H_i = \int \chi_i^*(\mathbf{x}_1)\left(-\frac{1}{2}\nabla_i^2 + \sum_{A=1}^{M}\frac{Z_A}{r_{iA}}\right)\chi_i(\mathbf{x}_1)d\mathbf{x}_1 \tag{2.4}$$

$$J_{ij} = \iint \chi_i^*(\mathbf{x}_1)\chi_j^*(\mathbf{x}_2)\frac{1}{r_{12}}\chi_i(\mathbf{x}_1)\chi_j(\mathbf{x}_2)d\mathbf{x}_1 d\mathbf{x}_2 \tag{2.5}$$

$$K_{ij} = \iint \chi_i^*(\mathbf{x}_1)\chi_j^*(\mathbf{x}_2)\frac{1}{r_{12}}\chi_i(\mathbf{x}_2)\chi_j(\mathbf{x}_1)d\mathbf{x}_1 d\mathbf{x}_2. \tag{2.6}$$

The $J_{ij}$ integrals are *Coulomb integrals* and the $K_{ij}$ integrals are called *Exchange integrals*. The following equality is important

$$J_{ii} = K_{ii}. \tag{2.7}$$

Minimizing Eq.(2.3) subject to the orthonormalization conditions

$$\int \chi_i^*(\mathbf{x})\chi_j(\mathbf{x})d\mathbf{x} = \delta_{ij}, \tag{2.8}$$

we obtain the Hartree-Fock differential equations

$$\hat{f}|\chi_i\rangle = \sum_{j=1}^{N} \epsilon_{ij}|\chi_j\rangle \tag{2.9}$$

where

$$\hat{f}(i) = -\frac{1}{2}\nabla_i^2 - \sum_{A=1}^{M} \frac{Z_A}{r_{iA}} + v^{HF}(i). \tag{2.10}$$

The operator $\hat{f}(i)$ is an effective one-electron operator, called the *Fock* operator. $v^{HF}(i)$ is the average potential influenced by the $i$-th electron due to the presence of the other electrons. This idea leads us to the simple problem for the complicated many-body system, that is, we can regard it as a one-electron problem where electron-electron repulsion is treated in an average way.

There are $N$ solutions in the Eq.(2.9), but a unitary transformation of those solutions is also the solution for Eq.(2.9). In other words, it means that the wave function based on the Slater determinant does not change by an unitary transformation.

Since the matrix $\epsilon$ is Hermitian, one may choose a Unitary matrix $\mathbf{U}$ to diagonalize it. The corresponding orbitals $\chi'_i$, called the following *canonical Hartree-Fock orbitals*, satisfy the *canonical Hartree-Fock equations*

$$\hat{f}|\chi'_i\rangle = \epsilon'_i|\chi'_i\rangle. \tag{2.11}$$

We henceforth drop the primes and write the Hartree-Fock equations as

$$\hat{f}|\chi_i\rangle = \epsilon_i|\chi_i\rangle. \tag{2.12}$$

We can regard the problem to solve the single Slater determinant as the problem to solve the molecular orbital (MO) by the Hartree-Fock equation (2.12). Understanding of the orbitals, which is obtained by solving this canonical equations, is given by Koopmans' theorem [24]. According to the theorem, the canonical orbital are uniquely appropriate for describing removal of electron from the system.

### 2.1.2 Restricted Closed-Shell Hartree-Fock: The Roothaan Equations

As mention above, we can realize the informations of the molecules by solving the Hartree-Fock equation. However, it is difficult to solve this equation numerically as it is. Roothaan introduced *a linear combination of atomic orbitals* (LCAO), and the differential equation could be converted to a set of algebraic equations and solved by standard matrix functions [25].

Before introducing the LCAO, let us consider eliminating spin. A closed-shell restricted set of spin orbitals has the form

$$\chi_i(\mathbf{x}) = \begin{cases} \psi_j(\mathbf{r})\alpha(s) \\ \psi_j(\mathbf{r})\beta(s) \end{cases}. \tag{2.13}$$

Substituting Eq.(2.13) into the Hatree-Fock equation (2.12), we can obtain the following equation

$$\hat{f}(\mathbf{x}_1)\psi_j(\mathbf{r}_1)\alpha(s_1) = \epsilon_j\psi_j(\mathbf{r}_1)\alpha(s_1). \tag{2.14}$$

Multiplying on the left by $\alpha^*(s_1)$ and performing the integrations over spin, we obtain the following equation finally

$$\hat{f}(1)\psi_j(1) = \epsilon_j\psi_j(1), \tag{2.15}$$

where

$$\hat{f}(1) = h(1) + \sum_a^{N/2} 2J_a(1) - K_a(1). \tag{2.16}$$

$\hat{f}(1)$ is the closed-shell Fock operator, and $J_a(1)$ and $K_a(1)$ represent the closed-shell coulomb and exchange operators, respectively.

Since we have eliminated spin, next we show that the differential equation can be converted to a set of algebraic equations by introducing the basis set. We introduce the expansion of the one-electron orbitals $\psi_i$ as

$$\psi_i = \sum_{\mu=1}^{K} C_{\mu i}\phi_\mu \quad i = 1,2,\ldots,K, \tag{2.17}$$

where $c_{\mu i}$ is the $\mu$-th orbital coefficient of the $i$-th MO $\psi$, and the $K$ orbital $\phi$ form the LCAO basis set. Substituting Eq. (2.17) into the Hartree-Fock equation (2.16), multiplying by $\phi_\mu^*(1)$ on the left and integrating, we turn the integro-differential equation into a matrix equation

$$\sum_\nu C_{\nu i}\int \phi_\mu^*(1)\hat{f}(1)\phi_\nu(1)d\mathbf{r}_1 = \epsilon_i\sum_\nu C_{\nu i}\int \phi_\mu^*(1)\phi_\nu(1)d\mathbf{r}_1. \tag{2.18}$$

Here we define the *overlap matrix* **S** and the *Fock matrix* **F** as

$$S_{\mu\nu} = \int \phi_\mu^*(1)\phi_\nu(1)d\mathbf{r}_1 \tag{2.19}$$

$$F_{\mu\nu} = \int \phi_\mu^*(1)\hat{f}(1)\phi_\nu(1)d\mathbf{r}_1. \tag{2.20}$$

With these definitions of **S** and **F**, we can write the integrated Hartree-Fock equation (2.18) as

$$\sum_\nu F_{\mu\nu}C_{\nu i} = \epsilon_i\sum_\nu S_{\mu\nu}C_{\nu i} \quad i = 1,2,\ldots,K \tag{2.21}$$

or, simply,

$$\mathbf{FC} = \mathbf{SC}\epsilon. \tag{2.22}$$

Eq.(2.22) is called the *Roothaan equations* [25].

### 2.1.3 Unrestricted Open-Shell Hartree-Fock: The Pople-Nesbet equations

In previous subsection, we surveyed the restricted closed-shell Hartree-Fock equations, which is called the Roothaan equations. Next we need to consider the open-shell systems. The open-shell Hartree-Fock approach is not appropriate only for a open-shell system like a radical, but also for the dissociation problem as a long bond length for a molecule like $H_2$.

In the open-shell systems, the spatial orbitals are separated $\alpha$ spin into $\beta$ spin

$$\chi_i(\mathbf{x}) = \begin{cases} \psi_j^\alpha(\mathbf{r})\alpha(s) \\ \psi_j^\beta(\mathbf{r})\beta(s) \end{cases} . \tag{2.23}$$

The derivation of the unrestricted Hartree-Fock equations is analogous to the restricted ones. So, we will not repeat all details of the derivation. Substituting Eq.(2.23) into Eq.(2.12) and multiply on the left by spin function $\alpha^*(s_1)$ or $\beta^*(s_1)$, we obtain

$$\hat{f}^\alpha(1)\psi_j^\alpha(1) = \epsilon_j^\alpha \psi_j^\alpha(1) \tag{2.24}$$

$$\hat{f}^\beta(1)\psi_j^\beta(1) = \epsilon_j^\beta \psi_j^\beta(1). \tag{2.25}$$

In order to solve the unrestricted Hartree-Fock equations (2.24) and (2.25), we introduce a basis set, just as we did when deriving the Roothaan equations. We thus introduce the expansion of the one-electron orbitals for $\alpha$ spin $\psi_i^\alpha$ and $\beta$ spin $\psi_i^\beta$,

$$\psi_i^\alpha = \sum_{\mu=1}^{K} C_{\mu i}^\alpha \phi_\mu \quad i = 1,2,\ldots,K \tag{2.26}$$

$$\psi_i^\beta = \sum_{\mu=1}^{K} C_{\mu i}^\beta \phi_\mu \quad i = 1,2,\ldots,K. \tag{2.27}$$

After a few derivation procedure, we finally obtain the algebraic equations, which is called the *Pople-Nesbet equations* [26], for the unrestricted Hartree-Fock equations,

$$\mathbf{F}^\alpha \mathbf{C}^\alpha = \mathbf{S}\mathbf{C}^\alpha \epsilon^\alpha \tag{2.28}$$

$$\mathbf{F}^\beta \mathbf{C}^\beta = \mathbf{S}\mathbf{C}^\beta \epsilon^\beta. \tag{2.29}$$

The Pople-Nesbet equations (2.28) for open-shell systems, as well as the Roothaan equations (2.22), are solved iteratively until the minimum total energy is reached, because the Fock matrix contains the expansion coefficients, so those equations are nonlinear. Once that limit is achieved, further iterations will not change the coefficients. This procedure is called *self-consistent field* (SCF).

## 2.2 Density Functional Theory

Today, density functional theory (DFT) is widely used in chemistry [27–29]. The method based on the DFT have derived from Thomas-Fermi-Dirac model [30–32]. An approach of the DFT is to represent an electron correlation as a functional of the electron density. Foundations of the approach date back to Hohenberg-Kohn (HK) theorem published in 1964 [33].

### 2.2.1 Hohenberg-Kohn Theorems

HK theorem consists of two fundamental theorems [33].

***The First Theorem*** **(HK1)** :

> *The external potential* $v(\mathbf{r})$ *is determined, within a trivial additive constant, by the electron density* $\rho(\mathbf{r})$.

***The Second Theorem*** **(HK2)**:

> *For a trial density* $\tilde{\rho}(\mathbf{r})$, *such that* $\tilde{\rho}(\mathbf{r}) \geq 0$ *and* $\int \tilde{\rho}(\mathbf{r}) d(\mathbf{r}) = N$, *then* $E_0 \geq E_v[\tilde{\rho}]$

The HK1 means that the mapping between potentials and densities is one to one. The proof of the HK1 is by *reductio as absurdum.* If there were two different external potential $v$ and $v'$ differing by more than a constant, there would be two Hamiltonian $H$ and $H'$, whose the ground-state densities were the same. However, those normalized wave functions $\Psi$ and $\Psi'$ must be different. Using $\Psi'$ as a trial function for $\hat{H}$, we obtain

$$\begin{aligned} E_0 < \langle\Psi'|\hat{H}|\Psi'\rangle &= \langle\Psi'|\hat{H}'|\Psi'\rangle + \langle\Psi'|\hat{H} - \hat{H}'|\Psi'\rangle \\ &= E_0' + \int \rho(\mathbf{r})\left[v(\mathbf{r}) - v'(\mathbf{r})\right] d(\mathbf{r}), \end{aligned} \tag{2.30}$$

where $E_0$ and $E_0'$ are the ground-state energies for $\hat{H}$ and $\hat{H}'$, respectively. Similarly, for $\Psi$ and $\hat{H}'$,

$$\begin{aligned} E_0 < \langle\Psi|\hat{H}'|\Psi\rangle &= \langle\Psi|\hat{H}|\Psi\rangle + \langle\Psi|\hat{H}' - \hat{H}|\Psi\rangle \\ &= E_0 + \int \rho(\mathbf{r})\left[v(\mathbf{r}) - v'(\mathbf{r})\right] d(\mathbf{r}). \end{aligned} \tag{2.31}$$

Addition Eq.(2.30) and Eq.(2.31), we obtain

$$E_0 + E_0' < E_0' + E_0 \tag{2.32}$$

This clearly contradicts. Therefore, if $\rho$ is the same for the ground-state, it does not corresponds to two different $v$.

The HK2 gives the variational principle for the energy. The request of the variational principle is to satisfy the stationary principle for the density of the ground-state

$$\delta\left\{E_v[\rho]-\mu\left[\int\rho(\mathbf{r})d\mathbf{r}-N\right]\right\}=0. \tag{2.33}$$

And we can obtain the Euler-Lagrange equation

$$\mu=\frac{\delta E_v[\rho]}{\delta\rho(\mathbf{r})}=v(\mathbf{r})+\frac{\delta F_{\mathrm{HK}}[\rho]}{\delta\rho(\mathbf{r})}, \tag{2.34}$$

where $\mu$ is the chemical potential. The $F_{\mathrm{HK}}$ is an independent term from the external potential, and is called a *universal functional* of $\rho(\mathbf{r})$. If an explicit form for the universal functional is given, we can apply this method to any system. However, it is hard to obtain an explicit form for the universal functional.

### 2.2.2 Levy Constrained-Search Formulation

According to the HK theorem, if the trial density $\tilde{\rho}(\mathbf{r})$ is not negative value and the number of particles is finite, for any trial density functional, the external potential decides unique. In reverse, if the density is given from the antisymmetric ground-state wave function for a Hamiltonian consisting the external potential, it is called *v-representability.* That is, the mapping between the density and the external potential is one to one. However, degenerated ground-state can describe the identical density for many wave functions, so it is not $v$-representability. It turns out that DFT can be formulated for the densities in the variational principle to satisfy a weaker condition as the following,

$$\tilde{\rho}(\mathbf{r})\geq 0,\quad \int\tilde{\rho}(\mathbf{r})d\mathbf{r}=N,\quad \text{and}\quad \int|\nabla\tilde{\rho}^{1/2}(\mathbf{r})|^2 d\mathbf{r}<\infty. \tag{2.35}$$

It is called *N-representability,* and meaning that a density is obtained from some antisymmetric wave function. The $N$-representability is weaker than the $v$-representability, because the former is necessary condition for the letter.

We have showed one-to-one mapping between the ground-state density and the wave function, so we states how it determines wave function from a given density. The density $\rho_0(\mathbf{r})$ gives by the square of the wave function $\Psi_0$. Defining the wave function which becomes the density $\rho_0(\mathbf{r})$ as $\Psi_{\rho_0}$,

$$\langle\Psi_{\rho_0}|\hat{H}|\Psi_{\rho_0}\rangle\geq\langle\Psi_0|\hat{H}|\Psi_0\rangle=E_0 \tag{2.36}$$

is trivial. Expanding the Hamiltonian, we obtain

$$\langle\Psi_{\rho_0}|\hat{T}+\hat{V}_{ee}|\Psi_{\rho_0}\rangle+\int v(\mathbf{r})\rho_0(\mathbf{r})d\mathbf{r}\geq\langle\Psi_0|\hat{T}+\hat{V}_{ee}|\Psi_0\rangle+\int v(\mathbf{r})\rho_0(\mathbf{r})d\mathbf{r}$$
$$\langle\Psi_{\rho_0}|\hat{T}+\hat{V}_{ee}|\Psi_{\rho_0}\rangle\geq\langle\Psi_0|\hat{T}+\hat{V}_{ee}|\Psi_0\rangle. \tag{2.37}$$

The right-hand side of Eq.(2.37) shows $v$-representability, and the left-hand side of Eq.(2.37) shows $N$-representability. Minimizing the left-hand side of Eq.(2.37), it turns out to become $v$-representability

$$\begin{aligned}F_{HK}&=\langle\Psi_0|\hat{T}+\hat{V}_{ee}|\Psi_0\rangle\\&=\min_{\Psi\to\rho_0}\langle\Psi|\hat{T}+\hat{V}_{ee}|\Psi\rangle\end{aligned} \tag{2.38}$$

This is a *constrained-search* for the density functional $F_{HK}[\rho_0]$ [34, 35]. It means that search over all the antisymmetric wave functions gives the $v$-representable wave function. Therefore, we can eliminate the limitation of the HK theorem that there is no degeneracy in the ground-state. Ultimately, the energy of the ground-state is obtained as the functional of the density as the following,

$$\begin{aligned}E[\rho]&=F[\rho]+\int v(\mathbf{r})\rho_0(\mathbf{r})d\mathbf{r}\\&=\min_{\Psi\to\rho_0}\langle\Psi|\hat{T}+\hat{V}_{ee}|\Psi\rangle+\int v(\mathbf{r})\rho_0(\mathbf{r})d\mathbf{r}\end{aligned} \tag{2.39}$$

### 2.2.3 Kohn-Sham Equations

In the section (2.2.1), we have showed that electron density of the ground-state is obtained by minimizing $E[\rho]$ and hence satisfies the Euler equation (2.34). The $F_{HF}[\rho]$ is

$$F_{HK}[\rho]=T[\rho]+V_{ee}[\rho]. \tag{2.40}$$

If we construct explicit forms for the kinetic energy term $T[\rho]$ and the electron-electron interaction term $V_{ee}[\rho]$, we can apply this method to any system as mentioned above. However, there are apparently insuperable difficulties in going beyond the crude level of approximation. Kohn and Sham then introduce orbitals into the problem [36].

Representing the kinetic energy without the interaction not as the density but the wave function, we obtain

$$T_s=\sum_{i=1}^{N}\langle\Psi_s|-\frac{1}{2}\nabla^2|\Psi_s\rangle. \tag{2.41}$$

Using the $T_s$, we rewrite (2.40) as

$$F[\rho]=T_s+J[\rho]+E_{xc}[\rho] \tag{2.42}$$

where

$$E_{xc}[\rho]\equiv T[\rho]-T_s+V_{ee}[\rho]-J[\rho]. \tag{2.43}$$

The $E_{xc}[\rho]$ is called the *exchange-correlation energy*. This term contains the difference between $T$ and $T_s$ and the electron-elentron interaction term in quantum. That is, the parts differing from the explicit energy is integrated into this term.

The energy functional is given by

$$\begin{aligned} E[\rho] &= T[\rho] + V_{ee}[\rho] + \int \rho(\mathbf{r})v(\mathbf{r})d\mathbf{r} \\ &= \sum_{i=1}^{N}\sum_{s}\int \Psi_i^{s,*}(\mathbf{r})\left(-\frac{1}{2}\nabla^2\right)\Psi_i^s(\mathbf{r})d\mathbf{r} + J[\rho] + E_{xc}[\rho] + \int \rho(\mathbf{r})v(\mathbf{r})d\mathbf{r}. \end{aligned} \tag{2.44}$$

The relation between the densities and the molecular orbitals is

$$\rho(\mathbf{r}) = \sum_{i=1}^{N}\sum_{s}\Psi_i^{s,*}(\mathbf{r})\Psi_i^s(\mathbf{r}), \tag{2.45}$$

so we have the energy express in terms of $N$ orbitals.

To derive the Kohn-Sham (KS) equations we need to minimize $E[\rho]$ with respect to the orbitals, subject to the constrain that the orbitals remain orthonormal,

$$\int \Psi_i^*(\mathbf{r})\Psi_j(\mathbf{r})d\mathbf{r} = \delta_{ij}. \tag{2.46}$$

We therefore consider the functional $\Omega[\{\Psi_i\}]$ of the $N$ orbitals

$$\Omega[\{\Psi_i\}] = E[\rho] - \sum_{i}^{N}\sum_{j}^{N}\epsilon_{ij}\int \Psi_i^*(\mathbf{r})\Psi_j(\mathbf{r})d\mathbf{r} \tag{2.47}$$

where $E[\rho]$ is the functional of the $\Psi_i$ expressed in Eq.(2.44) and Eq.(2.45), and the $\epsilon_{ij}$ constitute a set of Lagrange multipliers. Minimization of $E[\rho]$, subject to the constraints, is thus obtained by minimizing $\Omega[\{\Psi_i\}]$, namely,

$$\Omega[\{\Psi_i\}] = 0. \tag{2.48}$$

We obtain the following equation,

$$\left[-\frac{1}{2}\nabla^2 + v_{\text{eff}}\right]\Psi_i = \sum_{j=1}^{N}\epsilon_{ij}\Psi_j \tag{2.49}$$

$$v_{\text{eff}}(\mathbf{r}) = v(\mathbf{r}) + \int \frac{\rho(\mathbf{r})'}{\left|\mathbf{r}-\mathbf{r}'\right|d\mathbf{r}'} + v_{xc}(\mathbf{r}). \tag{2.50}$$

We finally obtain the canonical form of the KS equations

$$\left[-\frac{1}{2}\nabla^2 + v_{\text{eff}}\right]\Psi_i = \epsilon_i\Psi_i. \tag{2.51}$$

The $v_{\text{eff}}(\mathbf{r})$ is the *effective potential* term. The KS equations have the same form as the Hartree-Fock equations, except that a more general local potential $v_{\text{eff}}(\mathbf{r})$ is contained. If the potentail decide unique, we can solve it just as in the Hartree-Fock theory.

### 2.2.4 Spin-Polarized DFT

The formula used the spin unrestricted orbital for DFT is called *spin-polarized DFT.* In the spin-polarized DFT, the exchange-correlation functional is treated as the functional of $\alpha$ electron density $\rho^{\alpha}$ and $\beta$ electron density $\rho^{\beta}$

$$E_{XC} = E_{XC}[\rho^{\alpha}, \rho^{\beta}]. \tag{2.52}$$

The KS equations (2.51) is

$$\left[-\frac{1}{2}\nabla^2 + v_{\text{eff}}\right]\Psi_i = \epsilon_i \Psi_i \tag{2.53}$$

$$v_{\text{eff}}(\mathbf{r}, \sigma) = v(\mathbf{r}) + \int \frac{\rho(\mathbf{r})'}{\left|\mathbf{r} - \mathbf{r}'\right| d\mathbf{r}'} + v_{xc}(\mathbf{r}, \sigma). \tag{2.54}$$

### 2.2.5 Exchange-Correlation Functionals

As mentioned until now, Hohenberg and Korn demonstrated that the $E_{XC}[\rho]$ is decided only density. However, there are insuperable difficulties, because we do not know an explicit exchange-correlation functional. So we use the approximation of the functional. The exchange-correlation functional $E_{XC}[\rho]$ is typically split up into two terms, $E_X[\rho]$ and $E_C[\rho]$ for the exchange and correlation, respectively. The first apploximation to the exchange functional is the so called *local density approximation* (LDA),

$$E_X^{\text{LDA}}[\rho] = -\frac{3}{4}\left(\frac{3}{\pi}\right)^{1/3} \int \rho^{4/3}(\mathbf{r}) d\mathbf{r}. \tag{2.55}$$

To derive the functional, a homogeneous electron gas is used. The LDA approximation has two main drawbacks: First, it originates from a homogeneous electron gas, which is normally not found in real systems. Also, the dependence on $\mathbf{r}$ in the limit of $\mathbf{r} \to \infty$ is not correct.

We does not consider a molecular nonuniform property for LDA in the beginnings of the density functional. Taking in this nonuniform property, a correction used a density gradient is thought out, and called *generalized gradient approximation* (GGA),

$$E_X^{\text{GGA}}[\rho] = -\frac{3}{4}\left(\frac{3}{\pi}\right)^{1/3} \int \rho^{4/3}(\mathbf{r}) F(\chi) d\mathbf{r}. \tag{2.56}$$

The correlation term is not taken in the Hartree-Fock theory, and it is not defined as the method used the single Slater determinant. For this term, Lee, Yang and Parr thought out the following functional [37],

$$E_C^{\text{LYP}} = -a \int \frac{\rho(\mathbf{r}) + 2b\rho^{-5/3}(\mathbf{r})\left[\sum_{\sigma} \rho_{\sigma}(\mathbf{r}) t_{\sigma}^{HF}(\mathbf{r}) - \rho(\mathbf{r}) t^{W}(\mathbf{r})\right] \exp\left(-c\rho^{-1/3}(\mathbf{r})\right)}{1 + d\rho^{-1/3}(\mathbf{r})} \gamma(\mathbf{r}) d\mathbf{r}. \tag{2.57}$$

This well-known functional is called LYP functional [37].

### 2.2.6 Hybrid DFT

The LDA and GGA functionals does not contain the nonlocal interaction, leading to many problems for atoms and molecules. A *hybrid DFT* is widely used for correcting the problems not containing the nonlocal interaction. In the hybrid DFT, the $E_{XC}$ is framed by mixing the GGA functinals with the nonlocal interaction of HF method. In the hybrid DFT, mixing parameters is used, and fitting by many calculations. The most hybrid DFT is the B3LYP [38],

$$E_{XC}^{\mathrm{B3LYP}} = 0.20E_X^{\mathrm{HF}} + 0.18E_X^{\mathrm{Slater}} + 0.72E_X^{\mathrm{Becke88}} + 0.19E_C^{\mathrm{VWN}} + 0.81E_C^{\mathrm{LYP}}, \tag{2.58}$$

where $E_X^{\mathrm{HF}}$ is the Hartree-Fock exchange functional, $E_X^{\mathrm{Slater}}$ is the Slater exchange functional, $E_X^{\mathrm{Becke88}}$ is the Becke88 exchange functional [39], $E_C^{\mathrm{VWN}}$ is the Vosko-Wilk-Nusair (VWN) correlation functional [40], and $E_C^{\mathrm{LYP}}$ is the LYP correlaton functional [37].

# Chapter 3

# Quantum Transport

Molecular devices have attracted much attention in nanoelectronics from the limit of the miniaturization of conventional silicon-based devices, because the top-down approach leads to drastic limitations for dimensions smaller than 100 nm [41]. Electron transport in molecular devices is different from the silicon-based devises because of the effects of the electronic structures and the interface to the external contact. In order to investigate the molecular conduction, many experimental and theoretical studies have been reported so far. Especially, a theoretical approach is necessary for understanding the molecular conduction because a control of the contact between the molecule and the electrodes is difficult in an experimental approach. In this chapter, we survey the general concept of the quantum transport [42, 43].

## 3.1 Landauer Formula

In this section, we describe an approach, which is called the *Landauer approach* [44], that has proved to be very useful in describing electron transport. In this approach, the current through a conductor is expressed in terms of the *probability that an electron can transmit through it.*

We consider a ballistic conductor having one conductive channel and do not consider the interaction between electrons, and the effect of temperature. We assume the Figure (3.1) as this model. We define $\mathrm{Res}_1$ and $\mathrm{Res}_2$ as the reservoirs locating on right and left on the sample, and define those chemical potential as $\mu_1$ and $\mu_2$, assuming $\mu_1 > \mu_2$. The voltage ($V = (\mu_1 - \mu_2)/e$) is then applied between $\mathrm{Res}_1$ and $\mathrm{Res}_2$. Also, we assume that there are perfect leads ($\mathrm{L}_1$ and $\mathrm{L}_2$) between the sample and the reservoirs. The perfect lead does not contain the scattering of electrons, and perfect lead and reservoirs satisfy the following assumption:

1. The states in $\mathrm{L}_1$ are occupied only by electrons coming in from the left reservoirs and hence must have an electrochemical potential of $\mu_1$.

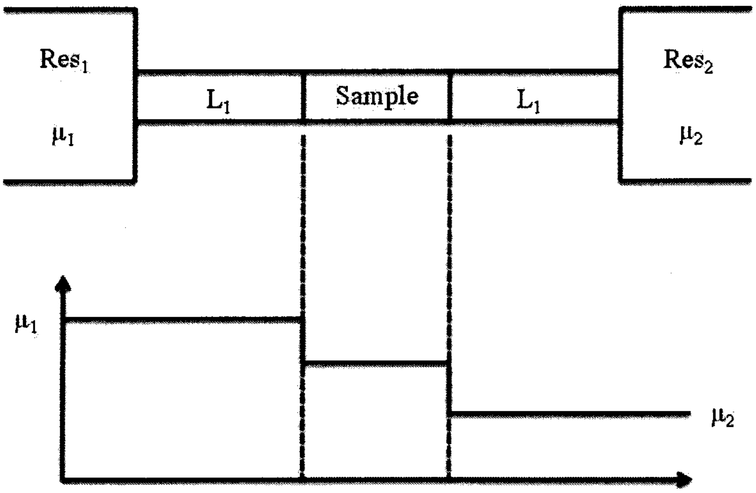

Figure 3.1: A ballistic conductor model connected to two wide reservoirs

2. The states in $L_2$ are occupied only by electrons coming in from the right reservoirs and hence must have an electrochemical potential of $\mu_2$.

3. The $Res_1$ and $Res_2$ are enough large, and the current always keep heat equilibrium.

Under zero temperature, a current takes place entirely in the energy range between $\mu_1$ and $\mu_2$. The influx electrons from $L_1$ is given by

$$I_1^+ = \frac{2e}{h}[\mu_1 - \mu_2]. \tag{3.1}$$

The outflux from $L_2$ is simply the influx at $L_1$ times the transmission probability $\mathscr{T}$,

$$I_2^+ = \frac{2e}{h}\mathscr{T}[\mu_1 - \mu_2]. \tag{3.2}$$

The rest of the flux is reflected back to reservoir 1,

$$I_1^- = \frac{2e}{h}(1-\mathscr{T})[\mu_1 - \mu_2]. \tag{3.3}$$

The net current $I$ flowing at any point in the device is given by

$$I = I_1^+ - I_1^- = I_2^+ = \frac{2e}{h}\mathscr{T}[\mu_1 - \mu_2]. \tag{3.4}$$

So, the conductance $g$ is

$$g = \frac{I}{V} = \frac{I}{(\mu_1 - \mu_2)/|e|} = \frac{2e^2}{h}\mathscr{T}, \tag{3.5}$$

where $\mathscr{T}$ represents the average probability that an electron injected at one end of the conductor will transmit to the other end.

Assuming that $\mathscr{T}$ is unity, we obtain the conductance,

$$g = \frac{2e^2}{h} = 77.4\,\mu\text{S}. \tag{3.6}$$

This indicates that the conductance of a ballistic conductor having one channel is 77.4 $\mu S$, and we can not exceed this conductance.

## 3.2 A Physical Understanding on the Landauer Model

The derivation of the Landauer formula is simple, but there are some questions. Let us consider it for the simple equation (3.5).

Q1 Can we estimate the transmission probabilities between the reservoirs instead of between the leads ?

Q2 Energy is dissipated to be generating the joule-heat when voltage is applied. However, Eq. (3.5) does not contain the mechanism.

The answer for Q1 is that we can estimate that of the leads, but not necessary to do it as long as the reservoirs are *reflectionless*, that is, electrons can transport from the leads to the reservoirs without the reflection. In the Landauer model, it turns out that the conductance depends on the interface between the conductor and the reservoirs which are dissimilar materials. For this reason, this resistance is often called the *contact resistance.* Therefor, the $g$ in the Eq.(3.5) represents the contact resistance. The interface between the leads and the conductor depends on the transmission probability $\mathscr{T}$.

On the Q2, the joule-heat generate inside the reservoirs from the assumption. However, since the capacitance of the reservoirs is enough large, we can neglect it.

## 3.3 Finite Temperature

We have derived the Landauer formula under the assumption of zero temperature. In the finite temperature, the average number of electrons is given by the Fermi distribution function,

$$f_0(E-\mu) = \frac{1}{1+\exp[(E-\mu)/k_B T]}. \tag{3.7}$$

$f(E-\mu)$ represents the probability of occupancy available energy state $E$ at absolute temperature $T$. This distribution is applicable to indistinguishable particles at thermal equilibrium, which obey

Pauli's exclusion principle. In the condition, the influx of electrons from lead 1 is given by

$$i_1^+(E) = \frac{2e}{h} f_1(E), \tag{3.8}$$

while the influx from lead 2 is given by

$$i_2^-(E) = \frac{2e}{h} f_2(E). \tag{3.9}$$

The outflux from lead 2 is obtained as

$$i_2^+(E) = \mathcal{T} i_1^+(E) + (1 - \mathcal{T}') i_2^-(E), \tag{3.10}$$

while the outflux from lead 1 is obtain as

$$i_1^-(E) = (1 - \mathcal{T}) i_1^+(E) + \mathcal{T}' i_2^-(E). \tag{3.11}$$

The net current $i(E)$ in the device is given by

$$\begin{aligned} i(E) &= i_1^+ - i_1^- \\ &= i_2^+ - i_2^- \\ &= \mathcal{T} i_1^+ - \mathcal{T}' i_2^- \\ &= \frac{2e}{h}[\mathcal{T}(E) f_1(E) - \mathcal{T}'(E) f_2(E)]. \end{aligned} \tag{3.12}$$

Assuming that $\mathcal{T}(E) = \mathcal{T}'(E)$, the total current can be written as

$$I = \int i(E) dE, \tag{3.13}$$

where

$$i(E) = \frac{2e}{h} \mathcal{T}(E)[f_1(E) - f_2(E)]. \tag{3.14}$$

Moving away from equilibrium, the applied bias could change the two transmission functions and make them unequal. Thus $\mathcal{T}(E) \neq \mathcal{T}'(E)$ in general. However, if we assume that there is no inelastic scattering inside device, it then can be shown that $\mathcal{T}(E)$ is always equal to $\mathcal{T}'(E)$ for a two-terminal device.

For small deviations from equilibrium state, the current is proportional to the applied bias. The Eq.(3.14) is given by

$$\delta I = \frac{2e}{h} \int \left( \left[ \mathcal{T}(E) \right]_{\text{eq}} \delta [f_1 - f_2] + [f_1 - f_2]_{\text{eq}} \delta \left[ \mathcal{T}(E) \right] \right) dE. \tag{3.15}$$

The second term is zero, because $f_1(E) = f_2(E)$ at equilibrium state. The first term is rewritten by using a Taylor's series expansion,

$$\begin{aligned} \delta[f_1 - f_2] &\approx [\mu_1 - \mu_2]\left(\frac{\partial f}{\partial \mu}\right)_{\mathrm{eq}} \\ &= \left(-\frac{\partial f_0}{\partial E}\right)[\mu_1 - \mu_2]. \end{aligned} \tag{3.16}$$

We then obtain the linear response formula at finite temperature

$$\begin{aligned} g &= \frac{\delta}{(\mu_1 - \mu_2)/e} \\ &= \frac{2e^2}{h}\int \mathcal{T}(E)\left(-\frac{\partial f_0}{\partial E}\right)dE \\ &= \frac{2e^2}{hk_BT}\int \mathcal{T}(E)f_0(E)[1 - f_0(E)]\,dE. \end{aligned} \tag{3.17}$$

## 3.4 Multi-Channel Case

The Landauer model quantizes the conductance of one-dimensional conductor. The conductance of perfect conductor having single channel is $g$ (Eq. (3.6)). In this section, we describe the case in which multiple conducting channels are presented. In this case, the sum of each transmission probability of channel becomes the total transmission probability,

$$g = \frac{2e^2}{h}\sum_{i,j}\mathcal{T}_{i,j}, \tag{3.18}$$

where $\mathcal{T}_{i,j}$ means the transmission probability of the process which transports from channel i to j. In order to calculate the $\mathcal{T}_{i,j}$, we often use the *S-matrix*. A coherent conductor can be characterized at each energy by the S-matrix that relates the outgoing wave amplitudes to the incoming wave amplitudes at different leads.

The incoming and reflecting waves are moving in each channel (Figure 3.3). We consider the system, which connects the two conducting channel 1 and 2 as illustrate in Figure 3.2. The wavefunctions in channel 1 and 2 can be represented by the plane wave as the following,

$$\psi_1 = a_1 e^{ikx} + b_1 e^{ikx}, \tag{3.19}$$

$$\psi_2 = a_2 e^{ikx} + b_2 e^{ikx}. \tag{3.20}$$

For simplicity, we use the common $k$ in channel 1 and 2, but in general, they are different each other. According to the Schrödinger equation, there are the linear relation in between an incoming

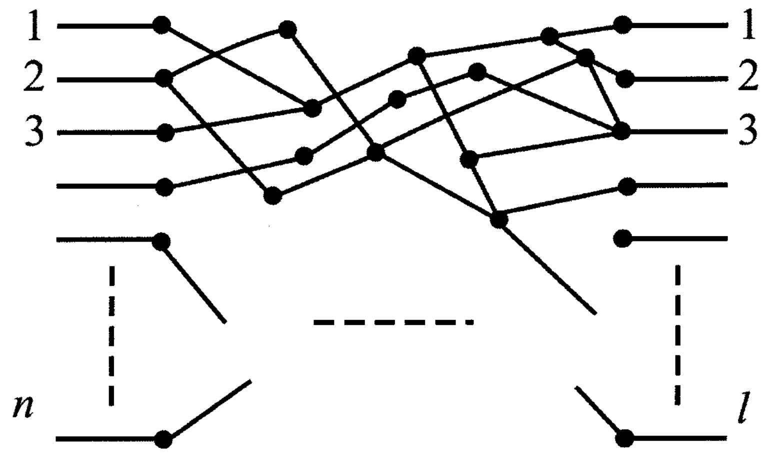

Figure 3.2: The model of multi-channel system

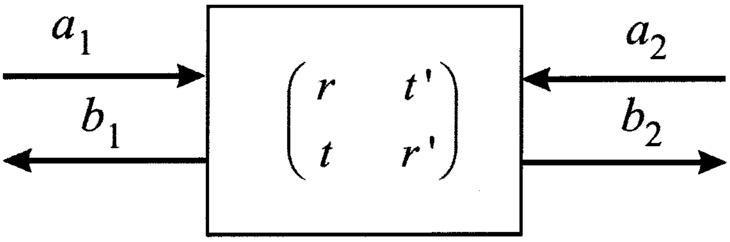

Figure 3.3: The S-matrix of the one-dimensional conductor

amplitude $(a_1, a_2)$ and an outgoing amplitude $(b_1, b_2)$, then

$$\begin{aligned} b_1 &= r a_1 + t_2', \\ b_2 &= t a_1 + r_2', \end{aligned} \tag{3.21}$$

where $(r, t)$ is the left side of the matrix of the reflection coefficient, and $(r', t')$ is the right side of the matrix of the transmission coefficient. Eq.(3.21) is rewritten as the following,

$$\mathbf{b} = \mathbf{Sa}, \quad \mathbf{S} = \begin{pmatrix} r & t' \\ t & r' \end{pmatrix}. \tag{3.22}$$

The **S** is called S-matrix and must be the unitary matrix.

We can make generalizations the above concept as the following. We consider one coherent conductor, and count all of the channels where the electrons can move.

The transmission probability $T_{m \leftarrow n}$ is then obtained by taking the squared magnitude of the corresponding element of the S-matrix.

$$T_{m \leftarrow n} = |s_{m \leftarrow n}|^2 \tag{3.23}$$

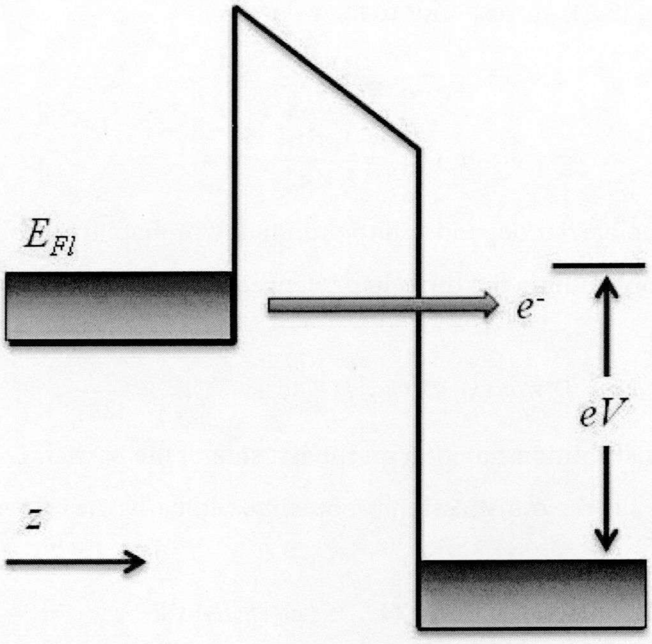

Figure 3.4: Band diagram for a tunneling barrier under dias, illustrating charge flow

We have introduced the arrows in the subscripts just as a reminder that the direction of propagation is backwards from the second subscript to the first one.

## 3.5 Current Density

The Landauer formula is the method that investigates the conductance (or current) between the reservoirs and conductor. In this section, we derive the Landauer formula from another approach.

In an equilibrium state where the bias voltage is zero, the amplitudes of the waves of left and right direction is equal to each other, so that the current does not flow. The general problem is shown Figure 3.4 for a beneric tunneling barrier. Considering that a real device is three-dimensional system, we assume that the flowing direction of the tunneling current is $z$-direction, and split the $z$-direction into perpendicular direction against it. We deal with the transport of the electrons of $z$-direction as the tunneling process. The transport of perpendicular direction is not affect for the tunneling process because it is regarded as free-electrons. The energy of $z$-direction is written by

$$E_z = \frac{\hbar^2 k_{lz}^2}{2m} = \frac{\hbar^2 k_{rz}^2}{2m} + \text{constant}. \tag{3.24}$$

$k_{lz}$ is the $z$-component of the wave vector for a region of the left side of the barrier, and $k_{rz}$ is the $z$-component of the wave vector in the right side. The constant term is the dependent on the bias voltage, the value takes a negative value when the potential of a region of the right side is a positive value. The differential of Eq.(3.24) corresponds to the velocity,

$$v_z(k_{lz}) = \frac{1}{\hbar}\frac{\mathrm{d}E}{\mathrm{d}k_{lz}}, \tag{3.25}$$

$$v_z(k_{rz}) = \frac{1}{\hbar}\frac{\mathrm{d}E}{\mathrm{d}k_{rz}}. \tag{3.26}$$

The current through the barrier depends on the tunneling probability through the barrier and the number of electrons contributing the tunneling. Hence, the current density from the left to the right is written,

$$J_{\mathrm{LR}} = e\int D(\mathbf{k})\, v_z(k_{lz})\mathcal{T}(k_{lz}) f(E_{\mathrm{L}})\mathrm{d}^3\mathbf{k}, \quad D(\mathbf{k}) = \frac{2}{(2\pi)^3}, \tag{3.27}$$

where $f(E_{\mathrm{L}})$ is the Fermi distribution function on the left side of the barrier, $D(\mathbf{k})$ is the density of state in **k**-space, and $\mathcal{T}(k_{lz})$ is the transmission probability. Similarly, the current density from the right to the left is written,

$$J_{\mathrm{RL}} = e\int D(\mathbf{k})\, v_z(k_{rz})\mathcal{T}(k_{rz}) f(E_{\mathrm{R}})\mathrm{d}^3\mathbf{k}. \tag{3.28}$$

If the energy of the left side is equal to that of the right side, the transmission probability of the left side is equal to that of the right side, that is, those are symmetric so that $\mathcal{T}(k_{lz}) = \mathcal{T}(k_{rz})$, in spite of the direction moving the electrons. Adding Eq.(3.27) to Eq.(3.28), we can obtain,

$$\begin{aligned} J &= e\int D(\mathbf{k})\, v_z(k_z)\mathcal{T}(k_z)\Big[f(E_{\mathrm{L}}) - f(E_{\mathrm{R}})\Big]\mathrm{d}^3\mathbf{k} \\ &= e\int D(\mathbf{k})\, v_z(k_z)\mathcal{T}(k_z)\Big[f(E_{\mathrm{L}}) - f(E_{\mathrm{L}} + eV)\Big]\mathrm{d}^3\mathbf{k}. \end{aligned} \tag{3.29}$$

In order to rewrite the simple equation, the energy of the left side of the barrier is separated into the $E_z$ for the $z$-direction and the $E_\perp$ for the perpendicular direction,

$$E = E_z + E_\perp, \tag{3.30}$$

and

$$\mathrm{d}^3\mathbf{k} = \mathrm{d}^2 k_\perp \mathrm{d}k_z. \tag{3.31}$$

Here, the differential $\mathrm{d}k_z$ is rewrite by the differential on the $z$-direction energy $E_z$,

$$\mathrm{d}k_z = \left(\frac{\mathrm{d}E}{\mathrm{d}k_z}\right)^{-1}\frac{\mathrm{d}E}{\mathrm{d}E_z}\mathrm{d}E_z, \tag{3.32}$$

$$\frac{\mathrm{d}E}{\mathrm{d}k_z} = \frac{\hbar^2 k_z}{m} = \hbar v_z. \tag{3.33}$$

Also,

$$\begin{aligned} \mathrm{d}^2 k_\perp &= 2\pi k_\perp \mathrm{d}k_\perp, \\ &= \left(\frac{2\pi m}{\hbar^2}\right)\mathrm{d}E_\perp \quad \left(k_\perp \mathrm{d}k_\perp = \frac{m}{\hbar^2}\mathrm{d}E_\perp\right). \end{aligned} \tag{3.34}$$

So the Eq.(3.29) is rewritten,

$$\begin{aligned} J &= \frac{4\pi e m}{(2\pi)^3\hbar}\int_0^\infty \mathcal{T}(E_z)\mathrm{d}E_z \int_0^\infty \Big[f(E_z+E_\perp)-f(E_z+E_\perp+eV)\Big]\mathrm{d}E_\perp, \\ &= \frac{emk_\mathrm{B}T}{2\pi^2\hbar^3}\int_0^\infty \mathcal{T}(E_z)\ln\left(\frac{1+e^{(E_\mathrm{F}^l-E_z)/k_\mathrm{B}T}}{1+e^{(E_\mathrm{F}^l+eV-E_z)/k_\mathrm{B}T}}\right)\mathrm{d}E_z, \end{aligned} \tag{3.35}$$

where the $E_\mathrm{F}^l$ is the Fermi energy on the left side. The logarithmic term is sometimes called the *supply function.*

# Part III

# Development of Electron Conductivity Calculation Method for Open-Shell Molecules

# Chapter 4

# Development of Electron Conductivity Calculation Method for Open-Shell Molecules

## 4.1 Introduction

Interest in the transport properties of single molecules has been increasing due to their possible use as electronic components since Aviram and Ratner proposed the first molecular-based diode in 1974 [1]. Their study lead to extremely downsize electronic circuits by utilizing the organic molecules. After that, many studies of the molecular devices have carried out so far. In the beginnings of the studies, Langmuir-Blodgett (LB) was used to realize the molecular devices. Various molecules were synthesized and LB films were made, and the electron characteristics were measured by connecting the electrode. However, it turns out that it is difficult to realize the molecular device by utilizing the LB files. In 1982, Scanning Tunneling Microscope (STM) was developed, and its applications to the molecular device advanced. After that, studies of the molecular devices by Self-Assembled Monolayer (SAM) and Mechanical Break Junction (MBJ) have been also advanced. The idea of the MBJ (Figure 4.1) is to break by bending a very thin metal wire fabricated on the surface of an elastic substrate, thereby creating two electrodes [45].

Reed et al. reported that molecules of benzene-1,4-dithiol (BDT) were self-assembled onto the two facing gold electrodes of the MBJ to form a statically stable gold-sulfur-aryl-sulfur-gold system, and the $I$-$V$characteristics of the BDT shows 0.045 $\mu$S at about 0.7 V [2]. Many groups have reported the conductance of the BDT, but the reported conductance values vary from $< 10^{-4}G_0$ to $\sim 0.1G_0$, where $G_0 = 2e^2/h \sim 77.5\mu$S [2,4,46–48]. Also there are theoretical studies on the $I$-$V$characteristics of the BDTs, but there is the discrepancy between the experimental and calculated conductance. For a one of the reason, there are distinct Au-S bonding geometry. Those are top-molecule-top geometry,

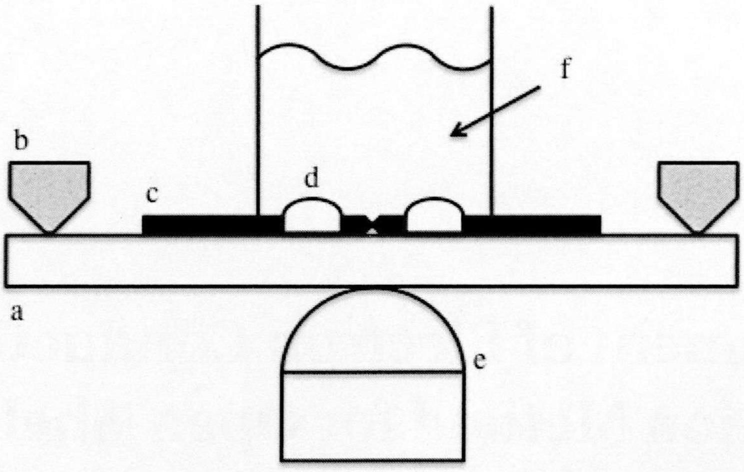

Figure 4.1: A schematic of the mechanical break junction (MBJ) with (a) the bending beam, (b) the counter supports, (c) the notched gold wire, (d) the glue contacts, (e) the pizeo element, and (f) the glass tube containing the solution. Ref. [2] is referred.

where both S atoms of the molecule occupy the top site of the Au surface, bridge-molecule-bridge geometry where both S atoms connect to the middle of the two Au atoms and hollow-molecule-hollow geometry, where both S atoms connect to the threefold hollow site of Au electrodes. For these viewpoints, Kondo et al. demonstrated single BDT theoretically [7].

Of course, many molecules were studied not only on the BDT but also on the various molecules for the realization of the molecular devices, e.g. see ref. [49]. STM measurements on $C_{60}$ have revealed linear $I$-$V$ characteristics at low applied bias voltages [50] (Figure 4.2). The resistance of the $C_{60}$ is 54.80 MS for the junction at tip contact. The $I$-$V$ characteristics of bisthiolterthiophene was also reported [51] (Figure 4.3). The molecules is connected to the two facing gold electrodes, and forming metal-molecules-metal junctions. The conductance of 10-100 nS was obtained. Especially, the top-down approach, such as the miniaturization of conventional silicon-based devices, leads to drastic limitations for dimensions smaller than 100 nm. So, the realization of the devices by utilizing the molecules is necessary for miniaturizing the devices.

## 4.2 Motivations

The molecular devices mentioned above are closed-shell systems in general. However, I have the interest in introducing spins into the molecular devices, because a coexistence of localized spins and conduction electrons has attracted much attention in a material science. It is well known that tetrathiafulvalene (TTF) derivatives containing redox active $\pi$ electrons show the electron conduc-

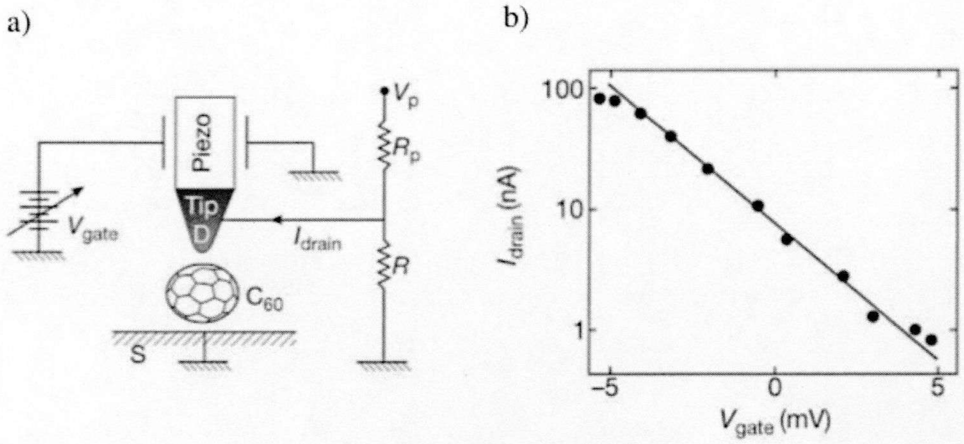

Figure 4.2: a) A schematic of the $C_{60}$ device, b) *I-V* characteristics of the $C_{60}$ device. [These figures were taken from C. Joachim et al. *Phys. Rev Lett.*, **74**, 2102 (1995)]

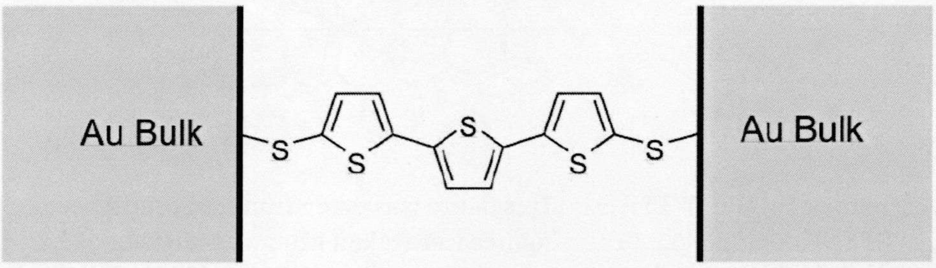

Figure 4.3: A schematic of the bisthiolterthiophene device. A conjugated molecule is chemisorbed onto the gold electrodes *via* the thiolate terminal groups. [This figure was taken from C. Kerguerls et al. *Phys. Rev. B.*, **59**, 12505, (1999)]

tivity. If such molecules can be combined with localized spin species, one will obtain coexistent systems of localized spins and conduction electrons. Coronado et al. has reported that (BEDT-TTF)$_3$[MnCr(ox)$_3$] (BEDT-TTF = bis(ethylenedithio) tetrathiafulvalene) shows both ferromagnetic spin interactions and the conductivity [52] in Figure 4.4(a). This molecule-based compound shows a ferromagnetism at 5.5K and a metallic behavior at the range from room temperature to 2K. Matsushita et al. reported the coexistence of the ferromagnetism and the conductivity using a pure organic compound, which shows a negative magneto-resistance below 15K [53] in Figure 4.4(b). Peng et al. reported the magnetism and the electron conductivity of extended metal atom chains (EMAC) [8] in Figure 4.4(c).

On the other hand, there are many reports of the electron transfer not only on the synthesized molecules but also biological molecules such as DNA. DNA is also known for its conductivity by $\pi$-stacking interactions [9–19], e.g. *see* Figure 4.5. Recently, Tanaka et al. reported alternative base-pair

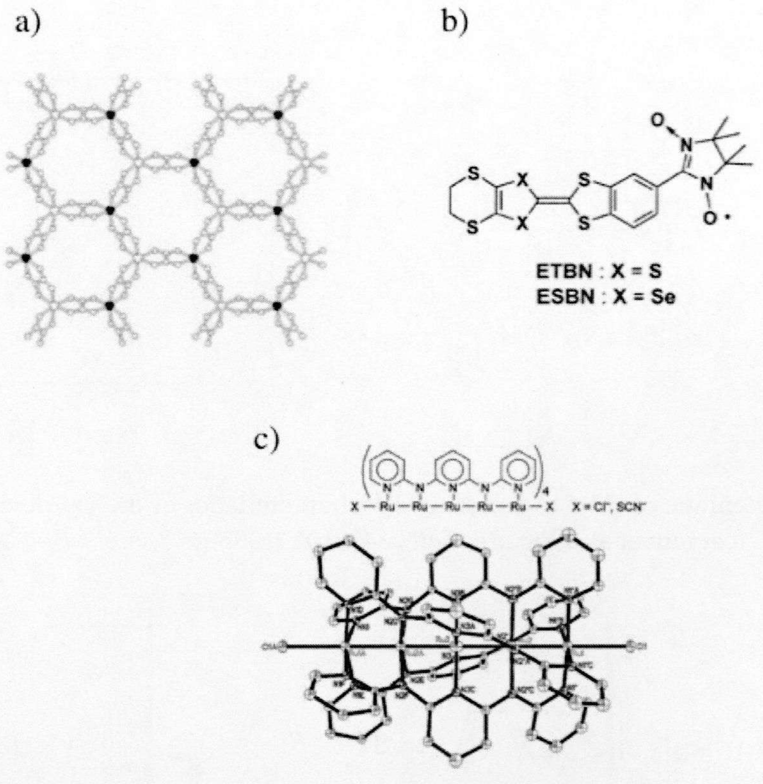

Figure 4.4: A scheme of a) BEDT-TTF [52] [This figure was taken from E. Corondo et al. *Nature*, **408**, 447 (2000)], b) ETBN and ESBS [53] [These figures were taken from M. Matsushita et al. *Chem. Lett.*, **36**, 110 (2007)] and c) EMAC [8] [This figure was taken from C. Yin et al. *J. Am. Chem. Soc.*, **130**, 10090 (2008).]

models in which hydrogen bonds between natural base pairs are replaced by $Cu^{2+}$-mediated base pairs of hydroxypyridone nucleobases [20] (Figure 4.6). An existence of the ferromagnetic interaction between electron spins on adjacent $Cu^{2+}$ centers has been found by using electron paramagnetic resonance (EPR) spectra at 1.5K [20] (I have investigated for the theoretical approach on the magnetism, *in detail see* Chapter 8 (89 page)). However, the conductivity of this system has not been reported so far, in spite of being expected the realization of the spintronics device by DNA.

There are many theoretical reports on the magnetism of these systems, but almost no theoretical reports on the electron conductivity of these systems. This main reason is that these systems are the open-shell systems and there is no theoretical method on the electron conductivity for the open-shell systems, especially the calculation of the systems containing metal ions is difficult. Then, I developed the calculation method of the electron conductivity for open-shell molecules using an elastic scattering Green's approach in low computational costs. Finally, if there are a spin source in a system, the Kondo effect seems to be important. However, in this developed model, I do not consider the Kondo effect.

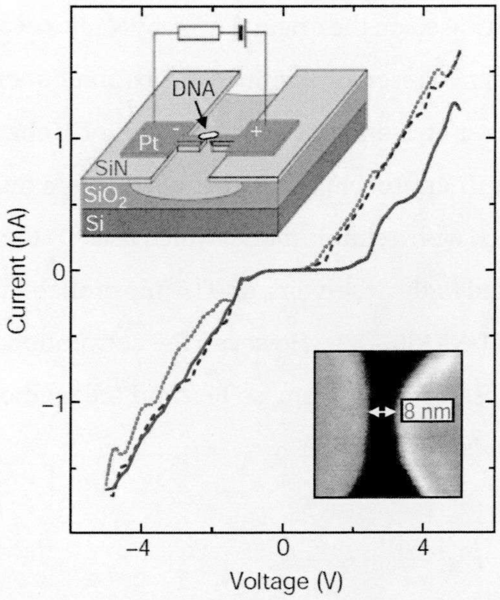

Figure 4.5: Current-voltage curves measured at room temperature on a DNA molecule trapped between two metal nanoelectrodes [This figure was taken from D. Porath et al. *Nature*, **403**, 635, (2000)]

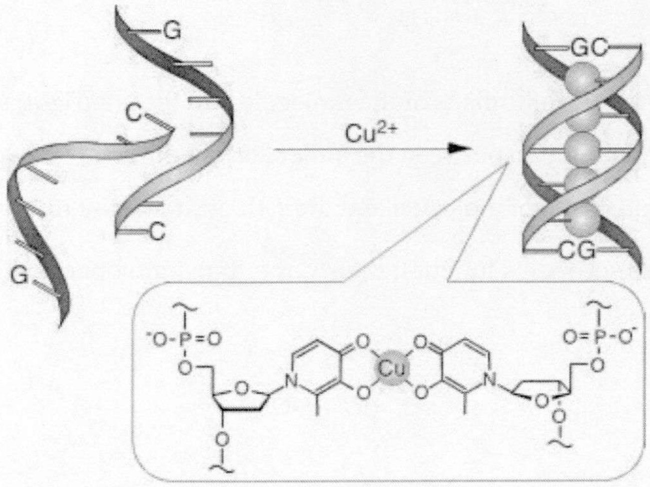

Figure 4.6: Schematic representation of $Cu^{2+}$-mediated duplex formation between two artificial DNA strands in which hydroxypyridone nucleobases replace natural base pairs. [This figure was taken from K. Tanaka et al. *Science*, **299**, 1212 (2003)]

## 4.3 Development of the Theory

The elastic scattering approach based on the original work by Mujica et al. is often used to investigate the *I*-*V* characteristics between two reservoirs with each electronic state at the two terminals of the molecular wire [54–56]. However, it is difficult to calculate the *I*-*V* characteristics for large systems consisting of many atoms in this approach, because it needs quite high computational resources. Luo et al. modified the approach with a simple model which uses (1) the overlap matrix elements, (2) the terminated atoms connected to the reservoirs, and (3) the probabilities that the electron exists at the terminated atoms within LUMO [57–59]. However, the conventional elastic scattering theory is originally developed for the closed- shell system, so I extend the method to the open-shell systems. The Hamiltonian of the system is written as

$$H = H_{\mathrm{M}} + H_{\mathrm{L}} + H_{\mathrm{R}} + U, \tag{4.1}$$

$$\begin{aligned} H_{\mathrm{M}} &= \sum_{\sigma=\pm}\sum_{\alpha} E^0_{\alpha\sigma}\left|\alpha_\sigma\right\rangle\left\langle\alpha_\sigma\right| \\ &\equiv \sum_{\sigma=\pm}\sum_{\alpha} E^0_{\alpha\sigma} C^*_{\alpha\sigma I} C_{\alpha\sigma J}\left|I\right\rangle\left\langle J\right|, \end{aligned} \tag{4.2}$$

$$H_{\mathrm{L}} = \sum_{\sigma=\pm}\sum_{i} E^0_{i\sigma}\left|i_\sigma\right\rangle\left\langle i_\sigma\right|, \tag{4.3}$$

$$H_{\mathrm{R}} = \sum_{\sigma=\pm}\sum_{j} E^0_{j\sigma}\left|j_\sigma\right\rangle\left\langle j_\sigma\right|, \tag{4.4}$$

$$U = \sum_{\sigma=\pm}\sum_{I}\left(\sum_{i}\gamma_{iI,\sigma}\left|i_\alpha\right\rangle\left\langle I\right| + \sum_{j}\gamma_{jI,\sigma}\left|j_\alpha\right\rangle\left\langle I\right|\right) + c.c., \tag{4.5}$$

where $H_{\mathrm{M}}$ and $H_{\mathrm{L(R)}}$ are the Hamiltonians of the molecule and the left (right) side reservoirs, respectively. $U$ is the interaction potential between the molecule and the reservoirs and $\gamma_{iI,\sigma}$ represents the interaction between the $I$-th site of molecule and the $i$-th orbital of the reservoirs with spin $\sigma$.

In the elastic scattering Green's function theory, the transition operator [60–62] ($\hat{\mathcal{T}}$), is defined as

$$\hat{\mathcal{T}} = U + UGU, \tag{4.6}$$

where $G$ is the Green's function,

$$G(z) = (z - H)^{-1}. \tag{4.7}$$

$z$ is a complex variable. Assuming that the reservoirs directly intact with the end-sites (site 1 and N) of the molecule only [54, 63], the transition matrix element ($\hat{\mathscr{T}}_{ij,\sigma}$) can be rewritten as

$$\hat{\mathscr{T}}_{ij,\sigma}(z) = \gamma_{i1,\sigma} G_{1N,\gamma}(z) \gamma_{Nj,\sigma}, \tag{4.8}$$

$$\begin{aligned} G_{1N,\gamma}(z) &= \sum_{\eta} \left\langle 1 \middle| \frac{1}{z-H} \middle| \varphi_{\sigma}^{\eta} \right\rangle \langle \varphi_{\sigma}^{\eta} | N \rangle \\ &= \sum_{\eta} \frac{\langle 1 | \varphi_{\sigma}^{\eta} \rangle \langle \varphi_{\sigma}^{\eta} | N \rangle}{z - \epsilon_{\sigma}^{\eta}} \\ &\approx \sum_{\eta} \frac{\langle 1 | \phi_{\sigma}^{\eta} \rangle \langle \phi_{\sigma}^{\eta} | N \rangle}{z - \tilde{\epsilon}_{\sigma}^{\eta}}, \end{aligned} \tag{4.9}$$

where $|\varphi_{\sigma}^{\eta}\rangle$ is the eigenstate of the total Hamiltonian $H$ ($H|\varphi_{\sigma}^{\eta}\rangle = \epsilon_{\sigma}^{\eta}|\varphi_{\sigma}^{\eta}\rangle$). Here, the end-site is defined as the terminal atom connected to the reservoir as explained above. The eigenstate $\eta$ that overlaps with the molecular end-sites only contributes significantly to the Green's function matrix element. Therefore, $|\phi_{\sigma}^{\eta}\rangle$ can be approximated by orbitals obtained from the Kohn-Sham equation of a finite system consisting of the molecule sandwiched between reservoirs ($\tilde{H}|\phi_{\sigma}^{\eta}\rangle = \tilde{\epsilon}_{\sigma}^{\eta}|\phi_{\sigma}^{\eta}\rangle$) [57].

In the linear response theory, a static carrier conduction [64] ($i^{\mathrm{LR}}$) of the system that are applied the voltage ($V_{\mathrm{D}}$) by right and left reservoirs is given as

$$i_{\sigma}^{\mathrm{LR}} = \frac{1}{2} \sum_{\eta} \frac{emk_{\mathrm{B}}T}{2\pi^2\hbar^3} \int_{eV_{\mathrm{D}}}^{\infty} \left| \hat{\mathscr{T}}_{\sigma}(E) \right|_{\eta}^{2} f_{\sigma}(E) \mathrm{d}E, \tag{4.10}$$

$$f_{\sigma}(E) = \left\{ \ln\left[1 + \exp\left(\frac{E_{\mathrm{F},\sigma} + eV_{\mathrm{D}} - E}{k_{\mathrm{B}}T}\right)\right] - \ln\left[1 + \exp\left(\frac{E_{\mathrm{F},\sigma} - E}{k_{\mathrm{B}}T}\right)\right] \right\}, \tag{4.11}$$

where $E_{\mathrm{F}}$ is the Fermi energy. Here, I define that the intermediate value of HOMO and LUMO orbital energies of the extended molecular system is the Fermi energy. Since the spacing between molecular orbitals is large, I can assume that the interference between difference scattering channels is negligible [57]. $\left| \hat{\mathscr{T}}_{\sigma}(E) \right|_{\eta}^{2}$ then represents the transition probability,

$$\left| \hat{\mathscr{T}}_{\sigma}(E) \right|_{\eta}^{2} = \gamma_{L1,\sigma}^{2} \gamma_{NR,\sigma}^{2} \sum_{\eta} \frac{\left| \langle 1 | \phi_{\sigma}^{\eta} \rangle \right|^2 \left| \langle \phi_{\sigma}^{\eta} | N \rangle \right|^2}{\left( \tilde{\epsilon}_{\sigma}^{\eta} - E \right)^2 + \Gamma_{\eta,\sigma}^{2}}, \tag{4.12}$$

where $\Gamma_{p,\sigma}^{2}$ denotes the spin-depend escape rate determined by the Fermi's golden rule, i.e.,

$$\Gamma_{\eta,\sigma} = \frac{\gamma_{L1,\sigma} \langle 1 | \phi_{\sigma}^{\eta} \rangle + \gamma_{NR,\sigma} \langle \phi_{\sigma}^{\eta} | N \rangle}{2}. \tag{4.13}$$

$\langle 1 | \phi_{\sigma}^{\eta} \rangle$ and $\langle \phi_{\sigma}^{\eta} | N \rangle$ represent the site-orbital overlap matrix element between the end-sites and the extended molecule. The product of two site-orbital overlap matrixes represents the delocalization of the molecular orbital of the extended molecule.

$\gamma$ is a parameter to determine the $I$-$V$ characteristic and it is in proportion to a transition probability. To determine the $\gamma$ parameter, on the assumption of Dewar, Chatt and Duncanson (DCD) model [65, 66]. Luo et al. proposed a procedure that the occupied orbitals of the reservoirs interact with LUMO of the molecule according to the frontier orbital theory. Therefore, $\gamma$ can be written as

$$\gamma_{L1,\sigma}(\mathrm{LUMO}) = V_{L,\sigma}(\mathrm{LUMO})d^{*}_{1,\sigma}(\mathrm{LUMO}), \tag{4.14}$$

$$V^{2}_{L,\sigma}(\mathrm{LUMO}) = \frac{\left(\Delta E_{\sigma,\mathrm{HOMO-LUMO}} - \Delta E_{\sigma,\mathrm{LUMO}}\right)\Delta E_{\sigma,\mathrm{LUMO}}}{2}, \tag{4.15}$$

$$d^{2}_{1,\sigma}(\mathrm{LUMO}) = \frac{\sum_i c^{2}_{1,i,\sigma}}{\sum_{a,i} c^{2}_{a,i,\sigma}}, \tag{4.16}$$

where $\Delta E_{\sigma,\mathrm{HOMO-LUMO}}$ is the HOMO-LUMO gap of the extended molecule and $\Delta E_{\sigma,\mathrm{LUMO}}$ is the energy difference between the HOMO of reservoirs (gold clusters) and the LUMO of the isolated molecule which is not connected with the reservoirs. $d^{2}_{1,\sigma}(\mathrm{LUMO})$ is the square of an expansion coefficient of the wave function of the isolated molecule at the end-site.

In the system where LUMO of the molecule is non-degeneration, I can use Eq. (4.14, 4.15, 4.16). However, in the degenerating LUMO, I cannot apply the equations. So in the system I extend the equations to the degenerating system using the Boltzmann distribution. Here, assuming that Eq. (4.15) does not change in the degenerating LUMO, Eq. (4.14, 4.15, 4.16) become as the following,

$$\gamma_{L1,\sigma} = V_{L,\sigma}d^{*}_{1,\sigma}, \tag{4.17}$$

$$V_{L,\sigma} \approx V_{L,\sigma}(\mathrm{LUMO}), \tag{4.18}$$

$$\begin{aligned} d^{2}_{1,\sigma} &= \frac{\sum_k \exp\left[-\left(E_{\mathrm{LUMO}+k} - E_{\mathrm{LUMO}}\right)/RT\right] d_{\mathrm{LUMO}+k}}{\sum_k \exp\left[-\left(E_{\mathrm{LUMO}+k} - E_{\mathrm{LUMO}}\right)/RT\right]} \\ &= \frac{\sum_k B_k d_{\mathrm{LUMO}+k}}{\sum_k B_k}, \end{aligned} \tag{4.19}$$

where $k$ means the number of the degenerating orbitals around LUMO and $B_k$ is the Boltzmann distribution. In $k = 0$, (that is, the non-degenerating LUMO), Eq. (4.17, 4.18, 4.19) are equal to Eq.(4.14, 4.15, 4.16).

The total conduction current density is $I^{\mathrm{LR}} = Ai^{\mathrm{LR}}$, where $A$ is the effective injection area of the transmitting electron from the metal electrode, determined by the density of electronic states of the bulk gold. I have assumed that the effective injection area $A \approx \pi r_s^2$, where $r_s$ is defined as the radius of a sphere whose volume is equal to the volume per conduction electron, $r_s = (3/4\pi n)^{1/3}$, $n$ is the density of electronic states of the bulk gold [57].

# Chapter 5

# The Validity of the Developed Method

## 5.1 Introduction

Understanding electron transport through molecules remains one of the challenges in the emerging area of molecular electronics. Many researcher have studied the single molecules containing $\pi$ electrons to understand the electron transfer. However, in the realization of nano-device, it is unavoidable to have multiple molecular wires packed in proximity. If the wave function of one conductive electron mix with the conductive electron of the other molecular wire, it results in the unwanted transversal hopping of charge carriers. In view of this, one-dimensional metal string complexes can be a promising candidate.

The extended metal-atom chain (EMAC) complexes have attracted much interest in terms of a fundamental science and an application to molecular devices [67–80]. Peng et al. reported the syntheses of a series of EMAC complexes containing nickel atoms, such as $[\mathrm{Ni}_n\mathrm{L}_m(\mathrm{X})_2]$ (where L = the ligands, X = Cl or SCN). From the X-ray structure analysis, the peripheral ligands surrounded one-dimensionally aligned metal chains [67, 76]. From the XANES spectra, the terminal nickel(II) ions are high-spin ($S$ = 1), and inner nickel(II) ions are low-spin ($S$ = 0) [76]. A temperature-dependent magnetic study of these complexes indicated that there is a weak anti-ferromagnetic interaction between the two terminal high-spin nickel(II) ions, and depending on their chain length [67]. These weak anti-ferromagnetic interactions were demonstrated by using unrestricted DFT [77].

Recently, the measurements of the $I$-$V$characteristics and conductance of the EMAC complexes containing up to seven metal atoms were carried out by using conductive atomic force microscopy (c-AFM) measurements in vacuum [80]. These indicates the realization of the molecular wire using the one-dimensionally aligned metal ions. The first theoretical approach to the electron conductive of the EMAC complexes was carried out Hsu et al. [81]. They calculated its conductance using non-equilibrium Green's function (NEGF) based on the extended Huckel theory (EHT), and demon-

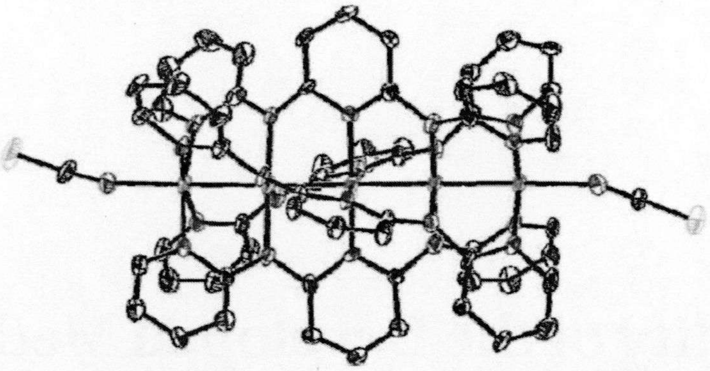

Figure 5.1: ORTEP view of the pentanickel complex, in general the metal atoms are colinear and wrapped helically by four ligands. Ni purple, N blue, S yellow, C gray. [This figure was taken from I. W. P. Chen et al. *Angew. Chem. Int. Ed.*, **45**, 5814 (2006)]

strated the measuring conductance. However, the EMAC complexes are the open-shell systems, so that the calculation of the current in the systems should be carried out the spin-polarized approach. In this chapter, I discuss the current of the EMAC complexes ($Ni_5L_4(NCS)_2$, L = oligo-$\alpha$-pyridylamine; Figure 5.1) by using the Green's function based on the spin polarized approach, and describe the importance and validity of the developed method.

## 5.2 Computational Details

Atomic coordinate of the EMAC complexes was taken from data of X-ray crystal structure analysis. I assumed as the following: 1) the EMAC molecule is connected to the Au electrode through the S-Au(111) junction at the bridge site, 2) the distance between the S atom and the Au surface is 2.3 Å, and 3) the distance Au-Au is 2.88 Å. All calculations were performed by unrestricted hybrid DFT (UB3LYP) [38] and set on Gaussian 03 [82].

For the calculation of the *I*-*V* characteristics of the systems, I used Eq.(5.1) as mentioned in section 4.3 (p. 44),

$$i_{\sigma}^{\mathrm{LR}} = \frac{1}{2}\sum_{\eta}\frac{emk_{\mathrm{B}}T}{2\pi^{2}\hbar^{3}}\int_{eV_{\mathrm{D}}}^{\infty}\left|\hat{\mathcal{T}}_{\sigma}(E)\right|_{\eta}^{2} f_{\sigma}(E)\mathrm{d}E, \tag{5.1}$$

$$f_{\sigma}(E) = \left\{\ln\left[1+\exp\left(\frac{E_{\mathrm{F},\sigma}+eV_{\mathrm{D}}-E}{k_{\mathrm{B}}T}\right)\right]-\ln\left[1+\exp\left(\frac{E_{\mathrm{F},\sigma}-E}{k_{\mathrm{B}}T}\right)\right]\right\}. \tag{5.2}$$

I set the temperature at 300 K to evaluate the *I*-*V* characteristics, and adopt the orbital from HOMO-9 to LUMO+9 as the orbital concerned with the conductivity.

Table 5.1: The calculated spin densities of $[Ni_5L_4(NCS)_2]$ complex for the BS-LS state.

| Atom[a] | Spin density |
|---|---|
| Ni1 | -1.59 |
| Ni2 | -0.11 |
| Ni3 | 0.00 |
| Ni4 | 0.10 |
| Ni5 | 1.59 |

[a] SCN-Ni1-Ni2-Ni3-Ni4-Ni5-NCS

Table 5.2: Experimental and theoretical current values (in eV) of the linear penta-nickel complex. [a] the experimental current values of the linear tri-nickel complex. [b] the calculated current value of the linear tri-nickel complex by using the NEGF-EHT [81].

| c-AFM | Calculation |
|---|---|
| ~ 8 | 5.11 |
| (~ 10)[a] | (16.0)[b] |

## 5.3 Results and Discussion

From the surface reflection IR spectrum, the terminal S atoms of the NCS connected to the Au atom, indicating that the EMAC complex containing the nickel(II) ions bind to the Au(111) surface to form a monolayer. As mentioned above, the terminal nickel(II) ions are highs-spin ($S$ =1), and the shows the anti-ferromagnetic interaction between the two terminal nickel(II) ions. The inner nickel(II) ions are low-spin ($S = 0$). The calculated spin densities of the complex for the broken-symmetry low-spin (BS-LS) state were summarized in Table 5.1. In this complex, spin densities are localized on the terminal nickel(II) ions. These results indicated that the terminal nickel(II) ions were open-shell ($S = 1$) and other inner nickel(II) ions were closed-shell ($S = 0$) structure, and which are consistent with experimental results.

Peng et al. measured the current values of the EMAC complexes by using the c-AFM measurement. In the c-AFM procedures, a gold-coted AFM tip is used to make direct contact with the monolayer while simultaneously measuring the $I$-$V$characteristics of the tip-molecule-substrate junction.

The experimental data were presented in Table 5.2. The data in the first column was obtained from the c-AFM measurement in vacuum. The calculated current value seems to be close to the data from the c-AFM measurement. This is reasonable result, because calculations were performed on a single molecular junction in vacuum, and also indicating that the spin-polarized approach is important for the open-shell systems.

The site-overlap elements and the coupling constants $\gamma$ are shown in Table 5.3. The dominant

Table 5.3: The coupling constant $\gamma$ (in eV), the orbital energies $E_\eta$ (in eV) and the overlap elements of the BDT connected the hollow site of Au(111) surface in the distance 2.6 Å. $\langle\text{Site}\rangle = |\langle 1|\phi^\eta_\sigma\rangle|^2 |\langle\phi^\eta_\sigma|N\rangle|^2$.

| | $\alpha$ orbital | | $\beta$ orbital | |
|---|---|---|---|---|
| | $\gamma_{1R}$ | 0.212 | $\gamma_{1R}$ | 0.287 |
| | $\gamma_{LN}$ | 0.672 | $\gamma_{LN}$ | 0.613 |
| | $E_\eta$ | $\langle$Site$\rangle$ | $E_\eta$ | $\langle$Site$\rangle$ |
| HOMO-9 | -5.710 | 0.225 | -5.723 | 0.368 |
| HOMO-8 | -5.657 | 0.034 | -5.642 | 0.015 |
| HOMO-7 | -5.581 | 0.000 | -5.559 | 0.004 |
| HOMO-6 | -5.531 | 0.000 | -5.550 | 0.006 |
| HOMO-5 | -5.478 | 0.000 | -5.481 | 0.000 |
| HOMO-4 | -5.464 | 0.000 | -5.468 | 0.000 |
| HOMO-3 | -5.429 | 0.000 | -5.430 | 0.000 |
| HOMO-2 | -5.257 | 0.000 | -5.263 | 0.000 |
| HOMO-1 | -4.893 | 0.000 | -4.896 | 0.000 |
| HOMO | -4.889 | 0.000 | -4.886 | 0.000 |
| LUMO | -2.657 | 0.000 | -2.651 | 0.000 |
| LUMO+1 | -2.626 | 0.000 | -2.631 | 0.000 |
| LUMO+2 | -1.952 | 0.000 | -1.931 | 0.000 |
| LUMO+3 | -1.913 | 0.000 | -1.916 | 0.000 |
| LUMO+4 | -1.760 | 0.000 | -1.786 | 0.000 |
| LUMO+5 | -1.619 | 0.000 | -1.627 | 0.000 |
| LUMO+6 | -1.504 | 0.000 | -1.483 | 0.000 |
| LUMO+7 | -1.473 | 0.000 | -1.473 | 0.000 |
| LUMO+8 | -1.415 | 0.000 | -1.419 | 0.000 |
| LUMO+9 | -1.243 | 0.000 | -1.242 | 0.000 |

site-overlap elements for the current are from HOMO-6 to HOMO-9 in alpha and beta orbitals (Figure 5.2). These orbitals are mainly distributed on the central metal strings ($d_{z^2}$ orbitals of the nickel atoms) and the sulfur atoms ($p_z$), indicating that the $d_{z^2}$ orbitals of the metal strings are dominant orbitals for the current flow through the EMAC, but the contribution from the peripheral ligands are small.

As mentioned above, Hsu et al. calculated the current values of the linear tri-metal complexes by using the NEGF-EHT [81]. Their calculated data was also summarized in Table 5.2. Their calculated current values are also close to the data from the c-AFM measurement as well as my calculated results. Moreover, they stated that the most important orbital for the conduction consisted mainly of the $d_{z^2}$ orbital with a much lower energy. These behaviors are similar to my calculated results. Both approaches show that the contributed orbitals for the electron conduction of the nickel string EMAC complex consist mainly of the $d_{z^2}$ orbital with orbitals of the lower energies.

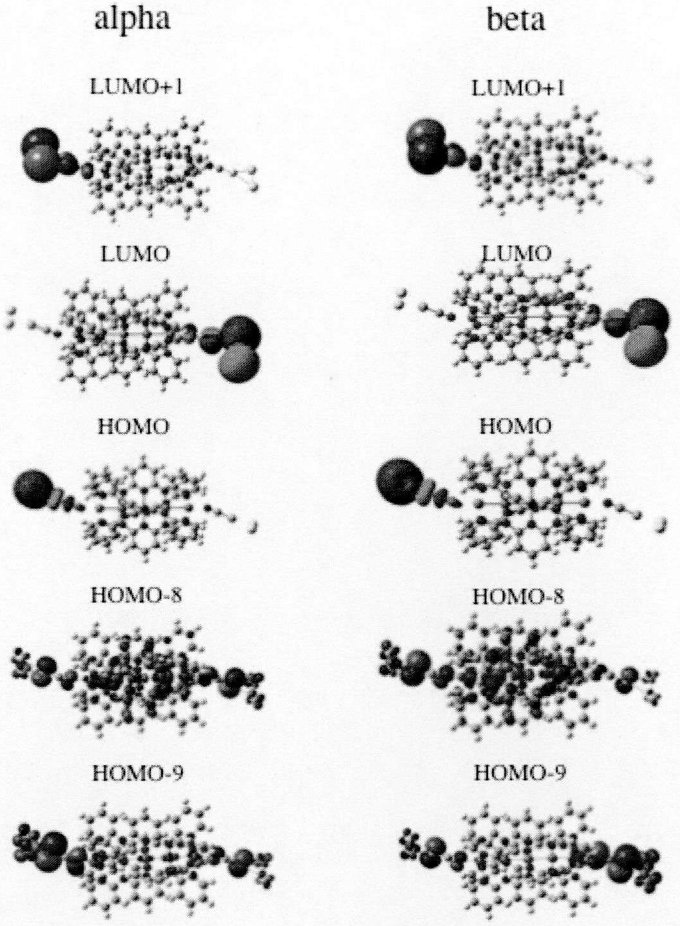

Figure 5.2: MO diagrams of the EMAC.

## 5.4 Conclusion

Taking the EMAC complexes as an example, I showed the validity of the developed method. The current values of the developed method agreed with the experimental values, indicating that the developed method is useful in the calculation of the current of the open-shell systems. The distribution of the orbital in tri- penta-nickel EMAC complexes are similar to each other from the developed method and the NEGF-EHF.

# Appendix

Hsu et al. calculated the current values of the EMAC using the NEGF-EHT [81]. Within the NEGF-EFT approach, the transmission function could be obtained as the following,

$$\begin{aligned} T(E) &= \mathrm{Tr}(\Gamma_{\mathrm{L}} G^{\mathrm{R}} \Gamma_{\mathrm{R}} G^{\mathrm{A}}) \\ &= \sum_{\mu\nu\lambda\sigma} (\Gamma_{\mathrm{L}})_{\sigma\lambda} (G^{\mathrm{R}})_{\lambda\mu} (\Gamma_{\mathrm{R}})_{\mu\nu} (G^{\mathrm{A}})_{\nu\sigma}, \end{aligned} \tag{5.3}$$

where $\sigma$, $\lambda$, $\mu$ and $\nu$ are the atomic orbital basis. The $G^{\mathrm{R(A)}}$ is called the retarded (advanced) Green's function,

$$\begin{aligned} G^{\mathrm{R}} &= \frac{1}{E - H_{\mathrm{mol}} - \Gamma^{\mathrm{R}}} \\ &= \sum_{ij} |i^{(0)}\rangle\langle i^{(0)}| \frac{1}{E - H_{\mathrm{mol}} - \Gamma} |j^{(0)}\rangle\langle j^{(0)}|, \end{aligned} \tag{5.4}$$

where $i$ and $j$ mean the molecular orbital basis. The retarded Green's function has the following relationship to the advanced Green's function,

$$G^{\mathrm{R}} = (G^{\mathrm{A}})^{\dagger}. \tag{5.5}$$

For simplicity, it assumes that the interaction between the molecule and the electrodes exists between the end atoms of the molecules and electrodes. This is similar to my approach. Eq(5.4) can be expanded using perturbation theory. The first-order energy correction can be calculated by considering the self-energy term as the perturbation term,

$$(G^{\mathrm{R}})_{\mu\nu} = \sum_{n} \frac{C^{(0)*}_{\mu n} C^{(0)}_{\nu n}}{E - \epsilon^{(0)}_{n} - \epsilon^{(1)}_{n}} \tag{5.6}$$

$$\epsilon^{(1)} = \langle n^{(0)} | \Sigma^{\mathrm{R}} | n^{(0)} \rangle \tag{5.7}$$

$$= \sum_{\mu\nu} C^{(0)*}_{\mu n} C^{(0)} (\Lambda_{\mu\nu} - i\Delta_{\mu\nu}) \tag{5.8}$$

where $C^{(0)}$ satisfies $\phi^{(0)}_{n} = \sum_{\mu} C^{(0)}_{\mu n} \varphi_{\mu}$. The $\Sigma^{\mathrm{R}}$ is the self-energy term, and stands for the interaction between the molecule and the electrodes. $\Lambda_{\mu\nu}$ and $\Delta_{\mu\nu}$ represent the real part and imaginary part of the self-energy, respectively. These terms show that the real part of the first-order energy correction is equivalent to a shift in energy and the imaginary part the broadening of the energy level.

Using the above Green's function, the transmission function represents as the following,

$$T(E)^{\text{NEGF-EHT}} = \frac{4\alpha^2|C_{1n}^{(0)}|^2|C_{Nn}^{(0)}|^2}{\left(E-\epsilon_n^{(0)}\right)^2 + \alpha^2\Big((|C_{1n}^{(0)}|^2 + |C_{Nn}^{(0)}|^2\Big)}, \tag{5.9}$$

where $\alpha$ is the imaginary part of the self-energy. This NEGF-EHT transmission function is equivalent in the developed transmission approach using Green's function,

$$\begin{aligned} T(E)^{\text{Dev}} &= \left|\hat{\mathcal{T}}_\sigma(E)\right|_\eta^2 \\ &= \Theta\frac{\left|\langle 1|\phi_\sigma^\eta\rangle\right|^2\left|\langle\phi_\sigma^\eta|N\rangle\right|^2}{\left(\epsilon_\sigma^\eta - E\right)^2 + \Gamma_{\eta,\sigma}^2}, \end{aligned} \tag{5.10}$$

where $\Theta$ means the coupling constant $(\gamma)$. Using $\phi_i = \sum_\mu C_{\mu i}\varphi_\mu$,

$$\langle 1|\phi_i\rangle = \sum_1\sum_\mu C_{1i}C_{\mu i}\mathbf{S}_{1\mu} \tag{5.11}$$

$$\mathbf{S}_{1\mu} = \int \varphi_\mu^*\varphi_1 \mathrm{d}\mathbf{r}, \tag{5.12}$$

where $\mathbf{S}_{1\mu}$ is the overlap matrix. Using the above relationship,

$$T(E)^{\text{NEGF-EHT}} \approx T(E)^{\text{Dev}} \tag{5.13}$$

Finally, the current formula can express as the following

$$I = \frac{2e}{h}\int [f(E,\mu_L) - f(E,\mu_R)]\,T(E)\mathrm{d}E. \tag{5.14}$$

# Part IV

# Electron Conductivity

# Chapter 6

# Benzene-dithiol Molecules

In previous chapter, I described the development of the theory for the electron conductivity of an open-shell system. In this and the following chapters, I describe the application of the developed theory. At first, I investigate the correlation of the electron conductivity with the stretching distance of the molecule-electrode contact.

## 6.1 Introduction

In the measurement of the conductance for the single molecule, a scanning tunneling microscope (STM) break junction and a mechanical break junction (MBJ) are widely used. As I mentioned above, The idea of the MBJ is to break by bending a very thin metal wire fabricated on the surface of an elastic substrate, thereby crating two electrodes. There are unresolved questions for an understanding of the experimental results in the break junction methods containing the STM and the MBJ.

Thiol group (-SH) is widely used as a linker of the molecule-electrode junction, and has the well-known property to be connected strongly to the Au electrodes. There are important problems for realizing the molecular devices. One of the problems is a stability and a breakdown mechanism of a linker-electrode bond. Huang et al. reported the problems for the single molecule covalently attached to two gold electrodes via Au-S bonds at room temperature using the STM break junction method [83]. They pointed out that the breakdown took place at the Au-Au bond near the molecule-electrode contacts. On the other hand, Qi et al. reported the junction broke at the S-Au bond [84]. They also pointed out that the breakdown took place at the Au-H bond by the H atom entering into interval between two Au atoms in the STM tip if one detached H atom was adsorbed to the Au tip. Then I am interested in the correlation of the electron conductivity with the stretching distance of the molecule-electrode contact. In the common sense, the electron conductivity almost does not exist if the distance between the linker and the electrode is long. However, it is important to under-

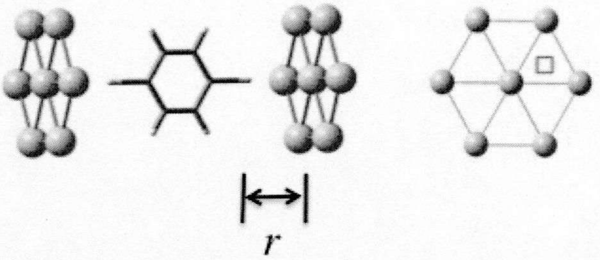

Figure 6.1: The scheme of the BDT molecule connected to the hollow site of Au(111) surface. $r$ is the distance between the BDT molecule and the Au cluster. □ means the location of the hollow site.

stand the correlation of the electron conductivity with the stretching distance. In order to investigate the correlation, I pointed out the spin polarization on the linker of the molecule-electrode contact in this chapter.

One Au atom is an open-shell system (radical) because the electron configuration is [Xe]$4f^{14}5d^{10}6s$. Therefore, the Au cluster is an open-shell system when the number of the Au atoms is odd numbers. When the distance between the surface of the Au electrode and sulfur atom is smaller than the equilibrium distance, the whole system becomes the close-shell system. However, the whole system becomes the open-shell system when the distance is longer than the equilibrium distance. These behaviors are similar to the dissociation of $H_2$. Therefore, when I investigate the electron conductivity involving the dissociation of the Au electrode and the sulfur atom, I need to use the unrestricted calculation.

## 6.2 Computational Details

In order to calculate the *I*-*V* characteristics of the BDT, I first optimized the geometry of the BDT. After that, I connected the optimized BDT to the hollow site of Au(111) surface as shown in Figure 6.1. As mentioned above, I used the results of DFT calculations for the *I*-*V* characteristics. These calculations were performed by UB3LYP [38] on the Gaussian03 program package [82]. Basis sets are 6-31G* for the BDT and LANL2DZ for Au atoms.

For the calculation of the *I*-*V* characteristics of the systems, I used Eq.(7.1) as mentioned in section 4.3 (p. 44),

$$i_\sigma^{\mathrm{LR}} = \frac{1}{2}\sum_\eta \frac{emk_{\mathrm{B}}T}{2\pi^2\hbar^3}\int_{eV_{\mathrm{D}}}^{\infty}\left|\hat{\mathscr{T}}_\sigma(E)\right|_\eta^2 f_\sigma(E)\mathrm{d}E, \tag{6.1}$$

$$f_\sigma(E) = \left\{\ln\left[1+\exp\left(\frac{E_{\mathrm{F},\sigma}+eV_{\mathrm{D}}-E}{k_{\mathrm{B}}T}\right)\right] - \ln\left[1+\exp\left(\frac{E_{\mathrm{F},\sigma}-E}{k_{\mathrm{B}}T}\right)\right]\right\}. \tag{6.2}$$

I set the temperature at 300 K to evaluate the *I*-*V* characteristics, and adopt the orbital from HOMO-9

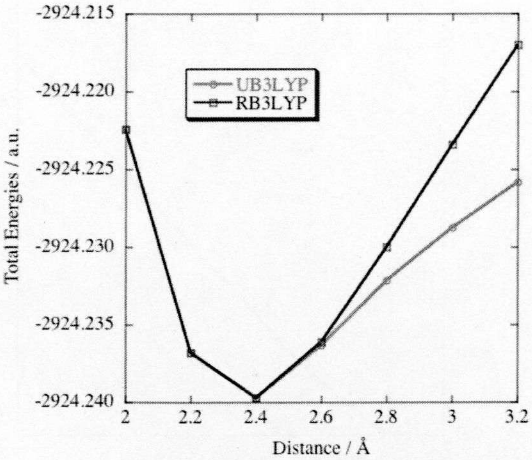

Figure 6.2: The potential energy surface of the BDT-Au.

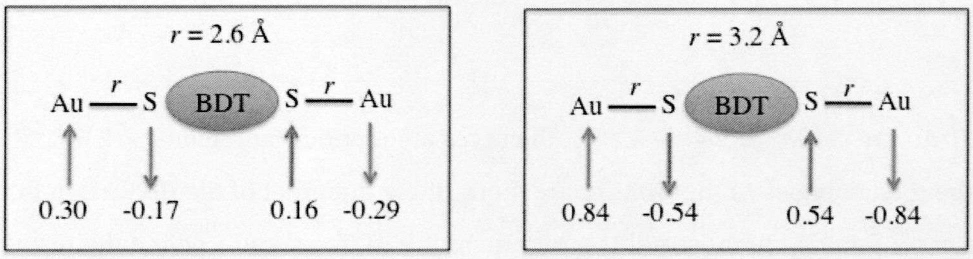

Figure 6.3: The schemes expressing the spin polarization of the BDT-Au in $r$ = 2.6 and 3.2 Å. The numerical values stand for the Mulliken spin densities.

to LUMO+9 as the orbital concerned with the conductivity.

## 6.3 Results and Discussion

### 6.3.1 Potential Energy Surface

The crucial problems in investigating the electron conductive are the evaluation of the interaction between the linker molecule and the electrode. Different methods have been proposed to estimate the interaction. In general, the interaction is interpreted as the electron coupling between the Au electrode and the end-site atom of the molecule. Simazaki et al. calculated the electron coupling by using non-diagonal elements of the Hamiltonian matrix for a benzene-dithiol (BDT) molecule connected to Au clusters. It is well-known that the electron coupling strongly depends on the distance between the Au electrode and the end-site atom of the molecule.

At first, I discuss the total energies for the BDT connected to the hollow site of Au(111) surface (BDT-Au) with the stretching distance between the Au cluster and the sulfur atom of the BDT molecule. For those total energies, I compare the RB3LYP with the UB3LYP. The potential energies

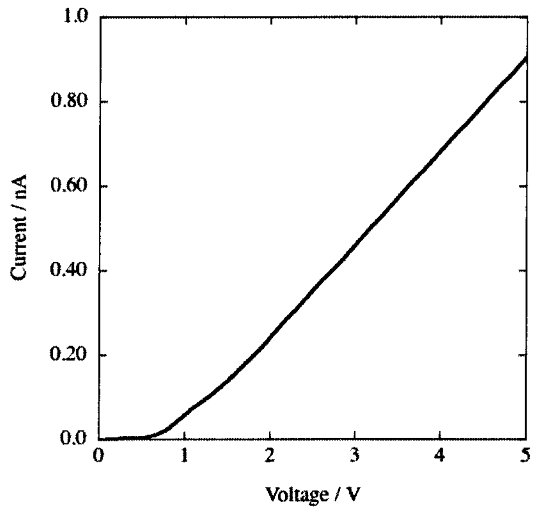

Figure 6.4: The *I*-*V* characteristics of the BDT molecule in the distance 2.4 Å.

for the BDT-Au are shown in Figure 6.2. Both curves are identical at region $r < 2.6$ Å. Beyond the distance, the total energies of the UB3LYP are more stable than that of the RB3LYP. In both curves, the distance $r = 2.4$ Å is the most stable structure of the BDT-Au, and I define the distance as the *model structure.*

By stretching the distance between the Au cluster and the sulfur atom, the covalent bond between the Au cluster and the sulfur atom breaks gradually, and finally the Au cluster exists alone without the covalent bond, where the localized spins polarize on the sulfur atoms of the BDT molecule as shown in Figure 6.3. The different of the total energies between the RB3LYP and the UB3LYP mainly originates from the spin polarization of the BDT molecule in the stretching distance $r = 2.8$ Å to 3.2 Å. Under such conditions, the RB3LYP cannot describe the correct electron states, so that the total energies of the UB3LYP are more stable. This phenomenon also be found in the dissociation of $H_2$, and is very well-known.

In summary, by stretching the distance the Au cluster and the sulfur atom of the BDT molecule, the UB3LYP curve moves to indicate the dissociation into the single Au cluster and the spin polarized BDT molecule while the RB3LYP curve gives to the incorrect results. In the stretching distance $r =$ 2.6 Å, although the total energy of the UB3LYP is almost equal to the that of the RB3LYP, the localized spins somewhat exist on the sulfur atom of the BDT-Au in the UB3LYP calculation. This causes the interesting phenomenon for the electron conductivity of the BDT-Au as being discussed after section.

Table 6.1: The coupling constant $\gamma$ (in eV), the orbital energies $E_\eta$ (in eV) and the overlap elements of the BDT connected to the hollow site of Au(111) surface in the distance 2.4 Å. ⟨Site⟩ = $\left|\langle 1|\phi^{\eta}_{\sigma}\rangle\right|^2 \left|\langle\phi^{\eta}_{\sigma}|N\rangle\right|^2$.

| $\gamma_{1R} = 0.042$<br>$\gamma_{1R} = 0.040$ | | |
|---|---|---|
| | $E_\eta$ | ⟨Site⟩ |
| HOMO-9 | -7.584 | 0.001 |
| HOMO-8 | -7.181 | 0.016 |
| HOMO-7 | -7.167 | 0.000 |
| HOMO-6 | -7.034 | 0.000 |
| HOMO-5 | -6.712 | 0.092 |
| HOMO-4 | -6.692 | 0.011 |
| HOMO-3 | -6.235 | 1.257 |
| HOMO-2 | -6.102 | 0.000 |
| HOMO-1 | -5.992 | 0.016 |
| HOMO | -5.283 | 0.638 |
| LUMO | -4.256 | 0.002 |
| LUMO+1 | -4.192 | 0.000 |
| LUMO+2 | -4.133 | 0.001 |
| LUMO+3 | -4.050 | 0.062 |
| LUMO+4 | -3.279 | 0.000 |
| LUMO+5 | -3.170 | 0.016 |
| LUMO+6 | -2.477 | 0.000 |
| LUMO+7 | -2.472 | 0.000 |
| LUMO+8 | -1.446 | 0.000 |
| LUMO+9 | -1.436 | 0.000 |

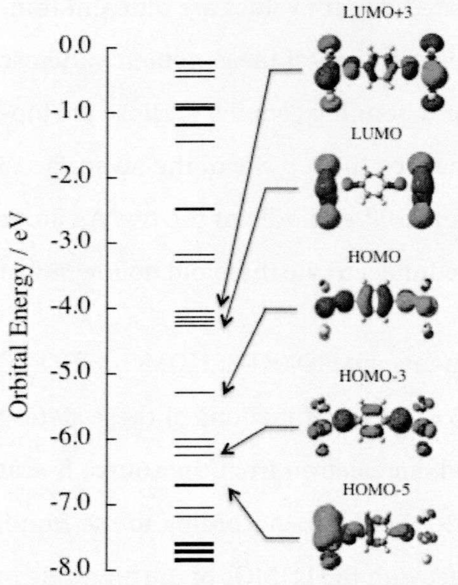

Figure 6.5: The MO diagram of the BDT in the distance 2.4 Å.

### 6.3.2 The *I*-*V* Characteristics in the Model Structure

In this section, I discuss the *I*-*V* characteristics of the BDT molecule in the model structure. In previous section, I found that the stretching distance in the most stable energy was 2.4 Å, and in the distance, the whole system is the closed-shell system. The DFT results were utilized i.e. Kohn-Sham orbital energies and the site-orbital overlap matrix elements (simply transcribed as overlap element hereafter) for these calculations. The lack of the correlation energy in the Hartree-Fock (HF) method can be a defect for the estimation of the *I*-*V* characteristics, and it takes a lot of time to estimate it in the post HF method. For those of viewpoints, the DFT is widely used to estimate the *I*-*V* characteristics.

The molecular orbitals having large overlap element values delocalize over all the site of the molecule, leading to contributing to the electron conduction. In the distance 2.4 Å, LUMO and LUMO+1 are degenerate. So, I adopted both LOMO and LUMO+1 for the calculation of the coupling constants. These parameters in the distance 2.4 Å were summarized in Table 6.1. The *I*-*V* curves were shown in Figure 6.4.

The onset of the current is 0.7 eV, and the calculated current value at 1V is 0.058 nA. Although the onset of the current is similar to the experimental result reported by Reed et al. [2] and Ulrich et al. [46] and so on, the calculated current values are different from the experimental results. This discrepancy takes place in the experimental measurements themselves [2, 4, 46–48]. For a one of the reason, there are distinct Au-S bonding geometry. Those are top-molecule-top geometry, where both S atoms of the molecule occupy the top site of the Au surface, bridge-molecule-bridge geometry where both S atoms connect to the middle of the two Au atoms and hollow-molecule-hollow geometry, where both S atoms connect to the threefold hollow site of Au electrodes.

The dominant overlap elements are HOMO-5, HOMO-3, HOMO and LUMO+3. These orbitals were summarized in Figure 6.5. The wavefunctions of these states are extended over the BDT-Au. In the elastic scattering method, an electron from the source is scattered through the unoccupied molecular orbital and reaches to the drain. According to the frontier orbital theory, the occupied electrode orbitals mainly interact with the LUMOs of the molecule in case of the closed-shell calculation. The coupling constants in the each end-side are almost equal to each other ($\gamma_1 = \gamma_N$) because of the symmetrical structure and the closed-shell system.

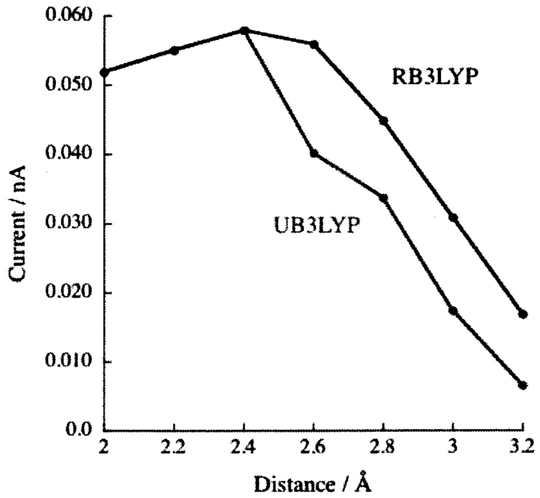

Figure 6.6: The current values at 1 V and the stretching distance between the sulfur atoms of the BDT and the Au clusters using UB3LYP and RB3LYP calculation methods.

Table 6.2: The coupling constant $\gamma$ (in eV), the orbital energies $E_\eta$ (in eV) and the overlap elements of the BDT connected the hollow site of Au(111) surface in the distance a) 2.6 Å and b) 3.2 Å. ⟨Site⟩ = $|\langle 1|\phi^{\eta}_{\sigma}\rangle|^2|\langle\phi^{\eta}_{\sigma}|N\rangle|^2$.

a) 2.6 Å

| | α orbital | | β orbital | |
|---|---|---|---|---|
| | $\gamma_{1R}$ | 0.053 | $\gamma_{1R}$ | 0.022 |
| | $\gamma_{LN}$ | 0.023 | $\gamma_{LN}$ | 0.052 |
| | $E_\eta$ | ⟨Site⟩ | $E_\eta$ | ⟨Site⟩ |
| HOMO-9 | -7.602 | 0.000 | -7.601 | 0.000 |
| HOMO-8 | -7.154 | 0.013 | -7.155 | 0.016 |
| HOMO-7 | -7.126 | 0.000 | -7.125 | 0.000 |
| HOMO-6 | -7.031 | 0.000 | -7.032 | 0.000 |
| HOMO-5 | -6.834 | 0.000 | -6.844 | 0.001 |
| HOMO-4 | -6.807 | 0.000 | -6.796 | 0.000 |
| HOMO-3 | -6.225 | 0.353 | -6.225 | 0.371 |
| HOMO-2 | -6.082 | 0.410 | -6.086 | 0.393 |
| HOMO-1 | -5.940 | 0.907 | -5.941 | 0.801 |
| HOMO | -5.161 | 0.147 | -5.163 | 0.155 |
| LUMO | -4.294 | 0.001 | -4.293 | 0.000 |
| LUMO+1 | -4.238 | 0.000 | -4.238 | 0.000 |
| LUMO+2 | -4.187 | 0.012 | -4.187 | 0.015 |
| LUMO+3 | -4.078 | 0.088 | -4.080 | 0.089 |
| LUMO+4 | -3.334 | 0.000 | -3.335 | 0.000 |
| LUMO+5 | -3.241 | 0.001 | -3.239 | 0.001 |
| LUMO+6 | -2.527 | 0.000 | -2.528 | 0.000 |
| LUMO+7 | -2.463 | 0.000 | -2.461 | 0.000 |
| LUMO+8 | -1.485 | 0.000 | -1.490 | 0.000 |
| LUMO+9 | -1.477 | 0.000 | -1.472 | 0.000 |

b) 3.2 Å

| | α orbital | | β orbital | |
|---|---|---|---|---|
| | $\gamma_{1R}$ | 0.031 | $\gamma_{1R}$ | 0.014 |
| | $\gamma_{LN}$ | 0.013 | $\gamma_{LN}$ | 0.029 |
| | $E_\eta$ | ⟨Site⟩ | $E_\eta$ | ⟨Site⟩ |
| HOMO-9 | -7.559 | 0.000 | -7.559 | 0.000 |
| HOMO-8 | -7.454 | 0.000 | -7.454 | 0.000 |
| HOMO-7 | -7.127 | 0.002 | -7.127 | 0.002 |
| HOMO-6 | -7.068 | 0.001 | -7.071 | 0.000 |
| HOMO-5 | -7.025 | 0.008 | -7.026 | 0.005 |
| HOMO-4 | -6.923 | 0.000 | -6.919 | 0.000 |
| HOMO-3 | -6.661 | 0.516 | -6.660 | 0.406 |
| HOMO-2 | -6.381 | 0.374 | -6.383 | 0.353 |
| HOMO-1 | -6.142 | 0.489 | -6.141 | 0.431 |
| HOMO | -5.118 | 0.010 | -5.117 | 0.009 |
| LUMO | -4.336 | 0.000 | -4.333 | 0.000 |
| LUMO+1 | -4.307 | 0.000 | -4.309 | 0.000 |
| LUMO+2 | -4.227 | 0.125 | -4.227 | 0.048 |
| LUMO+3 | -4.094 | 0.006 | -4.095 | 0.010 |
| LUMO+4 | -3.447 | 0.000 | -3.447 | 0.000 |
| LUMO+5 | -3.347 | 0.000 | -3.347 | 0.000 |
| LUMO+6 | -2.608 | 0.000 | -2.607 | 0.000 |
| LUMO+7 | -2.405 | 0.000 | -2.406 | 0.000 |
| LUMO+8 | -1.642 | 0.000 | -1.644 | 0.000 |
| LUMO+9 | -1.613 | 0.000 | -1.611 | 0.000 |

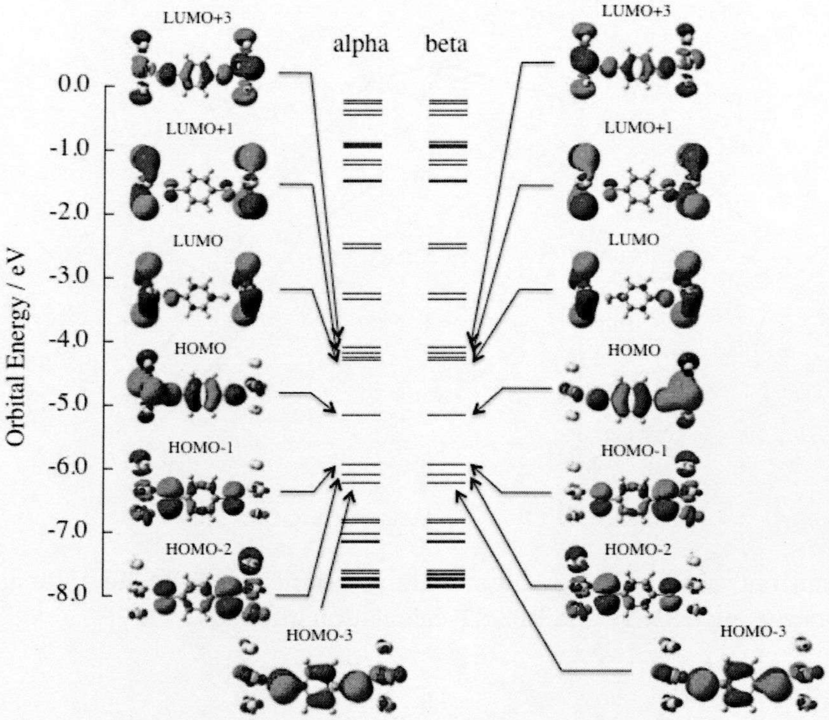

Figure 6.7: The MO diagram of the BDT connected the hollow site of Au(111) surface in the distance 2.6 Å.

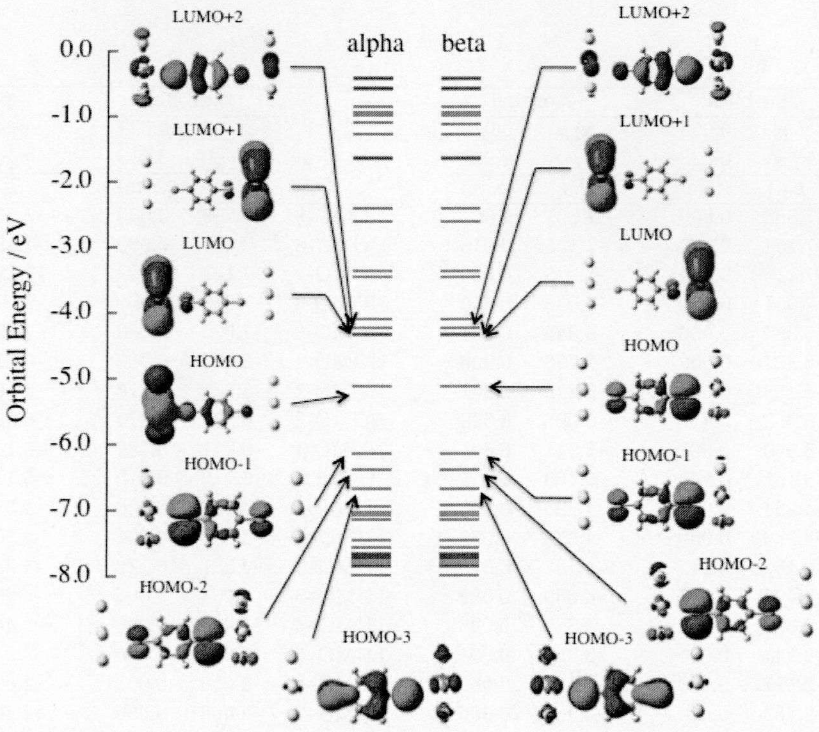

Figure 6.8: The MO diagram of the BDT connected the hollow site of Au(111) surface in the distance 3.2 Å.

### 6.3.3 Correlation of the Stretching Distance with the *I*-*V* Characteristics

As well as the dissociation of $H_2$ molecule, if the distance between the sulfur atoms of the BDT molecule and the Au cluster is longer, the whole systems becomes the open-shell systems because of the spin polarization of the BDT molecule. From the viewpoint of this, I investigated the correlation of the bonding distance with the *I*-*V* characteristics. In order to calculate the coupling constants, I adopted both LOMO and LUMO+1 because LUMO and LUMO+1 were degenerate. The *I*-*V* characteristics to the stretching distance were shown in Figure 6.6. In the distance from 2.0 Å to 2.4 Å, the current value is smaller (or almost constant) in the short distance. It indicates that if the bonding distance is shorter than the stable bonding distance (2.4 Å), the current value is somewhat smaller or almost constant. However, if the bonding distance is larger than the stable bonding distance, the current value extremely becomes small. The change of the current values in the bonding distance from 2.4 Å to 2.6 Å is large. The reason of the change seems the spin polarization of the BDT molecule. As mentioned in previous section, in the distance from 2.6 Å to 3.2 Å, the BDT molecules are the spin polarization, and the current values linearly decrease with the distance.

In the distance 2.6 Å, the current value at 1 V is 0.040 nA. The coupling constants ($\gamma$), the orbital energies, and the overlap elements are summarized in Table 6.2 a). The dominant overlap elements are HOMO-3, HOMO-2, HOMO-1, HOMO and LUMO+3 for both $\alpha$ and $\beta$ orbitals. These orbitals expand over the extended molecule as shown in Figure 6.7. The coupling constant $\gamma_1$ is different from another coupling constant $\gamma_N$ because of the spin polarization of the BDT. In LUMO of the alpha orbital, the MO coefficient of the sulfur atom is large only on the left side, but in LUMO+1, the coefficient is large on the both side. So, the coupling constant becomes large only on the one-side even if the degeneration of LUMO and LUMO+1 are considered. In the distance 3.2 Å, the dominant overlap elements are HOMO-3, HOMO-2, HOMO-1, HOMO, LOMO+2 for both $\alpha$ and $\beta$ orbitals as summarized in Table 6.2 b). These orbitals are also expand over the BDT molecule, but the extent on the Au clusters is small because the distance between the sulfur atom and Au cluster is long, as shown in Figure 6.8. The coupling constants in the distance 3.2 Å are smaller than in the distance 2.6 Å. LUMO and LUMO+1 in the distance 3.2 Å localize on the one-side of the end-sites. Therefore, the coupling constants become small values.

## 6.4 Conclusion

Investing the electron conductivity, the interaction between the sulfur atom and the electrodes are important. In this chapter, I discuss the effect of the spin polarization in the electron transfer of the BDT molecule. In my calculated results, the electron conductivity becomes small if the spin generates on the end-site.

# Chapter 7

# Artificial Metal-DNA

## 7.1 Introduction

Molecular devices have attracted much attention in a research field of nanoelectronics because of a limitation on a miniaturization of conventional silicon-based devices. For example, it is expected that a top down approach reaches a drastic limit at 100 nm [41]. In molecular devices, especially in a molecular wire, delocalization of a $\pi$-electron cloud is useful for an electron conductivity. On the other hand, DNA is well known not only as the molecule containing all genetic information, but also as a possible candidate for the molecular wire along the $\pi$-stacking axis. In order to utilize DNA for the molecular wire, a large number of studies on the mechanism of the electron transfer in DNA molecule have been reported [9–19]. However, little is known about whether DNA is a conductor or not. Zhang et al. obserbed a low electron conductivity of a DNA wire, and concluded that the DNA wire was the typical insulator [13]. On the other hands, Kasumov et al. reported that DNA molecules could be a good conductor [17]. From the theoretical studies, Tada et al. reported that DNA molecules were the semi-conductor if the base was directly connected with the gold leads, but were insulator if the sugar-phosphates were connected with the gold leads [18]. In this way, there are contrary opinions on the DNA conductor.

On the other hand, there are several attempts to synthesize novel DNA-based compounds to achieve the DNA conductor. One of the promising candidates is a metal-complexed DNA (M-DNA). This system is expected to conduct an electric current through the redox of the metal atom. A coordination of DNA to metal ions causes a change in the structure and the physical properties. Especially, the complex formation sometimes brings problems that a double helical structure of DNA becomes loose, and that a linear one-dimensional chain of the DNA duplex is damaged by the large transformation. For example, a cisplatin, which is known as an anticancer drug, attaches to the outer region of DNA duplex and distorts the structure of the duplex [85–88]. Therefore it is considered to be a disadvantage to arrange the metal ion on the outside of the DNA duplex. While, an incorporation of the metal ions into the inner region of the DNA duplex has been attempted in recent years. One of the examples is an artificial M-DNA.

As mentioned above, DNA has a double-helical structure made from a complementary hydrogen bonding pair called the Watson-Crick base pair, and is stabilized by a $\pi-\pi$ stacking interaction. Tanaka et al. succeeded in making complex by putting $Cu^{2+}$ ions into the DNA double helix using the hydroxypyridone (**H**) ligand as an artificial nucleoside [20]. Here, it is transcribed as **H**-$Cu^{2+}$-**H**. The merit of the material is the replacement of the Watson-Crick base pair in the natural DNA by the coordinate bond of metal [89]. An existence of the ferromagnetic interaction between electron spins on adjacent $Cu^{2+}$ ions has also been found by using an electron paramagnetic resonance (EPR) spectra, [20] suggesting that this has a possibility for spintronics [90] of DNA wire. From those points of view, it is interesting to investigate on the magnetism and the electron transport on this system.

The first theoretical calculation on the magnetism of this system was reported by Zhang et al. [91]. They showed that the ferromagnetic (F) and the anti-ferromagnetic (AF) phases were energetically almost degenerate. Jishi et al. also calculated the total energy of [**H**-$Cu^{2+}$-**H**] with three different symmetries [92]. On the other hand, I demonstrated that the thermal excitation from the anti-ferromagnetic (AF) state to the ferromagnetic (F) state would occur in the system by the Boltzmann distribution simulation based on calculated effective exchange integral ($J_{ab}$) values [93]. Mallajosyula and Pati also reported that an optical conductivity showed a peak of a low frequency excitation at 0.8 eV [94]. In addition, according to my previous density functional theory (DFT) studies [95] with an Anderson-Langreth-Lindqvist van der Waals (vdW) functional [96], the spin-spin interaction among $Cu^{2+}$ ions was not important for the stacking stabilization of **H**-$Cu^{2+}$-**H**, and I could reproduce the experimental distance between $Cu^{2+}$ ions.

Another development of an artificial M-DNA was carried out by Clever et al. using salen (**S**) ligands in which a variety of metal ions could be introduced as coordination partners [21, 97]. An advantage of the salen ligand is that the ethylenediamine, which is used to assemble the metal-salen complexes inside the DNA double strand, forms a covalent crosslink, and brings a high stability to the duplex. This system showed a weak anti-ferromagnetic interaction from theoretical studies [98, 99]. Afterward, Clever et al. reported that this system experimentally showed anti-ferromagnetic interaction [100, 101].

My another interest on the artificial M-DNAs is to calculate the I-V characteristics. Up to now, various artificial M-DNAs [102, 103] and artificial nucleosides [104–108] have been reported. However, the electron conductivities of the artificial M-DNA have not been reported yet in spite of that there are many reports on the electron conductivity of a natural DNA. Therefore, it is necessary to examine the electron conductivity of the artificial M-DNAs to understand the effect of metal ions. Mallajosyula and Pati also have pointed out its importance in their theoretical perspective [109].

From above reasons, this paper aims to investigate on the *I-V* characteristics on the artificial M-DNAs, [ **H**-$Cu^{2+}$-**H**] and [ **S**-$Cu^{2+}$-**S**] systems. Effects of spin states, metal ions and the backbone are examined by using the elastic scattering Green's function approach based on DFT.

Finally, it should be noted that there are many calculated reports about electron structures of DNA using the DFT method, which does not involve $\pi-\pi$ interaction well, but those results indicate that the density matrix of the DFT can be applicable to a qualitative discussions of the properties. (for example, see ref [19] and [110]) In addition, it is also important for the electron transport in DNA to consider the effect of water molecules and counter-ions, although I carried out all calculationa in the gas phase, as a first step for the elucidation of the electron conductivity of these systems.

## 7.2 Computational Details

### 7.2.1 Modeling of the systems

In this study, I examined the *I-V* characteristics of two types of the artificial M-DNAs, hydroxypyridone (**H**) [20] and salen (**S**) [21] complexes. In order to calculate the *I-V* characteristics for both of the systems, I first optimized the geometry of monomer structures of [**H**-$Cu^{2+}$-**H**] and [**S**-$Cu^{2+}$-**S**], where [**X**-$Cu^{2+}$-**X**] (**X** = **H** and **S**) means one monomer. As model structures, the backbone was replaced by S atoms.

The dimer models for both of the systems were constructed by using the optimized monomer. I assumed that the rotation angle was 36° clockwise. The distances of adjacent planes of $[\mathbf{H}\text{-}Cu^{2+}\text{-}\mathbf{H}]_2$ and $[\mathbf{S}\text{-}Cu^{2+}\text{-}\mathbf{S}]_2$ are 3.7 Å [20] and 3.375 Å [21], respectively. Note that a distance of the adjacent base pair of salen-complexed DNA is recently estimated 3.7 Å by Clever et al. (see ref. [100]). However, the distance of 3.375 Å is chosen. The bond lengths of Au-Au and the distance between a S atom and the gold cluster surface is fixed to 2.88 Å and 2.3 Å, respectively [58]. Finally, the models of the artificial M-DNAs were connected to the hollow site of Au(111) surface as illustrated in Figure 7.1.

### 7.2.2 Calculation Method

As mentioned above, I used the results of DFT calculations for the *I-V* characteristics. These calculations were performed by UB3LYP [38] on the Gaussian03 program package [82]. Basis sets used

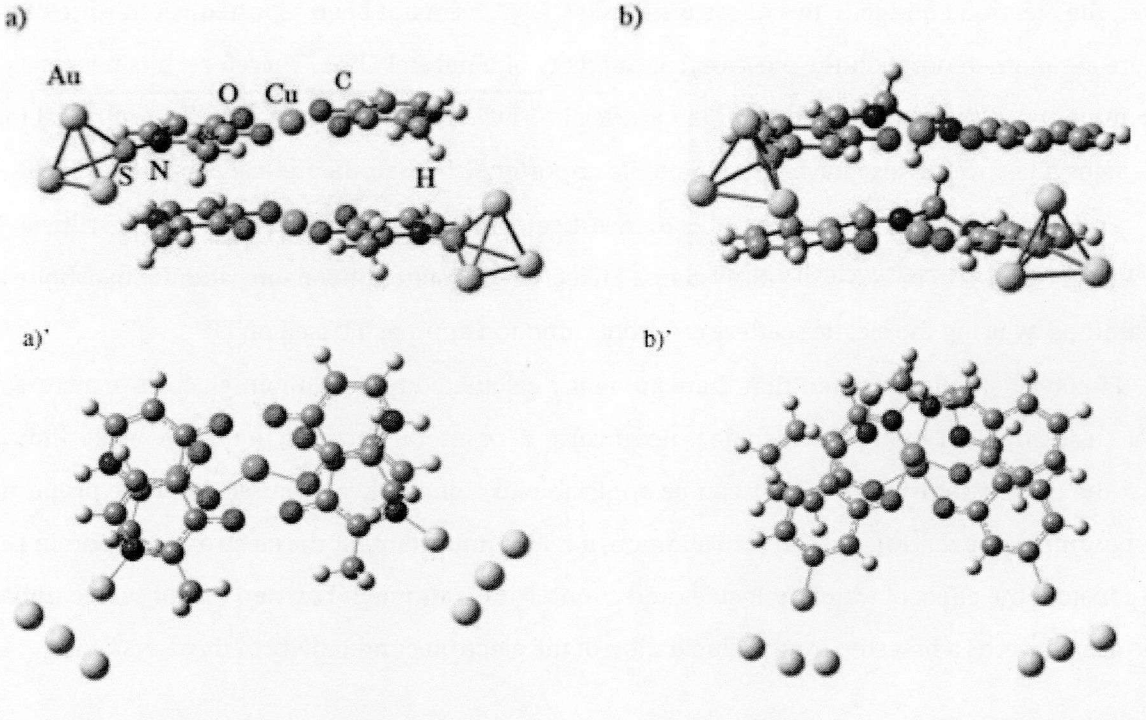

Figure 7.1: The calculated dimer models of $Cu^{2+}$ mediated base pairs of a) $[\mathbf{H}\text{-}Cu^{2+}\text{-}\mathbf{H}]_2$ and b) $[\mathbf{S}\text{-}Cu^{2+}\text{-}\mathbf{S}]_2$. a)′ and b)′ are the top view. The backbone is replaced by S atoms in the models and connected to the hollow site model structures on Au(111) surface.

for the ligands were 6-31G* for the geometry optimization and 6-31+G* for the single point energy calculations. Huzinaga MIDI+pd basis set [114] and LANL2DZ were used for Cu and Au atoms, respectively.

For the calculation of the *I*-*V* characteristics of the systems, I used Eq.(7.1) as mentioned in section 4.3 (p. 44),

$$i_{\sigma}^{\mathrm{LR}} = \frac{1}{2}\sum_{\eta} \frac{emk_{\mathrm{B}}T}{2\pi^2\hbar^3} \int_{eV_{\mathrm{D}}}^{\infty} \left|\hat{\mathscr{T}}_{\sigma}(E)\right|_{\eta}^{2} f_{\sigma}(E)\mathrm{d}E, \tag{7.1}$$

$$f_{\sigma}(E) = \left\{ \ln\left[1+\exp\left(\frac{E_{\mathrm{F},\sigma}+eV_{\mathrm{D}}-E}{k_{\mathrm{B}}T}\right)\right] - \ln\left[1+\exp\left(\frac{E_{\mathrm{F},\sigma}-E}{k_{\mathrm{B}}T}\right)\right]\right\}. \tag{7.2}$$

I set the temperature at 300 K to evaluate the *I*-*V* characteristics, and adopt the orbital from HOMO-9 to LUMO+9 as the orbital concerned with the conductivity.

Table 7.1: Total energies, $\langle \hat{S}^2 \rangle$ of the HS and the BS LS states and $J_{ab}$ values of [H-Cu$^{2+}$-H]$_2$ and [S-Cu$^{2+}$-S]$_2$.

| | HS | | BS LS | | |
|---|---|---|---|---|---|
| Models | Total Energy$^a$ | $\langle \hat{S}^2 \rangle$ | Total Energy$^a$ | $\langle \hat{S}^2 \rangle$ | $J_{ab}^b$ |
| [H-Cu$^{2+}$-H]$_2$ | -6638.24939334 | 2.0242 | -6638.24939822 | 1.0286 | -1.1 |
| [S-Cu$^{2+}$-S]$_2$ | -6644.51516521 | 2.0062 | -6644.51517229 | 1.0063 | -1.6 |

$^a$ in a.u.
$^b$ in cm$^{-1}$

## 7.3 Results and Discussion

### 7.3.1 Total Energies

Before the $I$-$V$ characteristics of the systems are discussed, let us consider the total energies of the systems. The total energies, $\langle \hat{S}^2 \rangle$ and $J_{ab}$ are shown in Table 7.1. The total energies of the HS and BS LS states of [H-Cu$^{2+}$-H]$_2$ and [S-Cu$^{2+}$-S]$_2$ are almost degenerate, but the BS LS state is somewhat more stable than HS state. It indicates that the thermal excitation from the BS LS state to the HS state occurs in these systems. The $J_{ab}$ values in the Table 7.1 mean the Effective Exchange Integral value depending on the total energy. The positive $J_{ab}$ value means ferromagnetic interaction, and the negative value means anti-ferromagnetic interaction. The $J_{ab}$ values of these systems are very small and negative values, that is, both these systems are weak anti-ferromagnetism. The details of the $J_{ab}$ values and the magnetism of these systems are described in Chapter 8 (p. 89).

### 7.3.2 Comparison of High-Spin State with Broken-Symmetry Low-Spin State

In this section, I analyze the $I$-$V$ characteristics especially in terms of a comparison between the HS and the BS LS states here.

I summarized the calculated coupling constant ($\gamma$) values in Table 7.2 and the current values at 1V in Table 7.3 for the HS and the BS LS states. In [H-Cu$^{2+}$-H]$_2$ model, LUMO and LUMO+1 are degenerate. So, I adopted both LUMO and LUMO+1 for the calculation of the coupling constants. On the other hand, in [S-Cu$^{2+}$-S]$_2$ model, I included from LUMO to LUMO+3. The DFT results are utilized i.e. Kohn-Sham orbital energies and the site-orbital overlap matrix elements (simply transcribed as overlap element hereafter) for these calculations. These parameters were summarized in Table 7.4 and Table 7.5. The $I$-$V$ curves were shown in Figure 7.2.

Table 7.2: The coupling constants $\gamma$ (in eV) of each orbital for a) the [H-Cu$^{2+}$-H]$_2$ and b) the [S-Cu$^{2+}$-S]$_2$ in the HS and the BS LS states. $\gamma = \gamma_{1R}\gamma_{LN}$.

a) [H-Cu$^{2+}$-H]$_2$

| | HS | | | BS LS | |
|---|---|---|---|---|---|
| | $\alpha$ orbital | $\beta$ orbital | | $\alpha$ orbital | $\beta$ orbital |
| $\gamma_{1R}$ | 0.207 | 0.210 | $\gamma_{1R}$ | 0.097 | 0.274 |
| $\gamma_{LN}$ | 0.336 | 0.312 | $\gamma_{LN}$ | 0.197 | 0.258 |
| $\gamma$ | 0.070 | 0.066 | $\gamma$ | 0.019 | 0.071 |

b) [S-Cu$^{2+}$-S]$_2$

| | HS | | | BS LS | |
|---|---|---|---|---|---|
| | $\alpha$ orbital | $\beta$ orbital | | $\alpha$ orbital | $\beta$ orbital |
| $\gamma_{1R}$ | 0.127 | 0.212 | $\gamma_{1R}$ | 0.068 | 0.199 |
| $\gamma_{LN}$ | 0.154 | 0.236 | $\gamma_{LN}$ | 0.081 | 0.256 |
| $\gamma$ | 0.020 | 0.056 | $\gamma$ | 0.006 | 0.051 |

Table 7.3: The current values (in nA) at 1V of each orbital for the [H-Cu$^{2+}$-H]$_2$ and the [S-Cu$^{2+}$-S]$_2$ in the HS and the BS LS states.

| [H-Cu$^{2+}$-H]$_2$ | | | [S-Cu$^{2+}$-S]$_2$ | | |
|---|---|---|---|---|---|
| | HS | BS LS | | HS | BS LS |
| $\alpha$ orbital | 1.45 | $4.82 \times 10^{-3}$ | $\alpha$ orbital | 0.304 | 0.0356 |
| $\beta$ orbital | 1.46 | 0.117 | $\beta$ orbital | 1.51 | 1.20 |
| Total | 2.91 | 0.122 | Total | 1.81 | 1.22 |

### The Hydroxypyridone Type M-DNA

In the HS state of [H-Cu$^{2+}$-H]$_2$ model, the current values for $\alpha$ and $\beta$ orbitals at 1V are $i_\alpha = 1.45$ nA and $i_\beta = 1.46$ nA, and the total current is $i_{\alpha+\beta} = 2.91$ nA, respectively. In the Luo's approach [57, 58], the important parameter to determine the current of the molecular wire is the coupling constant ($\gamma$). In the elastic scattering method, an electron from the source is scattered through the unoccupied molecular orbital and reaches to the drain. According to the frontier orbital theory, the occupied electrode orbitals mainly interact with the LUMOs of the molecule in case of the closed-shell calculation. In this calculation, however, the coupling constants of each end-site (1, N), $\gamma_{1\alpha(\beta)}$ and $\gamma_{N\alpha(\beta)}$, might be different from each other ($\gamma_{1\alpha(\beta)} \neq \gamma_{N\alpha(\beta)}$) because of the BS approach and the antisymmetry of the molecule. (In the case of a symmetrical molecule, e.g. the benzene dithiol molecule, the parameters are strictly equal to each other ($\gamma_{1\alpha(\beta)} = \gamma_{N\alpha(\beta)}$) [57, 58]. As shown in Table 7.2(a), the $\gamma_\alpha$ value is almost equal to $\gamma_\beta$ value, and there is no difference in the magnitude of the current between $\alpha$ and $\beta$ orbitals. The overlap element, which shows the contribution of each orbital for the electrical conduction, indicates that HOMO-9, HOMO-7 and HOMO-6 for $\alpha$ orbital, and HOMO-8, HOMO-5 and HOMO-4 for $\beta$ orbitals have a large orbital overlap as summarized in Table 7.4. These MO diagrams are showed in Figure 7.3a). It is found that these orbitals mainly delocalizes over both

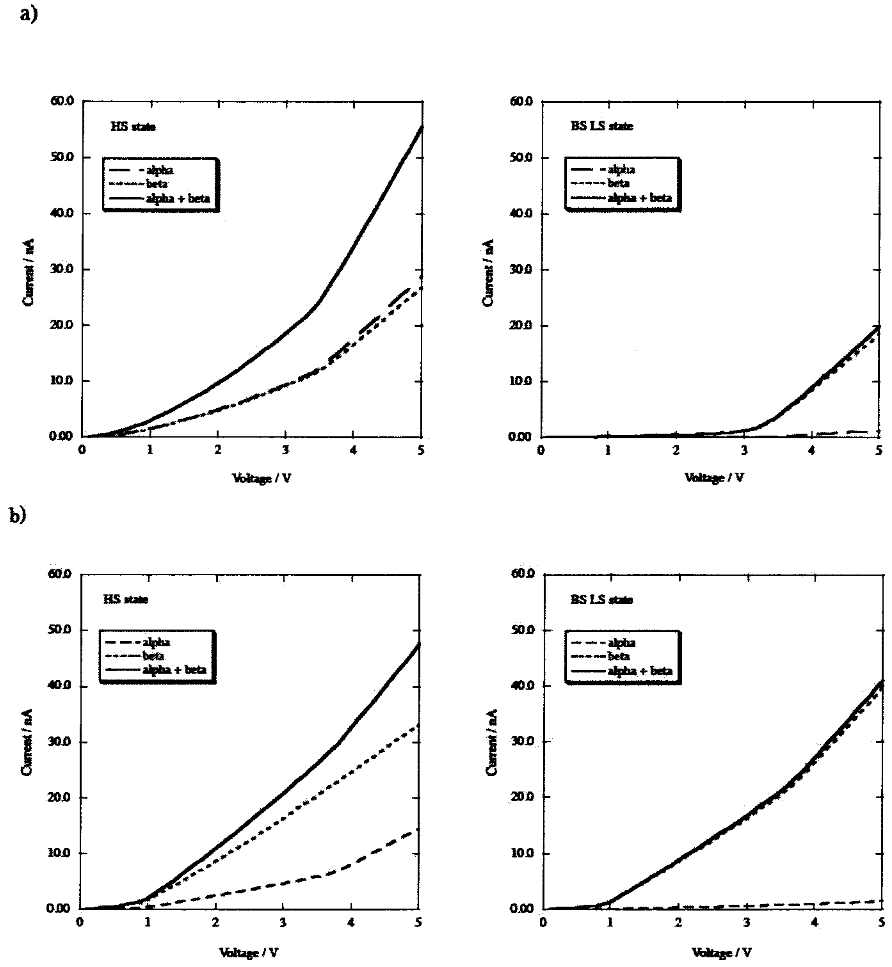

Figure 7.2: $I$-$V$ curves of a) $[\mathrm{H}\text{-}\mathrm{Cu}^{2+}\text{-}\mathrm{H}]_2$ and b) $[\mathrm{S}\text{-}\mathrm{Cu}^{2+}\text{-}\mathrm{S}]_2$ connected to the hollow site model on Au(111) surface in the HS and the BS LS states at 300 K temperature.

the Au-S moiety and the six-membered rings, and dominantly contributed to the electron conductivity. The LUMO locates on the one side of the Au-S moiety, whereas the LUMO+1 locates on the another side of the Au-S moiety. Therefore, if the LUMO is only treated to calculate the current, the current value becomes very small, and leading to mislead the result. The LUMO and the LUMO+1 are degenerate, so both LUMO and LUMO+1 are adopted for the calculation.

In the BS LS state, the current values at 1V are $i_\alpha = 4.82 \times 10^{-3}$ nA, $i_\beta = 0.117$ nA and $i_{\alpha+\beta} = 0.122$ nA, and is difference from the value of the HS state. The delocalization of molecular orbitals in the BS LS state is smaller than that of the HS state, so that the overlap elements become very small. The MO diagrams are showed in Figure 7.3a). The overlap elements, which are large values in the BS LS state, for example, are HOMO-5, but this element is small than the HS state. This reason is that the MO of the HOMO-5 localizes on the one side of the Au-S moiety, leading to be small overlap element.

Table 7.4: The orbital energies $E_\eta$ (in eV) and the overlap elements for [**H**-Cu$^{2+}$-**H**]$_2$ in HS and BS LS states. $\langle\text{Site}\rangle = \left|\langle 1|\phi_\sigma^\eta\rangle\right|^2 \left|\langle\phi_\sigma^\eta|N\rangle\right|^2$.

| | HS state | | | | | BS LS state | | | |
|---|---|---|---|---|---|---|---|---|---|
| | $\alpha$ orbital | | $\beta$ orbital | | | $\alpha$ orbital | | $\beta$ orbital | |
| | $E_\eta$ | ⟨Site⟩ | $E_\eta$ | ⟨Site⟩ | | $E_\eta$ | ⟨Site⟩ | $E_\eta$ | ⟨Site⟩ |
| HOMO-9 | -6.898 | 0.761 | -6.873 | 0.063 | HOMO-9 | -6.900 | 0.002 | -6.896 | 0.005 |
| HOMO-8 | -6.886 | 0.025 | -6.868 | 0.165 | HOMO-8 | -6.865 | 0.000 | -6.866 | 0.005 |
| HOMO-7 | -6.505 | 0.284 | -6.859 | 0.066 | HOMO-7 | -6.850 | 0.000 | -6.857 | 0.004 |
| HOMO-6 | -6.497 | 0.290 | -6.843 | 0.004 | HOMO-6 | -6.504 | 0.013 | -6.500 | 0.026 |
| HOMO-5 | -6.420 | 0.000 | -6.476 | 0.562 | HOMO-5 | -6.470 | 0.016 | -6.475 | 0.031 |
| HOMO-4 | -6.409 | 0.000 | -6.471 | 0.594 | HOMO-4 | -6.420 | 0.000 | -6.412 | 0.000 |
| HOMO-3 | -5.475 | 0.002 | -5.419 | 0.001 | HOMO-3 | -5.455 | 0.001 | -5.452 | 0.001 |
| HOMO-2 | -5.338 | 0.000 | -5.279 | 0.000 | HOMO-2 | -5.303 | 0.000 | -5.307 | 0.000 |
| HOMO-1 | -5.060 | 0.004 | -4.964 | 0.003 | HOMO-1 | -5.046 | 0.001 | -5.039 | 0.001 |
| HOMO | -5.007 | 0.002 | -4.916 | 0.001 | HOMO | -4.930 | 0.000 | -4.936 | 0.000 |
| LUMO | -3.992 | 0.000 | -4.000 | 0.000 | LUMO | -3.999 | 0.000 | -3.990 | 0.000 |
| LUMO+1 | -3.979 | 0.000 | -3.989 | 0.000 | LUMO+1 | -3.980 | 0.000 | -3.989 | 0.000 |
| LUMO+2 | -3.759 | 0.000 | -3.781 | 0.000 | LUMO+2 | -3.775 | 0.000 | -3.782 | 0.000 |
| LUMO+3 | -3.758 | 0.000 | -3.774 | 0.000 | LUMO+3 | -3.760 | 0.000 | -3.753 | 0.000 |
| LUMO+4 | -1.297 | 0.000 | -2.399 | 0.000 | LUMO+4 | -2.391 | 0.000 | -2.399 | 0.000 |
| LUMO+5 | -1.284 | 0.000 | -2.389 | 0.000 | LUMO+5 | -1.306 | 0.000 | -1.296 | 0.010 |
| LUMO+6 | -0.999 | 0.005 | -1.305 | 0.000 | LUMO+6 | -1.285 | 0.000 | -1.294 | 0.009 |
| LUMO+7 | -0.967 | 0.006 | -1.295 | 0.000 | LUMO+7 | -0.990 | 0.005 | -0.994 | 0.003 |
| LUMO+8 | -0.898 | 0.000 | -0.976 | 0.005 | LUMO+8 | -0.954 | 0.005 | -0.948 | 0.003 |
| LUMO+9 | -0.835 | 0.000 | -0.938 | 0.006 | LUMO+9 | -0.892 | 0.000 | -0.894 | 0.000 |

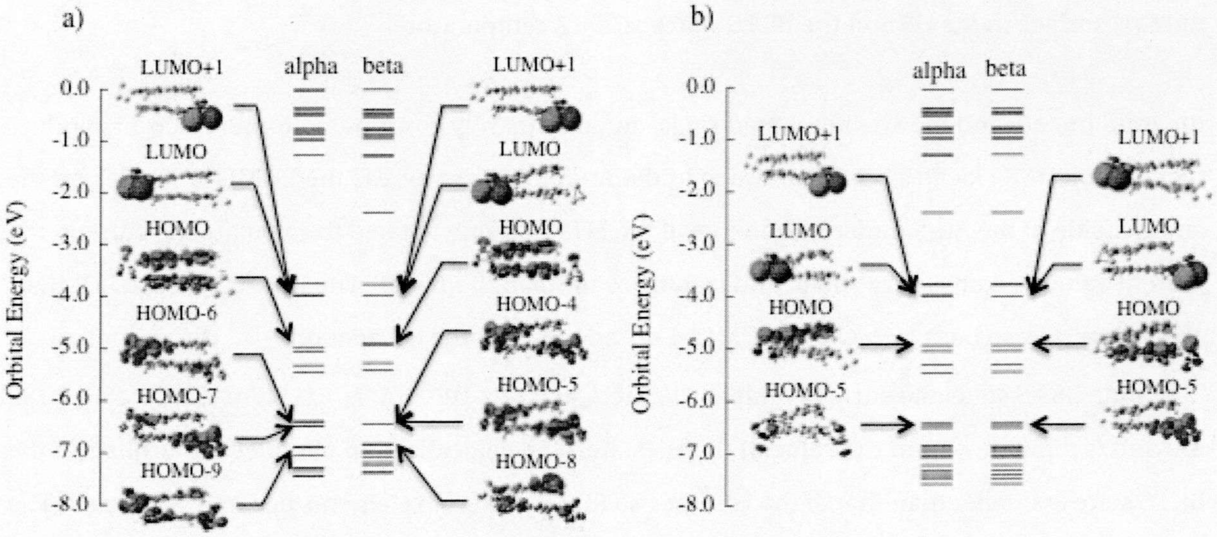

Figure 7.3: The MO diagrams of a) HS state and b) BS LS state for [**H**-Cu$^{2+}$-**H**]$_2$.

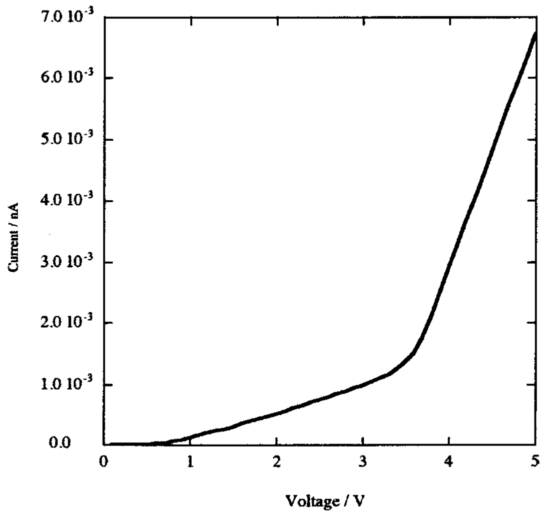

Figure 7.4: *I*-*V* curves of [**H**-$Cu^{2+}$-**H**]$_2$ connected to the hollow site model on Au(111) surface in low-spin states (closed shell) at 300 K temperature.

It indicates that the contribution to the orbital is small. However, as shown in Table 7.4, I found that $\gamma_\beta$ value was much larger than $\gamma_\alpha$ value. This behavior of the BS LS state, which is different from the HS state, is due to the fact that the $\beta$-LUMO of the extended molecule spatially extends on the molecule than that of $\alpha$ orbital in the BS LS state.

In order to discuss the difference between the *I*-*V* characteristics in the BS LS and the closed-shell LS state, I calculated the *I*-*V* characteristics of the [**H**-$Cu^{2+}$-**H**]$_2$ using a restricted B3LYP (RB3LYP). I adopted the orbitlas from LUMO to LUMO+2 and calculated the coupling constants. The difference of the total energies between the BS LS and the closed-shell LS is 43.2 kcal/mol and the BS LS is more stable than the closed-shell LS. The obtained current ($i = 1.18 \times 10^{-4}$ nA at 1V) is much smaller than that of the BS LS state as shown in Figure 7.4. In the closed-shell calculation, the almost all of the overlap elements are very small, indicating that the orbital delocalization of the molecule on the S atoms is smaller than that of the BS LS state. The HOMO orbital of the closed-shell LS is localized at Cu ions, whereas the HOMO of the BS LS state is delocalized on the whole molecule. In this way, the results in the BS LS and the closed-shell LS states are different, suggesting a necessity of calculations of the *I*-*V* characteristic based on the method with a static correlation such as BS method.

### The Salen Type DNA

Next I show the results of *I*-*V* characteristics of the [**S**-$Cu^{2+}$-**S**]$_2$ model. In the HS state, the calculated current values for $\alpha$ and $\beta$ orbitals at 1V are $i_\alpha = 0.304$ nA, $i_\beta = 1.51$ nA and $i_{\alpha+\beta} = 1.81$ nA. I found that the $\gamma_\alpha$ value and the overlap element of $\alpha$ orbital are different from those of $\beta$ orbital. The

Table 7.5: The orbital energies $E_\eta$ (in eV) and the overlap elements for the $[\mathbf{S}\text{-Cu}^{2+}\text{-}\mathbf{S}]_2$ in HS and BS LS states. $\langle\text{Site}\rangle = \left|\langle 1|\phi_\sigma^\eta\rangle\right|^2 \left|\langle\phi_\sigma^\eta|N\rangle\right|^2$.

| | HS state | | | | | BS LS state | | | |
|---|---|---|---|---|---|---|---|---|---|
| | $\alpha$ orbital | | $\beta$ orbital | | | $\alpha$ orbital | | $\beta$ orbital | |
| | $E_\eta$ | ⟨Site⟩ | $E_\eta$ | ⟨Site⟩ | | $E_\eta$ | ⟨Site⟩ | $E_\eta$ | ⟨Site⟩ |
| HOMO-9 | -6.319 | 0.001 | -6.324 | 0.000 | HOMO-9 | -6.324 | 0.000 | -6.319 | 0.002 |
| HOMO-8 | -6.303 | 0.000 | -6.308 | 0.006 | HOMO-8 | -6.303 | 0.001 | -6.308 | 0.003 |
| HOMO-7 | -6.157 | 0.001 | -6.285 | 0.065 | HOMO-7 | -6.285 | 0.000 | -6.263 | 0.001 |
| HOMO-6 | -6.005 | 0.000 | -6.264 | 0.040 | HOMO-6 | -6.004 | 0.000 | -6.157 | 0.000 |
| HOMO-5 | -5.993 | 0.001 | -5.960 | 0.002 | HOMO-5 | -5.963 | 0.002 | -5.992 | 0.000 |
| HOMO-4 | -5.785 | 0.049 | -5.768 | 0.021 | HOMO-4 | -5.771 | 0.079 | -5.783 | 0.020 |
| HOMO-3 | -5.746 | 0.116 | -5.721 | 0.073 | HOMO-3 | -5.743 | 0.179 | -5.723 | 0.077 |
| HOMO-2 | -5.718 | 0.004 | -5.691 | 0.007 | HOMO-2 | -5.713 | 0.008 | -5.698 | 0.009 |
| HOMO-1 | -5.554 | 0.000 | -5.498 | 0.000 | HOMO-1 | -5.505 | 0.000 | -5.549 | 0.000 |
| HOMO | -5.416 | 0.000 | -5.354 | 0.000 | HOMO | -5.412 | 0.000 | -5.355 | 0.000 |
| LUMO | -3.547 | 0.000 | -3.545 | 0.000 | LUMO | -3.545 | 0.000 | -3.547 | 0.000 |
| LUMO+1 | -3.525 | 0.000 | -3.522 | 0.000 | LUMO+1 | -3.524 | 0.000 | -3.522 | 0.000 |
| LUMO+2 | -3.519 | 0.001 | -3.520 | 0.000 | LUMO+2 | -3.520 | 0.000 | -3.519 | 0.001 |
| LUMO+3 | -3.509 | 0.001 | -3.510 | 0.000 | LUMO+3 | -3.509 | 0.000 | -3.510 | 0.001 |
| LUMO+4 | -2.230 | 0.000 | -2.750 | 0.000 | LUMO+4 | -2.750 | 0.000 | -2.513 | 0.000 |
| LUMO+5 | -1.835 | 0.000 | -2.512 | 0.000 | LUMO+5 | -2.198 | 0.000 | -2.229 | 0.000 |
| LUMO+6 | -1.601 | 0.000 | -2.196 | 0.000 | LUMO+6 | -1.832 | 0.000 | -1.803 | 0.000 |
| LUMO+7 | -1.466 | 0.000 | -1.800 | 0.000 | LUMO+7 | -1.572 | 0.000 | -1.600 | 0.000 |
| LUMO+8 | -0.783 | 0.003 | -1.571 | 0.000 | LUMO+8 | -1.466 | 0.000 | -1.437 | 0.000 |
| LUMO+9 | -0.705 | 0.004 | -1.436 | 0.000 | LUMO+9 | -0.783 | 0.003 | -0.783 | 0.003 |

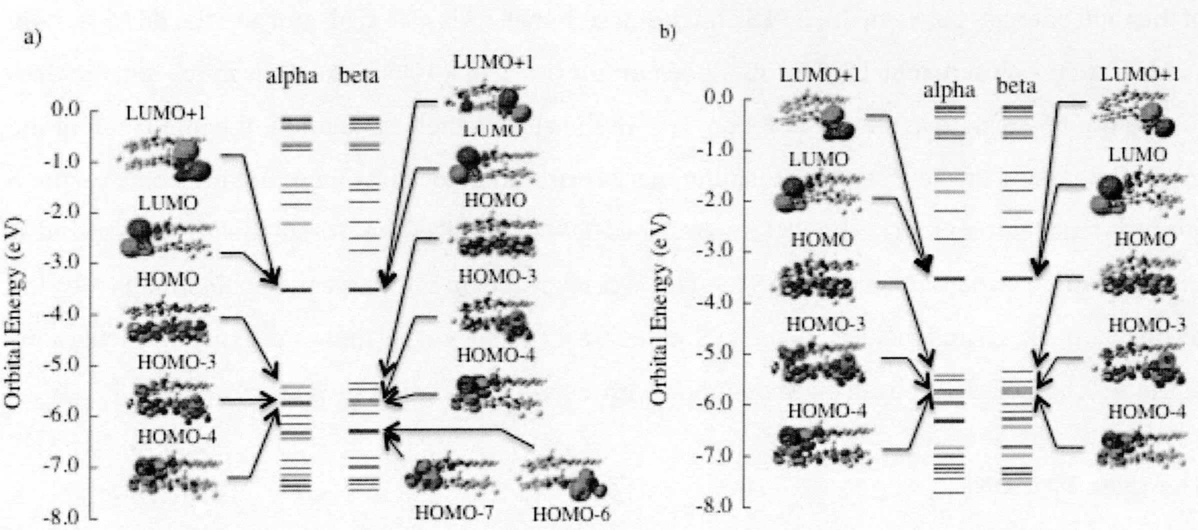

Figure 7.5: The MO diagrams of a) HS state and b) BS LS state for $[\mathbf{S}\text{-Cu}^{2+}\text{-}\mathbf{S}]_2$.

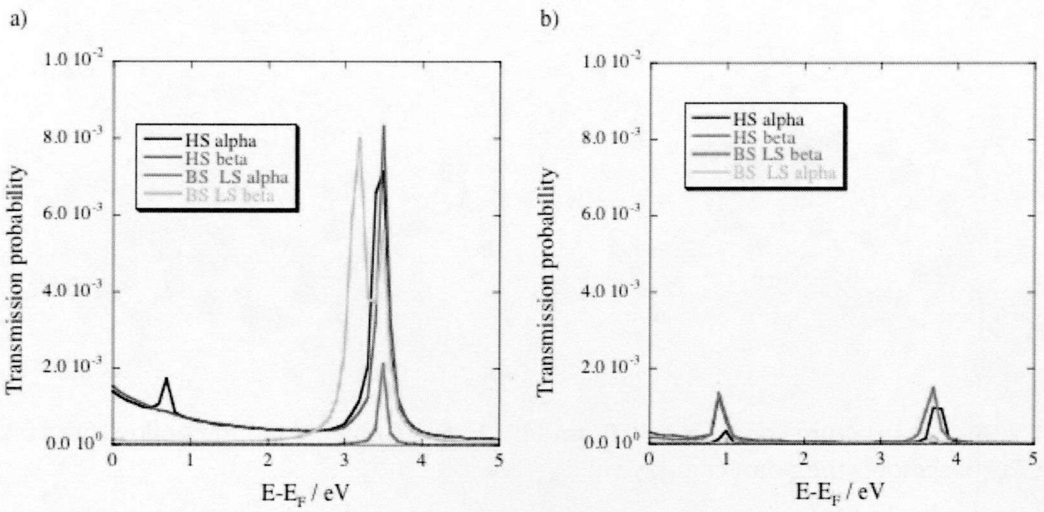

Figure 7.6: Transition probability of a) [**H**-Cu$^{2+}$-**H**]$_2$ and b) [**S**-Cu$^{2+}$-**S**]$_2$ connected to the hollow site model on Au(111) surface in the HS and the BS LS states.

dominant overlap elements are HOMO-4 and HOMO-3 for $\alpha$ orbitals, and HOMO-7, -6 -4 and -3 for $\beta$ orbitals. These orbitals are depicted in Figure 7.5a). The orbital of the HOMO-3 extends to the Au-S moiety and six-membered rings, leading to large overlap element. In case of the HOMO-4, the orbital locates on one side of the Au-S moiety, leading to smaller overlap element than the HOMO-3. On the other hand, the current values at 1V in the BS LS state are $i_\alpha$ = 0.0356 nA, $i_\beta$ = 1.20 nA and $i_{\alpha+\beta}$ = 1.22 nA. And the orbitals contributed to the electrical conduction are HOMO-4 and HOMO-3 for both $\alpha$ and $\beta$ orbitals. There orbitals are depicted in Figure 7.5b). Similarly to the HS state, the HOMO-3 mainly contributes to the electron conductivity in the BS LS state.

These results explained above indicate that the current of [**H**-Cu$^{2+}$-**H**]$_2$ tends to become larger than that of [**S**-Cu$^{2+}$-**S**]$_2$ in the HS states. This is because that the magnitude of coupling constants between the isolated molecule and the reservoirs, and the delocalization of orbitals are different in these two systems. The magnitude of the coupling constants of [**H**-Cu$^{2+}$-**H**]$_2$ is larger than that of [**S**-Cu$^{2+}$-**S**]$_2$, indicating that the interaction between the electrode orbitals and the LUMO of the molecule is stronger. It also indicates that the delocalization of the molecular orbital in [**H**-Cu$^{2+}$-**H**]$_2$ is larger than that of [**S**-Cu$^{2+}$-**S**]$_2$. It seems that this originates in the particular structure of [**S**-Cu$^{2+}$-**S**] type DNA. The dihedral angle between the planes defined by the aromatic rings was 22° in [**S**-Cu$^{2+}$-**S**] because of a crosslink by ethylenediamine in the metal-salen complex [111], so that the overlap of the $\pi$-orbital between the adjacent base pairs becomes small and the current becomes lower.

However, in the BS LS state, the current of [**S**-Cu$^{2+}$-**S**]$_2$ becomes larger than that of [**H**-Cu$^{2+}$-**H**]$_2$. The transmission probability of the [**H**-Cu$^{2+}$-**H**]$_2$ is smaller than that of the [**S**-Cu$^{2+}$-**S**]$_2$ (Figure

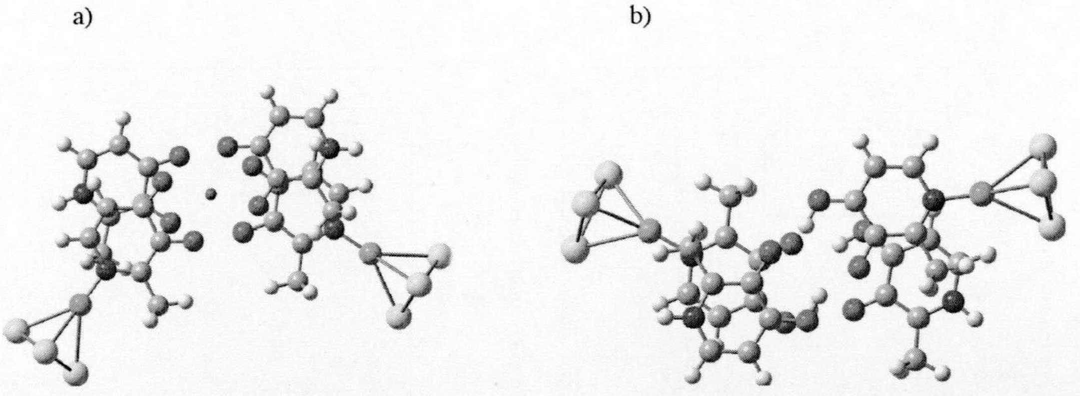

Figure 7.7: Model structures of a) [**H**-pc-**H**]$_2$ and b) [**H**-**H**]$_2$ connected to the hollow site of Au(111) surface. Purple color is the point charge in a).

7.6), so that the current values of the [**S**-Cu$^{2+}$-**S**]$_2$ becomes larger than that of the [**H**-Cu$^{2+}$-**H**]$_2$. The transmission probability of the [**H**-Cu$^{2+}$-**H**]$_2$ are almost zero up to $E - E_f = 3$ (eV) in [**H**-Cu$^{2+}$-**H**]$_2$ in the BS LS state, indicating that the current flows at high applied voltages. In the BS LS state of the [**H**-Cu$^{2+}$-**H**]$_2$, the difference between the Fermi energy and the orbitals contributed the transmission are large, while in [**S**-Cu$^{2+}$-**S**]$_2$ the differences are small. Therefore, the onset of the [**H**-Cu$^{2+}$-**H**]$_2$ need high voltage.

In [**S**-Cu$^{2+}$-**S**]$_2$ , the difference of the current values between the HS and the BS LS states is smaller than that of [**H**-Cu$^{2+}$-**H**]$_2$ . From the distorted structure of [**S**-Cu$^{2+}$-**S**]$_2$ , it is considered that the interaction of orbitals between adjacent base pairs is very small. Therefore, the difference in current values between the HS and the BS LS state becomes small.

Finally, in the both systems, the current of the HS state is larger than the BS LS state. It indicates that the interaction between the occupied electrode orbitals and LUMO of the molecule is strong in the HS state. From Eq. (4.14), a coupling constant depends on the $d$ value, which is the existence probability of sulfur atomic orbitals in LUMO. In the HS state, the electron densities tend to localize around the sulfur atoms because of the spin polarization. These phenomena bring a higher current value to the HS state.

### 7.3.3 Effects of Metal Ions

In order to understand the effect of Cu ions, I next examined the $I$-$V$ characteristics without metal ions for [**H**-Cu$^{2+}$-**H**]$_2$. I investigated the two models without metal ions here. One is the model that Cu ions are replaced by the point charge (+2) ([**H**-pc-**H**]$_2$), and another is the hydrogen bond model ([**H**-**H**]$_2$). These systems are connected to the hollow site on Au(111) surface, as shown in Figure

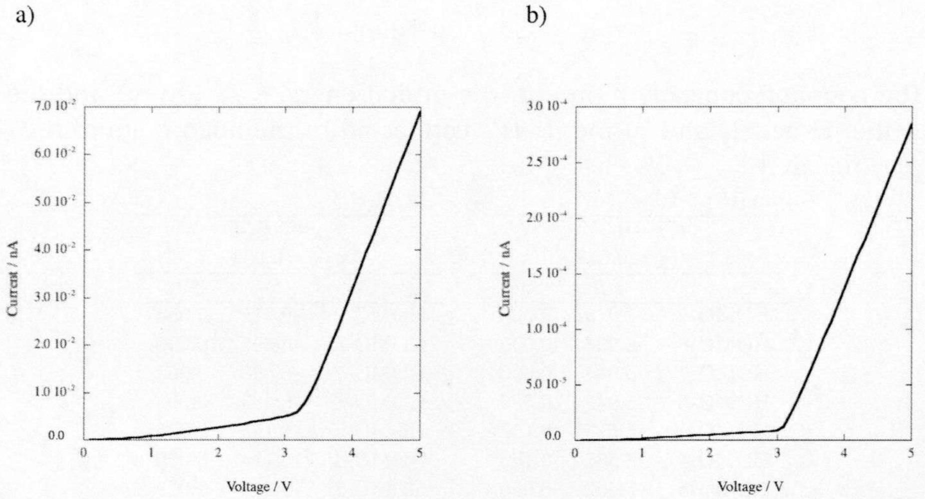

Figure 7.8: *I*-*V* curves of a) [**H**-pc-**H**]$_2$ and b) [**H**-**H**]$_2$ connected to the hollow site of Au(111) surface at 300 K temperature.

7.7. In [**H**-pc-**H**]$_2$ model, a geometry of all atoms is same as that of the [**H**-Cu$^{2+}$-**H**]$_2$ model except for the Cu ion. In [**H**-**H**]$_2$ model, I referred to structure suggested in ref. [89] and performed full optimization for this monomer structure. I used RB3LYP because there are no spin sources in the systems and they can be described by the closed-shell calculation. The distance between adjacent base pairs is assumed to be 3.7 Å. I adopted the orbitals from LUMO to LUMO+1 and calculated the coupling constants. The calculated results of the *I*-*V* characteristics, and $\gamma$ values, the orbital energies and the overlap elements are summarized in Figure 7.8 and Table 7.6, respectively.

The magnitudes of the current in the both models are much smaller than the original method contained, indicaing the coupling constant and the overlap elements are much smaller. By comparing [**H**-pc-**H**]$_2$ with [**H**-**H**]$_2$ model, the current of [**H**-pc-**H**]$_2$ model is larger than that of [**H**-**H**]$_2$ model. The dominant overlap elements of [**H**-pc-**H**]$_2$ are HOMO-4 and HOMO-5, whereas almost all of overlap elements of [**H**-**H**]$_2$ are zero. These orbitals were shown in Figure 7.9. In the case of [**H**-**H**] model, the delocalization of the molecular orbital is small, therefore the conductivity is decrease. But the point charge changes the delocalization of $\pi$ orbitals, so that the conductivity is increased. In this way, an introduction of Cu$^{2+}$ ions significantly contributes to the increase of the current value.

Table 7.6: The coupling constant $\gamma$ (in eV), the orbital energies $E_\eta$ (in eV) and the overlap elements of a) the [**H**-pc-**H**]$_2$ and b) the [**H**-**H**]$_2$ connected to the hollow site of Au(111) surface. $\langle\text{Site}\rangle = \left|\langle 1|\phi^{\eta}_{\sigma}\rangle\right|^2 \left|\langle\phi^{\eta}_{\sigma}|N\rangle\right|^2$.

a) [**H**-pc-**H**]$_2$

$\gamma_{1R} = 0.040$
$\gamma_{LN} = 0.049$

| | $E_\eta$ | ⟨Site⟩ |
|---|---|---|
| HOMO-9 | -7.019 | 0.000 |
| HOMO-8 | -6.996 | 0.000 |
| HOMO-7 | -6.944 | 0.000 |
| HOMO-6 | -6.943 | 0.000 |
| HOMO-5 | -6.575 | 0.152 |
| HOMO-4 | -6.566 | 0.160 |
| HOMO-3 | -5.492 | 0.000 |
| HOMO-2 | -5.409 | 0.000 |
| HOMO-1 | -5.125 | 0.001 |
| HOMO | -5.103 | 0.001 |
| LUMO | -4.059 | 0.000 |
| LUMO+1 | -4.048 | 0.000 |
| LUMO+2 | -3.836 | 0.000 |
| LUMO+3 | -3.829 | 0.000 |
| LUMO+4 | -3.036 | 0.000 |
| LUMO+5 | -2.380 | 0.000 |
| LUMO+6 | -1.354 | 0.004 |
| LUMO+7 | -1.343 | 0.004 |
| LUMO+8 | -1.062 | 0.000 |
| LUMO+9 | -1.013 | 0.001 |

b) [**H**-**H**]$_2$

$\gamma_{1R} = 0.049$
$\gamma_{LN} = 0.005$

| | $E_\eta$ | ⟨Site⟩ |
|---|---|---|
| HOMO-9 | -6.719 | 0.004 |
| HOMO-8 | -6.690 | 0.006 |
| HOMO-7 | -6.496 | 0.002 |
| HOMO-6 | -6.463 | 0.003 |
| HOMO-5 | -6.136 | 0.000 |
| HOMO-4 | -6.114 | 0.000 |
| HOMO-3 | -5.217 | 0.000 |
| HOMO-2 | -5.148 | 0.000 |
| HOMO-1 | -4.830 | 0.000 |
| HOMO | -4.806 | 0.000 |
| LUMO | -4.068 | 0.000 |
| LUMO+1 | -4.005 | 0.000 |
| LUMO+2 | -3.813 | 0.000 |
| LUMO+3 | -3.786 | 0.000 |
| LUMO+4 | -1.344 | 0.000 |
| LUMO+5 | -1.338 | 0.000 |
| LUMO+6 | -0.988 | 0.000 |
| LUMO+7 | -0.959 | 0.000 |
| LUMO+8 | -0.921 | 0.000 |
| LUMO+9 | -0.860 | 0.000 |

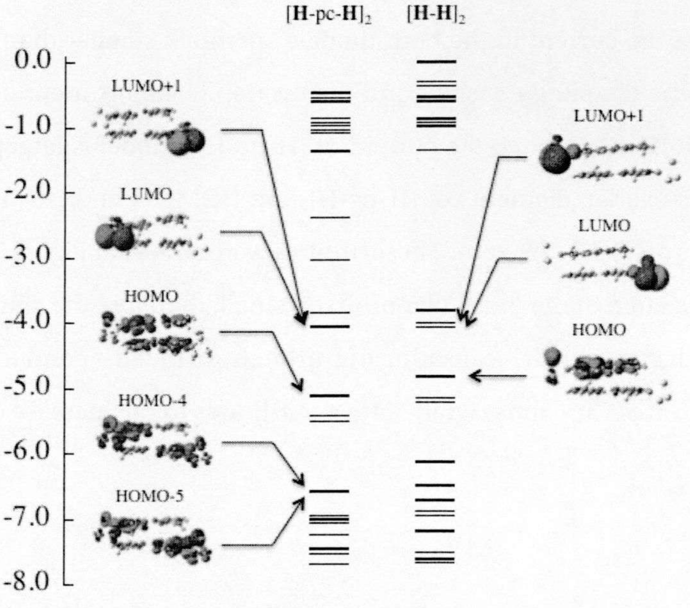

Figure 7.9: The MO diagrams of [**H**-pc-**H**]$_2$ and [**H**-**H**]$_2$.

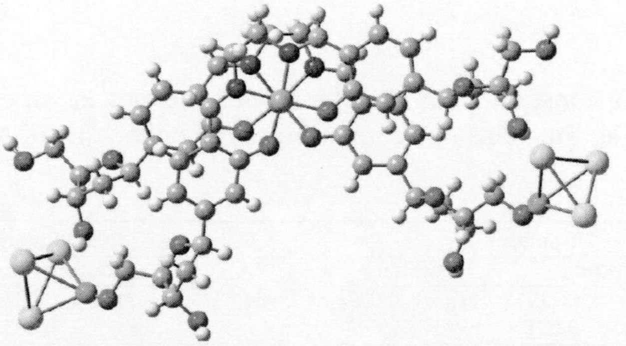

Figure 7.10: Model structure of $[\mathbf{S}\text{-Cu}^{2+}\text{-}\mathbf{S}]_2$ with the backbone connected to the hollow site of Au(111) surface.

### 7.3.4 *I-V* Characteristics of $[\mathbf{S}\text{-Cu}^{2+}\text{-}\mathbf{S}]_2$ with the Backbone

Here, I examine the effect of the backbone on the *I-V* characteristics. It has been reported that the electron conductivity between the backbone and reservoirs in natural DNA is small [18]. In order to consider the effect in artificial M-DNA, I incorporate the modeled backbone into my calculation based on the $[\mathbf{S}\text{-Cu}^{2+}\text{-}\mathbf{S}]_2$ structure as shown in Figure 7.10. As *backbone* model, I use the X-ray geometry of the metal-salen base pair complex [111] The calculated results of the *I-V* characteristics are shown in Figure 7.11 and $\gamma$ values, the orbital energies and the overlap elements are summarized in Table 7.7.

From the calculated results, I find that the magnitudes of the currents of the backbone model for the HS and the BS LS state are very small in comparison with the *without-backbone* ($[\mathbf{S}\text{-Cu}^{2+}\text{-}\mathbf{S}]_2$) model, indicating that the backbone cuts off the conductivity. This significant decrease of the current is simply explained by that $\pi$-orbitals do not delocalize to the backbone where the electrodes are connected. This behavior is agreed with the calculated result of the electron conductivity of the natural B-DNA reported by Tada et al. [18] These results indicate that the *without-backbone* model for the artificial M-DNAs can transmit electricity, although a realistic model with backbone seems to be hard to conduct the electrons.

Table 7.7: The coupling constant $\gamma$ (in eV), the orbital energies $E_\eta$ (in eV) and the overlap elements of [**S**-Cu$^{2+}$-**S**]$_2$ with the backbone connected to the hollow site of Au(111) surface. $\langle\text{Site}\rangle = \left|\langle 1|\phi_\sigma^\eta\rangle\right|^2 \left|\langle\phi_\sigma^\eta|N\rangle\right|^2$

| | HS state | | | | | BS LS state | | | |
|---|---|---|---|---|---|---|---|---|---|
| | $\alpha$ orbital | | $\beta$ orbital | | | $\alpha$ orbital | | $\beta$ orbital | |
| | $\gamma_{1R}$ | 0.115 | $\gamma_{1R}$ | 0.007 | | $\gamma_{1R}$ | 0.004 | $\gamma_{1R}$ | 0.115 |
| | $\gamma_{LN}$ | 0.011 | $\gamma_{LN}$ | 0.009 | | $\gamma_{LN}$ | 0.005 | $\gamma_{LN}$ | 0.009 |
| | $E_\eta$ | ⟨Site⟩ | $E_\eta$ | ⟨Site⟩ | | $E_\eta$ | ⟨Site⟩ | $E_\eta$ | ⟨Site⟩ |
| HOMO-9 | -5.869 | 0.000 | -5.869 | 0.000 | HOMO-9 | -5.869 | 0.000 | -5.869 | 0.000 |
| HOMO-8 | -5.847 | 0.000 | -5.819 | 0.000 | HOMO-8 | -5.835 | 0.000 | -5.833 | 0.000 |
| HOMO-7 | -5.687 | 0.000 | -5.620 | 0.000 | HOMO-7 | -5.631 | 0.000 | -5.680 | 0.000 |
| HOMO-6 | -5.557 | 0.000 | -5.488 | 0.000 | HOMO-6 | -5.548 | 0.000 | -5.488 | 0.000 |
| HOMO-5 | -5.488 | 0.000 | -5.484 | 0.000 | HOMO-5 | -5.488 | 0.000 | -5.486 | 0.000 |
| HOMO-4 | -5.419 | 0.000 | -5.419 | 0.000 | HOMO-4 | -5.419 | 0.000 | -5.419 | 0.000 |
| HOMO-3 | -4.693 | 0.000 | -4.693 | 0.000 | HOMO-3 | -4.693 | 0.000 | -4.693 | 0.000 |
| HOMO-2 | -4.548 | 0.000 | -4.548 | 0.000 | HOMO-2 | -4.548 | 0.000 | -4.548 | 0.000 |
| HOMO-1 | -4.442 | 0.000 | -4.442 | 0.000 | HOMO-1 | -4.442 | 0.000 | -4.442 | 0.000 |
| HOMO | -3.686 | 0.000 | -3.686 | 0.000 | HOMO | -3.686 | 0.000 | -3.686 | 0.000 |
| LUMO | -2.255 | 0.000 | -2.484 | 0.000 | LUMO | -2.484 | 0.000 | -2.283 | 0.000 |
| LUMO+1 | -1.981 | 0.025 | -2.278 | 0.000 | LUMO+1 | -2.221 | 0.000 | -2.245 | 0.000 |
| LUMO+2 | -1.968 | 0.029 | -2.215 | 0.000 | LUMO+2 | -1.977 | 0.001 | -1.974 | 0.000 |
| LUMO+3 | -1.906 | 0.006 | -1.974 | 0.000 | LUMO+3 | -1.963 | 0.001 | -1.941 | 0.000 |
| LUMO+4 | -1.884 | 0.002 | -1.932 | 0.000 | LUMO+4 | -1.906 | 0.000 | -1.906 | 0.000 |
| LUMO+5 | -1.837 | 0.001 | -1.906 | 0.000 | LUMO+5 | -1.851 | 0.000 | -1.881 | 0.000 |
| LUMO+6 | -1.725 | 0.001 | -1.848 | 0.000 | LUMO+6 | -1.834 | 0.000 | -1.836 | 0.000 |
| LUMO+7 | -0.622 | 0.000 | -1.834 | 0.000 | LUMO+7 | -1.724 | 0.000 | -1.690 | 0.000 |
| LUMO+8 | -0.170 | 0.000 | -1.690 | 0.000 | LUMO+8 | -0.622 | 0.000 | -0.622 | 0.000 |
| LUMO+9 | 0.016 | 0.001 | -0.622 | 0.000 | LUMO+9 | -0.170 | 0.000 | -0.170 | 0.000 |

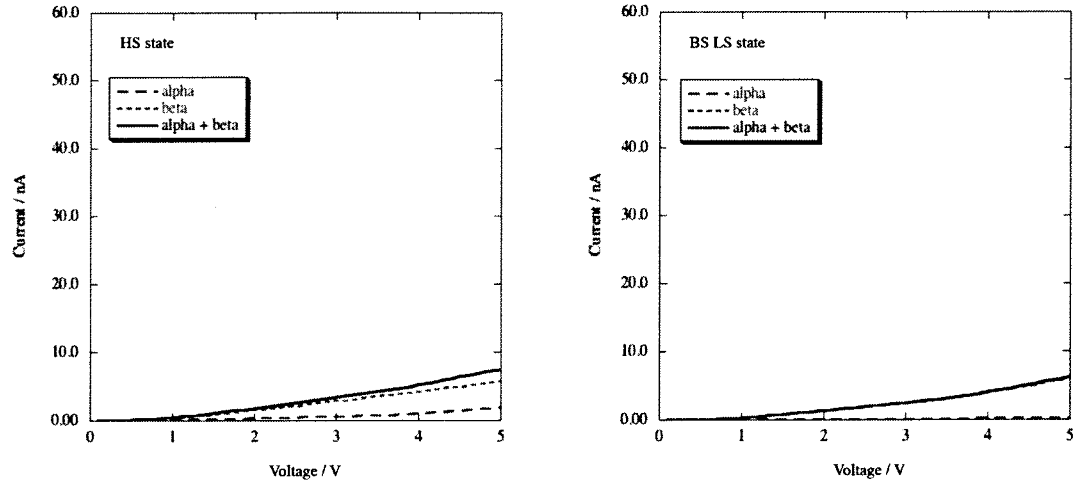

Figure 7.11: *I*-*V* curves of [**S**-Cu$^{2+}$-**S**]$_2$ with the backbone model connected to the hollow site of Au(111) surface in HS and BS LS states at 300 K temperature.

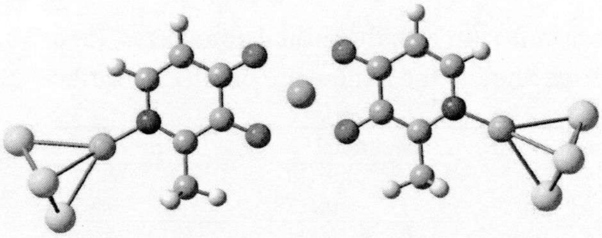

Figure 7.12: Model structure of [**H**-$Cu^{2+}$-**H**]$_2$ monomer connected to the hollow site of Au(111) surface.

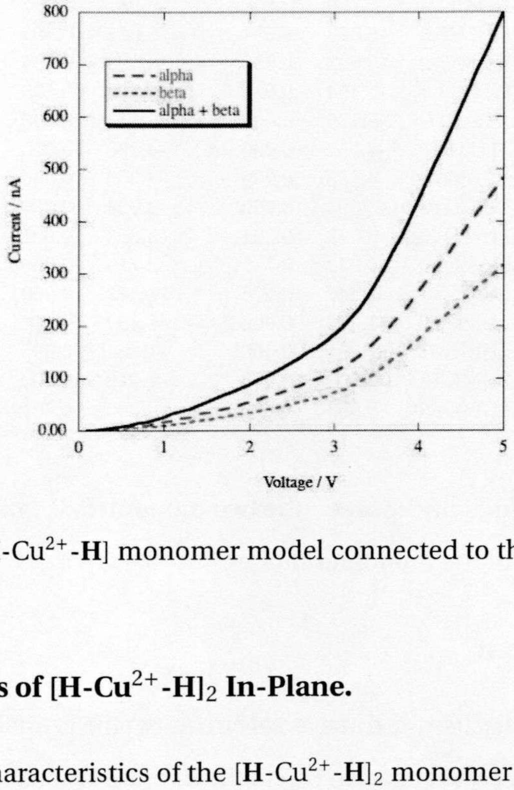

Figure 7.13: I-V curves of [**H**-$Cu^{2+}$-**H**] monomer model connected to the hollow site of Au(111) surface at 300 K temperature.

### 7.3.5 *I-V* Characteristics of [H-$Cu^{2+}$-H]$_2$ In-Plane.

I also investigated the *I-V* characteristics of the [**H**-$Cu^{2+}$-**H**]$_2$ monomer connected to the hollow site on Au(111) surface as shown in Figure 7.12. This calculation means the in-plane electron conductivity of the system. I adopted the orbitals from LUMO to LUMO+1 orbitals and calculated the coupling constants. The calculated results of the *I-V* characteristics are shown in Figure 7.13 and $\gamma$ values, the orbital energies and the overlap elements are summarized in Table 7.8.

From the calculated results, the magnitude of the in-plane current of the [**H**-$Cu^{2+}$-**H**] monomer is larger than the dimer model of [**H**-$Cu^{2+}$-**H**]$_2$. The reason for this high conductivity is explained as $d$-orbital of Cu ions assists the $\pi$-electrons to delocalize from one hydroxypyridone to the opposite one in the same plane. In other words, the mixture of $d$ and $\pi$ orbital causes the delocalization on the extended molecule in the plane, and then, electron conductivity becomes large. However, the Cu ion does not intermediate the delocalization between two monomers, because the distance (3.7Å) is

Table 7.8: The coupling constant $\gamma$ (in eV), the orbital energies $E_\eta$ (in eV) and the overlap elements of [H-Cu$^{2+}$-H] monomer connected to the hollow site of Au(111) surface. $\langle \text{Site} \rangle = |\langle 1|\phi_\sigma^\eta\rangle|^2 |\langle \phi_\sigma^\eta|N\rangle|^2$

| | $\alpha$ orbital | | $\beta$ orbital | |
|---|---|---|---|---|
| | $\gamma_{1R}$ | 0.418 | $\gamma_{1R}$ | 0.372 |
| | $\gamma_{LN}$ | 0.417 | $\gamma_{LN}$ | 0.371 |
| | $E_\eta$ | ⟨Site⟩ | $E_\eta$ | ⟨Site⟩ |
| HOMO-9 | -7.539 | 0.040 | -7.431 | 0.007 |
| HOMO-8 | -7.213 | 0.036 | -7.371 | 0.001 |
| HOMO-7 | -7.184 | 0.048 | -7.159 | 0.010 |
| HOMO-6 | -7.012 | 0.369 | -7.136 | 0.073 |
| HOMO-5 | -7.010 | 0.335 | -7.002 | 0.145 |
| HOMO-4 | -6.700 | 0.000 | -6.987 | 0.257 |
| HOMO-3 | -6.623 | 0.591 | -6.606 | 0.385 |
| HOMO-2 | -6.622 | 0.690 | -6.599 | 0.654 |
| HOMO-1 | -5.454 | 0.013 | -5.403 | 0.109 |
| HOMO | -5.185 | 0.005 | -5.113 | 0.008 |
| LUMO | -4.087 | 0.000 | -4.090 | 0.000 |
| LUMO+1 | -4.085 | 0.000 | -4.089 | 0.000 |
| LUMO+2 | -3.894 | 0.000 | -3.904 | 0.000 |
| LUMO+3 | -3.863 | 0.001 | -3.863 | 0.001 |
| LUMO+4 | -1.349 | 0.075 | -2.719 | 0.000 |
| LUMO+5 | -1.347 | 0.074 | -1.353 | 0.000 |
| LUMO+6 | -1.080 | 0.000 | -1.350 | 0.074 |
| LUMO+7 | -1.034 | 0.000 | -1.064 | 0.095 |
| LUMO+8 | -0.859 | 0.009 | -1.016 | 0.000 |
| LUMO+9 | -0.853 | 0.010 | -0.860 | 0.001 |

too long. Therefore, the conductivity between the two monomers is quite small in comparison with that of in-plane conductivity of the monomer model.

### 7.3.6 Longitudinal Current

In the previous subsection, I discuss the transversal current of the artificial M-DNA. The DNA has the backbones, so that the current vales tend to be small. In this subsection, I discuss the longitudinal current of the dimer and the trimer models of the artificial M-DNA (Figure 7.14) in the HS and BS states.

In order to estimate the current values, I assumed that the electrodes were connected to the aromatic rings of the one-side ligand, and that the distance between the electrode and the aromatic rings were 3.4 Å.

In previous calculation, the end-site, which is connected to the electrodes, is one site. However, in this model, the end-site is more than one site. Therefore, I extended the theory to the systems containing many end-sites as the following,

$$\langle 1|\eta\rangle = \frac{\sum_i \langle i|\eta\rangle}{\sum_i i}, \tag{7.3}$$

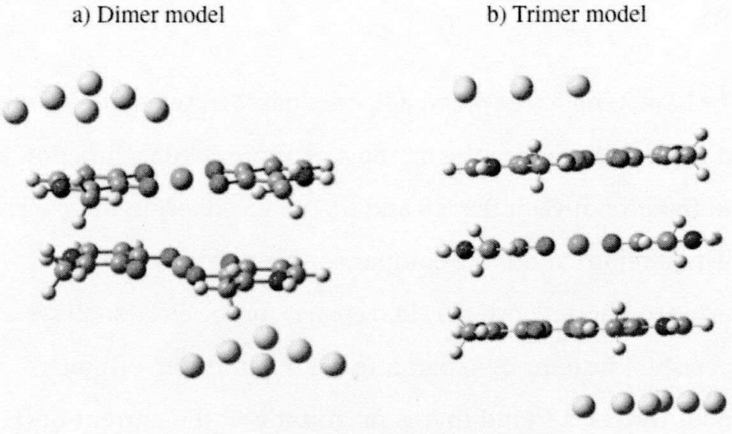

Figure 7.14: The calculated a) dimer and b) trimer models of the artificial M-DNA.

Table 7.9: The longitudinal current values (in nA) of the dimer and the trimer models in the HS and BS LS states.

| | HS state | BS LS state |
|---|---|---|
| Dimer | 1.09 | 0.504 |
| Timer | 0.378 | 0.276 |

where $i$ means the site connected to the electrodes.

I summarized the current values at 1V of the dimer and the trimer models in the HS and BS LS states in Table 7.9. In both the dimer and the trimer models, the current values of the HS states were larger than that of the BS LS states. In the dimer model, there were almost no large difference between the transversal and the longitudinal current values. It indicates that the subsisting current values in the HS state of the [**H**-Cu$^{2+}$-**H**]$_2$ are 1 ~ 3 nA, in the BS LS states 0.1 ~ 0.5 nA. On the dependence on the length of the artificial M-DNA, the current values of the dimer models were large than that of the trimer models, indicating there is the dependence on the length.

## 7.4 Conclusion

I investigated the *I*-*V* characteristics between adjacent bases in two types of the artificial M-DNAs, i.e. [**H**-Cu$^{2+}$-**H**]$_2$ and [**S**-Cu$^{2+}$-**S**]$_2$, using the elastic scattering Green's function with the DFT. Especially I focus on the different between the HS and the BS LS states on the *I*-*V* characteristic. To my knowledge, this is the first report about the comparison between them.

The elastic scattering method reported by Luo et al. is for the close shell system. So, in this study, I extended for the open shell systems by separating the $\alpha$ and $\beta$ spin orbitals.

From my calculated results, I found that i) magnitude of the current of [**H**-Cu$^{2+}$-**H**]$_2$ tends to become larger than that of [**S**-Cu$^{2+}$-**S**]$_2$, ii) the *I*-*V* characteristics is changed by the spin states and iii) introduction of metal ions into DNA remarkably increases the intra-plane electrical transport by increasing the delocalization of $\pi$-orbitals. These results suggest the possibility of the control of the *I*-*V* characteristics in the artificial M-DNAs. The simple breakthrough for obtaining the larger electron conductivity of the artificial M-DNA from a theoretical aspect is to change the metal ion with a large radius, because the interaction between adjacent planes becomes larger.

In addition, the results also suggest that the system can be applied to the spintoronics materials. Previously, my group reported the possibility of the system for the molecular switching devices by an external magnetic field [113]. From both results, it seems that I can control the conductivity by changing the spin state with the external magnetic field.

Based on my approach, I compared the current of the HS state with that of the BS LS state. The results strongly indicated that the coupling constant based on the elastic scattering method drastically changed the current value.

# Part V

# Magnetism

# Chapter 8

# Artificial Metal-DNA

## 8.1 Introduction

DNA is well known as the molecule containing all genetic information which is necessary for all living organisms in the earth. DNA consists of polymeric nucleotides. The nucleotides are composed of a deoxyribose, a phosphate and a nucleobase i.e. adenine (A), thymine (T), cytosine (C) and guanine (G). The DNA double helix is made from complementary base pairing called Watson-Click base pairing and stabilized by $\pi$-$\pi$ stacking interaction between adjacent base pairs. The role of base pairing and $\pi$-$\pi$ stacking in assembling DNA double helix is an excellent example of supermolecular self-assembly [115]. Using the programmable self-assembly, DNA will be one of the most promising materials for highly sophisticated materials with two or three-dimensional structures.

As one of the excellent examples, Tanaka et al. succeeded in making complexes of $Cu^{2+}$ ions with the DNA double helix [20] using hydroxypyridone nucleobases. This advance is the replacement of Watson-Crick base pair in natural DNA by coordinate bond of metal [89]. An existence of the ferromagnetic interaction between electron spins on adjacent $Cu^{2+}$ ion centers has been found by using electron paramagnetic resonance (EPR) spectra [20]. However, Mizoguchi et al. reported that a natural B-DNA system with introduced $Mn^{2+}$ ions shows anti-ferromagnetic interaction [116]. From the EPR data, the $Cu^{2+}$-$Cu^{2+}$ distance was estimated to be $3.7 \pm 0.1$ Å, which is slightly longer than the distance between adjacent base pairs in natural B-DNA.

The first theoretical calculation of this system was reported by Zhang et al. based on their plane-wave calculations [91]. They showed that the ferromagnetic and anti-ferromagnetic phases are almost energetically degenerated but the ferromagnetic phase was slightly stable than anti-ferromagnetic phase. The authors also suggested that the nature of the $\sigma$ and $\pi$ frontier orbitals do not support bandlike electron conduction with nodes between the stacked planes. However, they also suggested that the efficient metal-base hybridization might cause alternative mechanisms, for example, by a

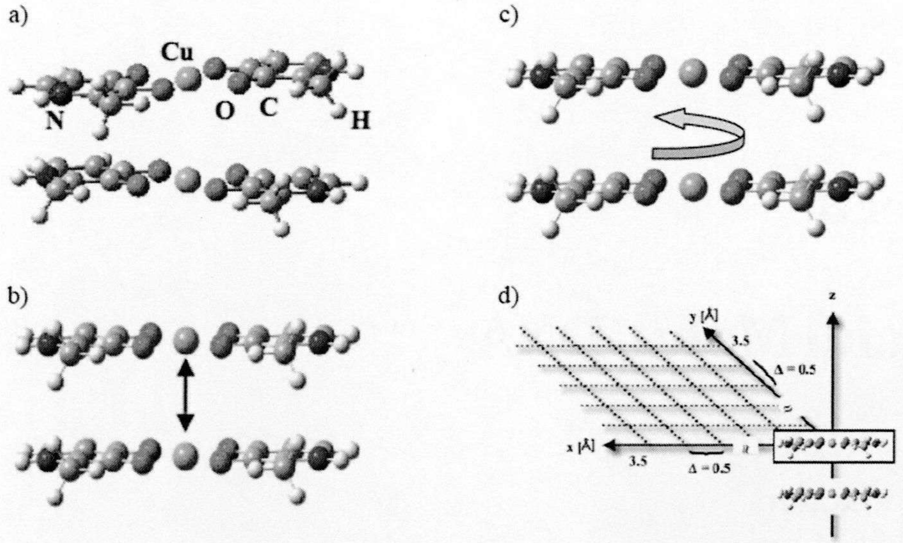

Figure 8.1: The Calculated dimer models of $Cu^{2+}$ mediated base pairs of hydroxypyridone nucleobases. Sugar-phosphate backbone is replaced by H atoms in the models. The structure (a) is the undistorted and (b)-(d) are distorted ones. Changed parameters are (b) the distance, (c) the rotaion angle and (d) the slip in X-Y plane between two monomers.

redox activity of inner cations.

The other development of incorporation of metal-base pair in DNA was carry out by Clever et al. using a metal-salen (salen = N,N'-bis(salicylidene)ethylenediamine) base pair in which a variety of metal ions could be introduced as coordination partners [21,97]. An advantage of using salen ligand is that the ethylenediamine (en) which is used to assemble the metal-salen complexes inside the DNA double strand forms a covalent crosslink, importing a high stability to the duplex. According to their study, the duplex stabilization based on salen ligand is much higher than that of any other metal-base pairs [21, 97, 111]. On the metal-salen complex, the dihedral angle between the planes defined by the aromatic rings is +22°, which is slightly larger than in natural base pairs [111].

In this paper, I quantitatively calculated effective exchange integral ($J_{ab}$) values between Cu(II) ions within a model structure of the and metal-hydroxypyridone and the metal-salen complexes as illustrated in Figure 8.1(a) and Figure 8.2(a), respectively, using unrestricted hybrid density functional theory (UHDFT) method. In order to consider effects of entanglement and dis-entanglement of the double helix chain, three types of structural disorders i.e. distance, rotation angle and discrepancy in XY-plane, are changed in the model dimer structure as illustrated in Figure 8.1(b)-(d) and Figure 8.2(b)-(d), respectively.

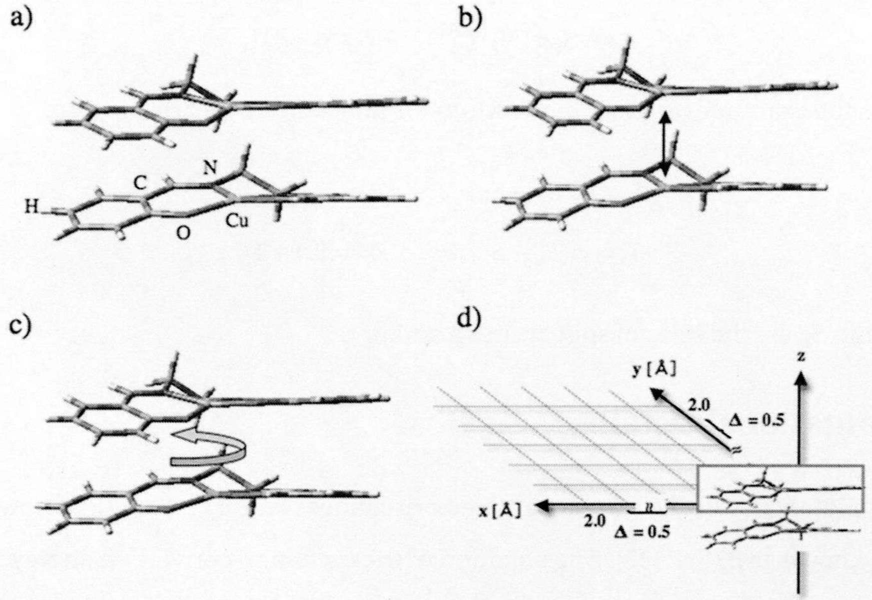

Figure 8.2: The calculation dimer models of $Cu^{2+}$ mediated base pairs of salen nucleobases. Sugar-phosphate backbone is replaced by H atoms in the models. The structure (a) is the undistorted and (b)-(d) are distorted ones. Changed parameters are (b) the distance, (c) the rotation angle and (d) the slip in X-Y plane between two monomers.

## 8.2 Theoretical Background

### 8.2.1 Effective Exchange Integral Value

An interaction between localized spins can be expressed by using Heisenberg Hamiltonian,

$$\hat{H} = -2\sum_{a,b} J_{ab}\hat{S}_a \bullet \hat{S}_b, \tag{8.1}$$

where the parameter $J_{ab}$ is a coupling parameter between localized spins S on metal ions a and b.

Yamaguchi et al. have proposed the approximate spin projection (AP) procedure by using Heisenberg Hamiltonian to eliminate the spin contamination [118, 134] as shown following equation,

$$J_{ab}^{(1)} = \frac{E_{BS}^{LS} - E_{BS}^{HS}}{\langle \hat{S}^2 \rangle_{BS}^{HS} - \langle \hat{S}^2 \rangle_{BS}^{LS}}, \tag{8.2}$$

where $E^X$ and $\langle \hat{S}^2 \rangle^X$ are total energy and total spin angular momentum of spin state $X$ ($X$ = LS and high-spin (HS) states), respectively. The positive (negative) $J_{ab}$ value means ferromagnetic (antiferromagnetic) interaction.

Eq. (8.2) is rewrite like Eq. (8.3) when there are many spin sites (N) [119],

$$J_{ab}^{(2)} = \frac{E^{LS} - E^{HS}}{\langle \hat{S}^2 \rangle^{HS} - \langle \hat{S}^2 \rangle^{LS} + c}, \tag{8.3}$$

where

$$c = -S_a g(N)\left[\langle \hat{S}^2 \rangle^{LS} - S_r(S_r+1)\right], \tag{8.4}$$

and $S_r$ denotes the exact spin angular momentum for molecules under discussion,

$$S_r = n(S_a - S_b) \quad (N = 2n), \tag{8.5}$$

$$S_r = n(S_a - S_b) + S_a \quad (N = 2n+1), \tag{8.6}$$

where the $S_a$ and $S_b$ are the sizes of spin at sites a and b.

## 8.3 Computational Details

In this study, I mainly use Becke's three parameter exchanges with Lee-Yang-Parr correlation functionals ($E_c^{LYP}$) known as B3LYP [38]. The equation of the exchange-correlation energy is as follow

$$E_{XC} = c_1 E_x^{\mathrm{HF}} + c_2 E_x^{\mathrm{Slater}} + c_3 E_x^{\mathrm{B88}} + c_4 E_c^{\mathrm{VWN}} + c_5 E_c^{\mathrm{LYP}}, \tag{8.7}$$

where $E_x^{\mathrm{HF}}$, $E_x^{\mathrm{Slater}}$, $E_x^{\mathrm{B88}}$ and $E_c^{\mathrm{VWN}}$ are the HF exchange energy, Slater exchange functional, the Becke88 exchange functional, the Vosko-Wilk-Nusair (VWN) correlation functional, respectively. These parameters are $c_1 = 0.2$, $c_2 = 0.8$, $c_3 = 0.72$, $c_4 = 0.19$ and $c_5 = 0.81$. Besides B3LYP, I used various exchange-correlation functionals, BHandHLYP [120], PW91PW91 [121], MPW1PW91 [122]. And I also examined by HF and MP2 [123], in order to elucidate dependency of $J_{ab}$ values on computational methods.

Calculating the $jab$ values of [H-Cu$^{2+}$-H]$_2$, I carried out it with 6-31+G* basis set for ligands, and Huzinaga MIDI+pd basis set [114] for Cu$^{2+}$ atoms on Gaussian03 program [82]. All $J_{ab}$ values between Cu$^{2+}$ ions in Cu$^{2+}$-DNA systems are calculated by two-unit dimer model as illustrated in Figure 8.1. Previous to the calculation of $J_{ab}$ values with the dimer model, a structure of the monomer unit is optimized because there is no available information about the complex except for the interplane distance. The dimer models are constructed by using the optimized monomers as described in later sections.

Calculating the $jab$ values of [S-Cu$^{2+}$-S]$_2$, I carried out it with 6-31G* basis set for ligands, and Huzinaga MIDI+pd basis set [114] for Cu$^{2+}$ atoms on Gaussian03 program [82]. To confirm the effects of the diffuse function for ligands, the $J_{ab}$ values were estimated with and without the diffuse function. As summarized in Table 8.5, the 6-31G* basis set gave $J_{ab}$ values of -0.7, -0.9, -0.6 and -0.1 eV for the various separation distance of the metal-salen dimer ([S-Cu$^{2+}$-S]$_2$) respectively, while the 6-31+G* basis set gave -0.6, -0.9, -0.6 and -0.1, respectively. The diffuse functions do not affect Jab

Table 8.1: Total energies, $\langle \hat{S}^2 \rangle$ of the HS and the BS LS states and $J_{ab}$ values of [**H**-$Cu^{2+}$-**H**]$_2$. The distance and angle between two base pairs are 3.7 Å and 36°, respectively.

| HS | | BS LS | | |
|---|---|---|---|---|
| Total Energy$^a$ | $\langle \hat{S}^2 \rangle$ | Total Energy$^a$ | $\langle \hat{S}^2 \rangle$ | $J^b_{ab}$ |
| -5030.22589113 | 2.0047 | -5030.22589734 | 1.0047 | -1.4 |

$^a$ in a.u.
$^b$ in $cm^{-1}$

values of the [**S**-$Cu^{2+}$-**S**]$_2$ quantitatively, so that the 6-31G* basis set is used for estimating $J_{ab}$ values, here. I constructed model structures based on the X-ray structure of the metal-salen base pair complex [111]. The structure of the metal-base pair in DNA, however, is difficult to decide whether it is the right handed or not, on the basis of experimental data, so that I assume that this structure is the right handed one. A distance between adjacent planes and rotation angle of the original structure are decided to be 3.375 Å and 36° on B-DNA form, respectively, as illustrated in Figure 8.2. Here I call this structure *original structure.*

## 8.4 Magnetism of the Hydroxypyridone Type M-DNA

### 8.4.1 $J_{ab}$ Values Between $Cu^{2+}$ Ions with the Reported Structure

First, the $J_{ab}$ value between two $Cu^{2+}$ ions is calculated for the reported structure [20]. As described above, I are only able to use the structural information of the complex that the system is a right-handed DNA helix and the distance of adjacent planes are 3.7 Å [20]. Therefore it is assumed that the Cu-Cu axis is perpendicular to monomer plane and the rotational angle of the dimer is 36° based on B-DNA [20, 89, 124], which is the right-handed DNA. By using those information and assumptions, I constructed the model system as illustrated in Figure 8.1(a). Calculated total energies and $\langle \hat{S}^2 \rangle$ values for a broken-symmetry (BS) LS and the HS states and $J_{ab}$ value are summarized in Table 8.1.

The calculated energy splitting between the BS LS and the HS states is small. However the BS LS state is slightly stable and the calculated $J_{ab}$ value is negative indicating an anti-ferromagnetic interaction. This result agrees with a Metal-DNA (M-DNA) based on a natural B-DNA ($J$ = -0.0483 $cm^{-1}$) [116].

Also I consider solvent (water) effect for this system by PCM method because ESR measurement carried out under condition of aqueous solution. The calculation result of the $J_{ab}$ value is -1.4 $cm^{-1}$ and it is equal to non-solvent model. In other word, the $J_{ab}$ value does not depend on the solvent effect in my model.

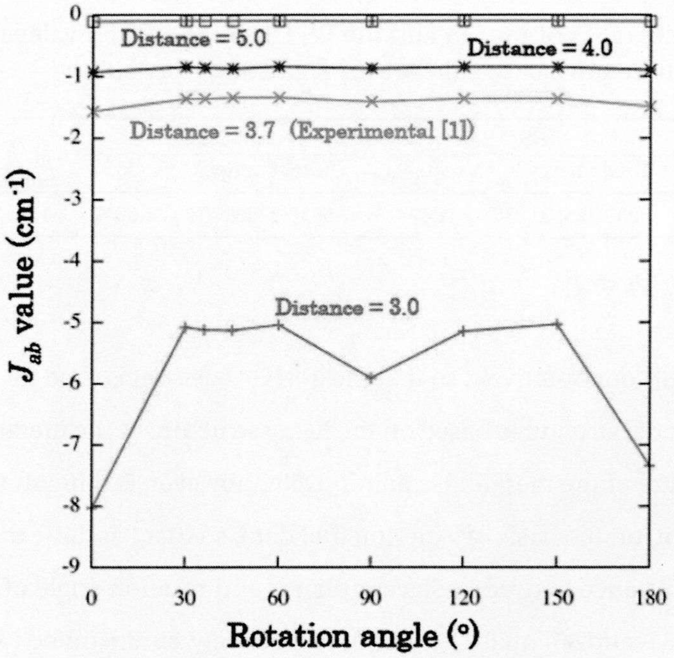

Figure 8.3: $J_{ab}$ values when the distance and the rotation angle between two base pairs are changed.

### 8.4.2 Change in $J_{ab}$ Values with Deformations

It is well known that the DNA is flickered and changed its form such as A-, B-and Z-forms by solvent [124]. In this sense, a structural disorder of the DNA strand must be examined for the consideration of the origin of high spin species. Therefore I, next, consider three possibilities of deformations i.e. the distance, the rotation angle and the slip in $X-Y$ plane between two monomers as illustrated in Figure 8.1(b)-(d), and examine a change in $J_{ab}$ values with those deformations.

Calculated results for the distance and the rotation angle are summarized in Figure 8.3. The range of Cu-Cu distance, and rotation angle are 3.0 - 5.0 Å and 0° - 180° , respectively. The experimental distance between two base pairs is 3.7 Å in B-form DNA. The calculated $J_{ab}$ values are small in all range of distances and angles. The $J_{ab}$ values simply depend on Cu-Cu distance and the antiferromagnetic interaction becomes stronger as the distance between two Cu ions becomes shorter, such as it was expected [125]. On the other hand, $J_{ab}$ values show a periodic dependency on the rotation angle. For example, there are minima around 0°, 90° and 180°. The reason of this phenomenon stems from the symmetry of orbitals of $Cu^{2+}$ ions of adjacent planes because the $J_{ab}$ values depend on overlap between two spin orbitals on $Cu^{2+}$ ions.

In order to explain the detail, the natural orbitals (NOs) of the system are examined for several angles. The NOs and their occupation numbers for the BS LS state are depicted in Figure 8.4 and

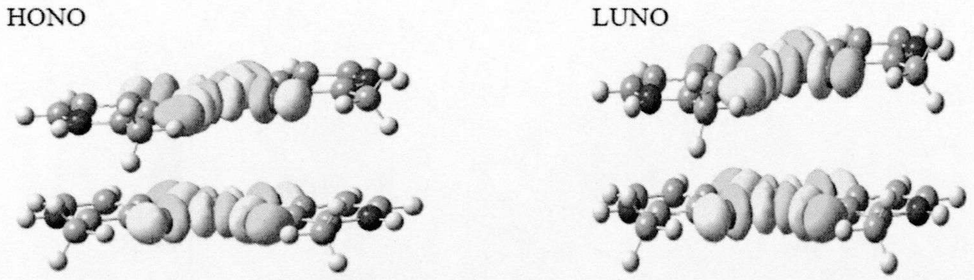

Figure 8.4: Depicted HONO and LUNO of [**H**-Cu$^{2+}$-**H**]$_2$ for the BS LS state. The distance and angle between two base pairs are 3.7 Å and 36°, respectively.

Table 8.2: The occupation number of HONO and LUNO of the BS LS state for [**H**-Cu$^{2+}$-**H**]$_2$. The distance between two base pairs is 3.7 Å.

| Angle$^a$ | HONO | LUNO |
|---|---|---|
| 0 | 1.0029 | 0.9971 |
| 30 | 1.0002 | 0.9998 |
| 36 | 1.0001 | 0.9999 |
| 45 | 1.0004 | 0.9996 |
| 60 | 1.0007 | 0.9993 |
| 90 | 1.0018 | 0.9982 |
| 120 | 1.0008 | 0.9992 |
| 150 | 1.0001 | 0.9999 |
| 180 | 1.0026 | 0.9974 |

$^a$ in degree

Table 8.2, respectively. The highest occupied natural orbital (HONO) and the lowest unoccupied natural orbital (LUNO) mainly consist of $d_{x^2-y^2}$ orbitals of Cu$^{2+}$ ions, and their occupation numbers are almost 1.0 indicating overlap between two spins on Cu$^{2+}$ ions are very small, allowing us to understand the weak magnetic interaction. Around 36° which is the angle of the B-DNA, overlap shows minimum but it is not completely orthogonal, while overlap shows maxima around 0°, 90° and 180°. The difference between 0° and 180° seems to originate from asymmetric methyl groups.

In case of 36°, the overlap estimated by the occupation number is 0.0001. In these systems, a slight structural change easily makes a change in overlap. If two orbitals are perpendicular each other, there is a possibility of the ferromagnetic interaction. As explained above, it is expected that the DNA backbone is always flickered by outer environment. So, I also investigate the slipping of two monomers in $X-Y$ plane as illustrated in Figure 8.1(d). In this model, rotation angle is fixed to 36°. As summarized in Figure 8.5, the $J_{ab}$ values become smaller and close to zero but they show anti-ferromagnetic interaction in whole region.

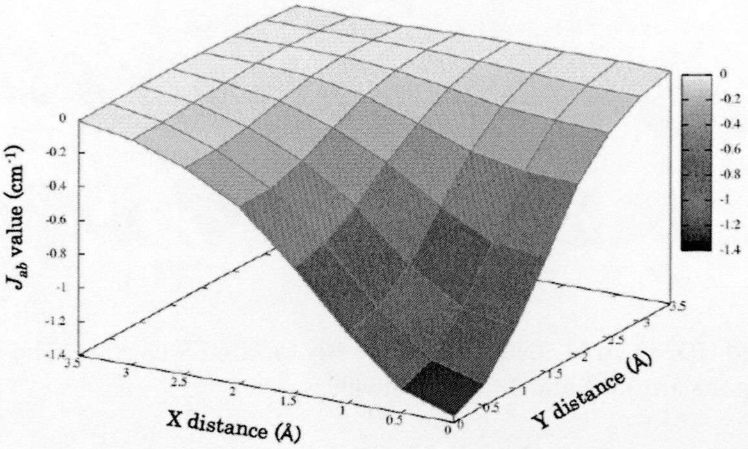

Figure 8.5: The change in $J_{ab}$ values when two monomers are slipped in $X-Y$ plane. The distance and angle between two base pairs are 3.7 Å and 36°, respectively.

Table 8.3: The $J_{ab}^{a}$ values of the dimer model calculated by several methods.

| Distance$^{b}$ | UBHandHLYP | UPW91PW91 | UMPW1PW91 | UHF | UMP2 |
|---|---|---|---|---|---|
| 3 | -5.1 | -3.5 | -4.5 | -2.4 | -4.6 |
| 3.7 | -1.2 | -0.8 | -0.9 | -0.4 | -0.4 |
| 4 | -0.7 | -0.6 | -0.6 | 0 | 0.4 |
| 5 | -0.1 | -0.1 | -0.1 | 0 | 2.1 |

$^{a}$ in cm$^{-1}$
$^{b}$ in Å

### 8.4.3 Dependence on the $J_{ab}$ Values for Various Calculation Methods

It has been reported calculated $J_{ab}$ values sometimes depend on the DFT functional sets quantitatively, but not qualitatively. Therefore, I next investigated the dependency of the Jab values on calculation methods such as BHandHLYP, PW91PW91, MPW91PW91, HF and MP2. Calculated results are shown in Table 8.3. Although the double helix of DNA is stabilized by $\pi-\pi$ interaction, the DFT methods which can not include $\pi-\pi$ interaction give systematic $J_{ab}$ values. MP2 can evaluate a dispersion interaction accurately. MP2 method shows an unreasonable weak ferromagnetic interaction at longer distance. On the other hand, the $J_{ab}$ values calculated by DFT methods are almost equal each other. Tsuzuki et al. reported that the MP2 calculation overestimate $\pi-\pi$ interaction such as benzene or naphthalene [126, 127]. my results also suggest the method may not be applicable to the long-distance [**H**-Cu$^{2+}$-**H**]$_2$ dimer.

Table 8.4: Total energies, $\langle\hat{S}^2\rangle$ values and $J_{ab}$ values of trimer (n=3), tetramer (n=4) and pentamer (n=5) models calculated by UB3LYP method.

| | HS | | BS LS | | |
|---|---|---|---|---|---|
| n | Total Energy[a] | $\langle\hat{S}^2\rangle$ | Total Energy[a] | $\langle\hat{S}^2\rangle$ | $J_{ab}^{b}$ |
| 3 | -7545.34013157 | 3.7570 | -7545.34014415 | 1.7572 | -1.4 |
| 4 | -10060.4546255 | 6.0093 | -10060.4546442 | 2.0096 | -1.4 |
| 5 | -12575.5689211 | 8.7617 | -12575.5689460 | 2.7620 | -1.4 |

[a] in a.u.
[b] in $\text{cm}^{-1}$

### 8.4.4 The $J_{ab}$ Values of Trimer, Tetramer and Pentamer

In order to examine the dependency of the $J_{ab}$ values on a chain length, I calculated the $J_{ab}$ values of trimer, tetramer and pentamer models. In these methods, the distance between adjacent planes are 3.7 Å and rotation angle are 36°. The results are shown in Table 8.4. Their total energies of HS and BS LS states are energetically degenerate but the BS LS is slightly stable. Interestingly, the calculated $J_{ab}$ values are equal to dimer model. In other words, I can not find a dependency of $J_{ab}$ values on the chain length.

### 8.4.5 Possibility of thermal excitation

From the calculated results, I can not find the structure in which the HS state is more stable than the BS LS state, although EPR spectra show the existence of the HS species. On the other hand, the HS and the BS LS states are energetically degenerate. So, I examine a possibility of the thermal excitation from the LS state to the HS state. The ratio of population in the HS (triplet) and in the LS (singlet) is estimated by the Boltzmann distribution,

$$\frac{N(\text{triplet})}{N(\text{singlet})} = \exp\left(-\frac{E^{\text{triplet}} - E^{\text{singlet}}}{k_{\text{B}}T}\right), \tag{8.8}$$

at the various temperature ($T$) [128] in case that the distance and the rotation angle between two monomers are 3.7 Å and 36°. As illustrated in Figure 8.6, a percentage of the triplet state

$$\frac{N(\text{triplet})}{N(\text{singlet}) + N(\text{triplet})} \times 100$$

is estimated to be about 21 % at 1.5 K (ESR measurement temperature) and about 50 % at 300 K. The result suggests that the HS species exist by the thermal excitation even at 1.5 K.

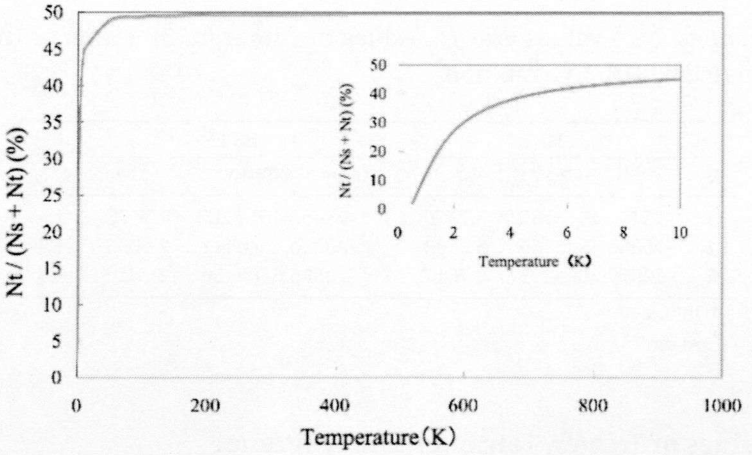

Figure 8.6: The ratio of the population on triplet states by Boltzmann distribution simulation. The distance and angle between two base pairs are 3.7 Å and 36°, respectively. $Ns$ and $Nt$ means the population of singlet and triplet states, respectively. The enlarged picture shows the range of low temperature.

## 8.5 Magnetism of the Salen Type M-DNA

### 8.5.1 $J_{ab}$ Values between $Cu^{2+}$ Ions for the Original Structure with and without the Backbones

The $J_{ab}$ values between two $Cu^{2+}$ ions are calculated for the original structure with and without backbones (sugar-phosphate) of [**S**-$Cu^{2+}$-**S**]$_2$. By using those assumptions, I constructed the model system as illustrated in Figure 8.2(a) and Figure 8.7. Calculated total energies, $\langle \hat{S}^2 \rangle$ values and the $J_{ab}$ values of models without backbone are summarized in Table 8.5. Results with backbones are also summarized in Table 8.6.

Within the both models, the calculated energy splitting between the BS LS and the HS states is small. However the BS LS state is slightly stable and the calculated $J_{ab}$ values are negative, indicating an anti-ferromagnetic interaction. This result agrees with experimental Jab values of a Metal-DNA (M-DNA) based on a natural B-DNA ($J$ = -0.0483 $cm^{-1}$) [116]. The $J_{ab}$ values of with- and without-backbone models are same. These results can be easily understood by the natural orbitals (NOs) analysis. The NOs for the BS LS state are depicted in Figure 8.8. The highest occupied natural orbital (HONO) and the lowest unoccupied natural orbital (LUNO) mainly consist of orbitals of $Cu^{2+}$ ions, and their occupation numbers are almost 1.0, indicating that overlap between two spins on $Cu^{2+}$ ions are very small. In âĂIJwith-backboneâĂİ model, I can not find population on backbone atoms, and occupation number of HONO is same to that of âĂIJwithout-backboneâĂİ model. These results indicate that backbone does not affect SOMO-SOMO overlap. Therefore the $J_{ab}$ values of two models

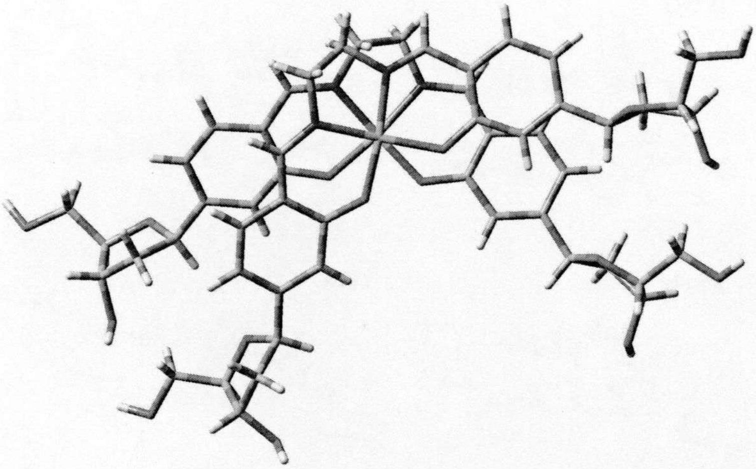

Figure 8.7: Top view structure of [**S**-$Cu^{2+}$-**S**]$_2$ with backbones.

Table 8.5: Total energies, $\langle \hat{S}^2 \rangle$ of the HS and the BS LS states and $J_{ab}$ values of [**S**-$Cu^{2+}$-**S**]$_2$ for the various distance between adjacent planes at the UB3LYP/6-31G* level.

| | HS | | BS LS | | |
|---|---|---|---|---|---|
| Distance[a] | Total Energy[b] | $\langle \hat{S}^2 \rangle$ | Total Energy[b] | $\langle \hat{S}^2 \rangle$ | $J_{ab}^{c}$ |
| 3 | -5035.92722253 | 2.0063 | -5035.92722550 | 1.0064 | -0.7<br>(-0.6)[d] |
| 3.375 | -5036.06572735 | 2.0062 | -5036.06573139 | 1.0063 | -0.9<br>(-0.9)[d] |
| 4 | -5036.12941566 | 2.0062 | -5036.12941832 | 1.0063 | -0.6<br>(-0.6)[d] |
| 5 | -5036.13858055 | 2.0062 | -5036.13858117 | 1.0062 | -0.1<br>(-0.1)[d] |

[a] in Å
[b] in a.u.
[c] in $cm^{-1}$
[d] $J_{ab}$ values calculated by UB3LYP/6-31+G* are in parentheses

Table 8.6: Total energies, $\langle \hat{S}^2 \rangle$ of the HS and the BS LS states and $J_{ab}$ values of [**S**-$Cu^{2+}$-**S**]$_2$ with backnones. The distance and angle between two base pairs are 3.375 Å and 36°, respectively.

| HS | | BS LS | | |
|---|---|---|---|---|
| Total Energy[a] | $\langle \hat{S}^2 \rangle$ | Total Energy[a] | $\langle \hat{S}^2 \rangle$ | $J_{ab}^{b}$ |
| -6719.75910069 | 2.0061 | -6719.75910490 | 1.0063 | -0.9 |

[a] in a.u.
[b] in $cm^{-1}$

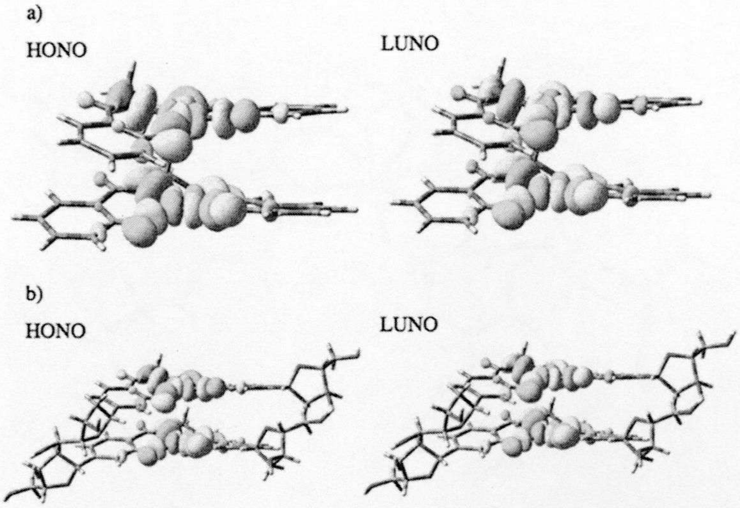

Figure 8.8: Depicted HONO and LUNO of [**S**-$Cu^{2+}$-**S**]$_2$ (a) without and (b) with backbones for the BS LS state. The distance and angle between adjacent planes are 3.375 Å and 36°, respectively.

are same. Also I consider solvent (water) effect by using PCM method on the original structure. The calculated $J_{ab}$ value is -0.8 cm$^{-1}$ and it is almost equal to non-solvent model. These results suggested that the $J_{ab}$ value does not depend on a chemicl environment by solvent.

### 8.5.2 Change in $J_{ab}$ Values with Deformations

It is well known that the DNA is flickered and changed their forms such as A-, B-and Z-forms by solvent [124]. In this sense, a structural disorder of the DNA strand must be examined for the consideration of the magnetic interaction. Therefore I, next, consider three possibilities of deformations i.e. the distance, the rotation angle and the slip in $X-Y$ plane between two monomers as illustrated in Figure 8.2(b)-(d), and examine a change in $J_{ab}$ values with those deformations. Calculated results for each distance and rotation angle are summarized in Table 8.5 and 8.7, respectively. The range of the separated distance and rotation angle are 3.0 - 5.0 Å and 0° - 180°, respectively. The calculated $J_{ab}$ values are small in all range of distances and angles. Interestingly, the $J_{ab}$ values are not in proportion to the separated distance. These is a minimam around 3.375 Å. In addition, $J_{ab}$ values do not show a periodic dependency on the rotation angle. For example, there are minima around 120° and 150°. Usually, it should be minima around 0°, 90° and 180° when the symmetry of orbitals of $Cu^{2+}$ ions of adjacent planes are considered, because the $J_{ab}$ values depends on overlap between two spin orbitals on $Cu^{2+}$ ions. The reason of this phenomenon is originated from the twisted salen structure as explained in section 8.5.4.

Table 8.7: Total energies, $\langle \hat{S}^2 \rangle$ of the HS and the BS LS states and $J_{ab}$ values of [S-$Cu^{2+}$-S]$_2$ for the various angle between adjacent planes.

| | HS | | BS LS | | |
|---|---|---|---|---|---|
| Angle$^a$ | Total Energy$^b$ | $\langle \hat{S}^2 \rangle$ | Total Energy$^b$ | $\langle \hat{S}^2 \rangle$ | $J^c_{ab}$ |
| 0 | -5036.063256 | 2.0062 | -5036.063263 | 1.0063 | -1.6 |
| 30 | -5036.041807 | 2.0062 | -5036.041812 | 1.0063 | -1.0 |
| 36 | -5036.06573 | 2.0062 | -5036.065734 | 1.0063 | -0.9 |
| 60 | -5036.067922 | 2.0064 | -5036.067935 | 1.0063 | -2.9 |
| 90 | -5036.069829 | 2.0063 | -5036.06984 | 1.0063 | -2.4 |
| 120 | -5036.062881 | 2.0063 | -5036.062894 | 1.0063 | -3.0 |
| 150 | -5036.099327 | 2.0063 | -5036.099335 | 1.0063 | -2.0 |
| 180 | -5036.135059 | 2.0062 | -5036.135065 | 1.0063 | -1.2 |

$^a$ in degree
$^b$ in a.u.
$^c$ in $cm^{-1}$

Table 8.8: The occupation number of HONO and LUNO of the BS LS state for [S-$Cu^{2+}$-S]$_2$. The distance between two base pairs is 3.375 Å.

| Angle$^a$ | HONO | LUNO |
|---|---|---|
| 0 | 1.0029 | 0.9971 |
| 30 | 1.0022 | 0.9978 |
| 36 | 1.0004 | 0.9996 |
| 45 | 1.0003 | 0.9997 |
| 60 | 1.0117 | 0.9883 |
| 90 | 1.0108 | 0.9892 |
| 120 | 1.0104 | 0.9896 |
| 150 | 1.0084 | 0.9916 |
| 180 | 1.0040 | 0.9960 |

$^a$ in degree

In order to explain the detail, the NO analyses are carried out for several angles. The occupation numbers of the BS LS state are depicted in Table 8.8. All of their occupation numbers for HONO and LUNO are almost 1.0 indicating overlap between two spins on $Cu^{2+}$ ions are very small.

As explained above, it is expected that the DNA backbone is always flickered by outer environment. So, I also estimate the slipping of two monomer in $X-Y$ plane as illustrated in Figure 8.2(d). In this model, separated distance and rotation angle are fixed to 3.375 Å and 36°, respectively. As summarized in Figure 8.9, the $J_{ab}$ values do not show a simple behavior because of the twisted structure of salen, but anti-ferromagnetic interaction is observed in whole region.

### 8.5.3 Dependency of the $J_{ab}$ Values on Various Calculation Methods

It has been reported calculated $J_{ab}$ values sometimes depend on the DFT functional sets quantitatively, but not qualitatively. Therefore, I next investigated the dependency of the $J_{ab}$ values on cal-

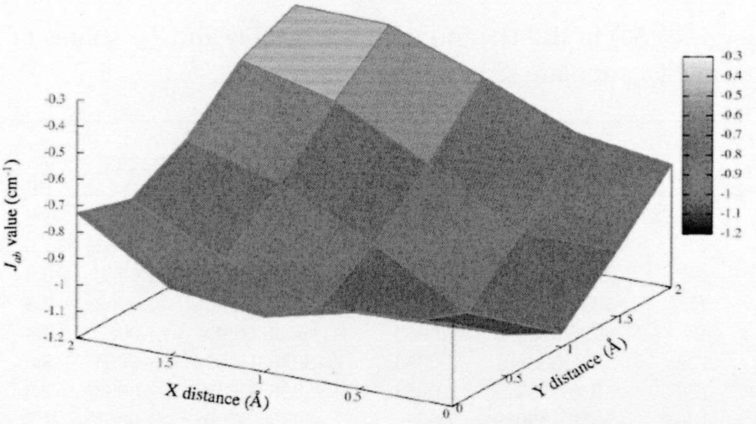

Figure 8.9: The change in Jab values when two monomer are slipped in $X-Y$ plane. The distance and angle between adjacent planes are 3.375 Å and 36°, respectively.

Table 8.9: The $J_{ab}^{a}$ values for various calculation methods.

| Distance$^{b}$ | UBHandHLYP | UPW91PW91 | UMPW1PW91 | UHF | UMP2 |
|---|---|---|---|---|---|
| 3 | -2.6 | 3.4 | -0.5 | -1.1 | -2.8 |
| 3.375 | -1.5 | 0.5 | -0.6 | -0.2 | -0.4 |
| 4 | -0.6 | -0.3 | -0.4 | 1.2 | 92.2 |
| 5 | -0.1 | -0.2 | -0.1 | 3.2 | -24.4 |

$^{a}$ in cm$^{-1}$
$^{b}$ in Å

culation methods such as BHandHLYP, PW91PW91, MPW91PW91, HF and MP2. Calculated results are shown in Table 8.9. Although the double helix of DNA is stabilized by $\pi-\pi$ interaction, the DFT method which does not include $\pi-\pi$ interaction gives systematic $J_{ab}$ values. B3LYP, BHandHLYP and MPW1PW91 functional contain 20%, 50% and 25% HF exchange, respectively. From the results, it can be seen that the $J_{ab}$ values depend on a ratio of HF exchange, but not depend on a correlation functional. In PW91PW91 (0% HF exchange), the $J_{ab}$ value is a weak ferromagnetic interaction for the original structure. In MP2, the absolute values of the $J_{ab}$ are larger at a long distance as compared others methods. This result of MP2 is unreasonable because magnetic interaction should be close to zero at a long distance. Tsuzuki et. al. reported that the MP2 calculation overestimate $\pi-\pi$ interaction such as benzene or naphthalene [129, 130]. my results also suggest the method may not be applicable to the long-distance [**S**-Cu$^{2+}$-**S**]$_2$.

### 8.5.4 Change in the $J_{ab}$ Values for Planer [S-Cu$^{2+}$-S]$_2$ without Ethylenediamine

As described above, on the metal-salen complex structure, the dihedral angle between the planes defined by the aromatic rings was +22° because of crosslink by ethylenediamine. If the metal-salen

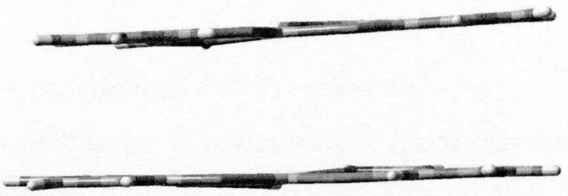

Figure 8.10: Structure of [**S**-Cu$^{2+}$-**S**]$_2$ without ethylenediamine

Table 8.10: Total energies, $\langle \hat{S}^2 \rangle$ of the HS and the BS LS states and $J_{ab}$ values of [**S**-Cu$^{2+}$-**S**]$_2$ without en. The angle between adjacent planes is 36°.

| | HS | | BS LS | | |
|---|---|---|---|---|---|
| Distance[a] | Total Energy[b] | $\langle \hat{S}^2 \rangle$ | Total Energy[b] | $\langle \hat{S}^2 \rangle$ | $J^c_{ab}$ |
| 3 | -4881.319981 | 2.006 | -4881.320001 | 1.0062 | -4.3 |
| 3.375 | -4881.341747 | 2.006 | -4881.341757 | 1.0062 | -2.2 |
| 4 | -4881.347789 | 2.006 | -4881.347793 | 1.0061 | -0.9 |
| 5 | -4881.347065 | 2.0061 | -4881.347065 | 1.0061 | -0.1 |

[a] in Å
[b] in a.u.
[c] in cm$^{-1}$

monomer does not have the linking en, it will be planer complex. Therefore. I examined the $J_{ab}$ values of planer [**S**-Cu$^{2+}$-**S**]$_2$ without en to elucidate the effect of the twist structure of ligand. I changed the dihedral angel into 0° by removing en from [**S**-Cu$^{2+}$-**S**]$_2$ as shown in Figure 8.10. The calculated results are shown Table 8.10. The calculated $J_{ab}$ values are small in all range of distances. The $J_{ab}$ values depend on the separated distance and the anti-ferromagnetic interaction becomes stronger as the distance between two Cu ions becomes shorter. From the result, the reason that, $J_{ab}$ values of [**S**-Cu$^{2+}$-**S**]$_2$ is not in proportion to the dimer distance seems to come from the twisted structure of the ligand.

## 8.6 Conclusion

I theoretically investigated an origin of HS species of $Cu^{2+}$ bridged hydroxypyridone pairs observed by EPR spectra. To my knowledge, this is the first report of a quantitative calculation for $J_{ab}$ value between $Cu^{2+}$ ions in metal-DNA systems. In all calculated results, the total energies of the HS and the BS LS states are degenerate but $J_{ab}$ values show weak anti-ferromagnetic couplings within the examined model structures. These results agree with Metal-DNA based on natural B-DNA [116]. Also $J_{ab}$ value for dimer model is equal to more than trimer models that the distance and the angel are 3.7 Å and 36°. Together with the result of the Boltzmann distribution simulation, it is expected that the thermal excitation from the LS state to the HS state occurs in the system and the HS species are observed by the EPR spectroscopy.

I also theoretically investigated magnetism of $Cu^{2+}$ bridged salen-base pairs. To my knowledge, this is the first report on the magnetism for this system. In all calculated results using UB3LYP, the total energies of the HS and the BS LS states are degenerated but $J_{ab}$ values show weak anti-ferromagnetic couplings within the examined model structures. These results agree with Metal-DNA based on natural B-DNA [116]. So, I can conclude that artificial Metal-DNA (especially this system) shows anti-ferromagnetic interaction, which is consistent with the experimental result. The $J_{ab}$ values strongly depend on the ligand structure caused by en but not backbones.

Seeman et al. reported pioneering studies of DNA nano-architectures. They made, for example, the self-assembly of branched DNA molecules into a two-dimensional crystal and ligated DNA molecules form interconnected rings to create a cube-like structure [131]. Using these structures, it is possible to create a new material by arranging molecules in space precisely. Assimilating SeemanâĂŹs structures and the metal-base pair in DNA, it is also possible to create a new magnetic material by arranging metals with spins. From my results, it seems to be effective to design the angle of aromatic ring to control the magnetic properties.

# Chapter 9

# Periodic Boundary Condition

## 9.1 Introduction

Recent interest in one-dimensional (1D) metal complexes, such as a quasi 1D halogen-bridged binuclear metal complex (MMX chain) [132–134] and an artificial metal-DNA (M-DNA) [20, 21], has spurred on researches, especially about their physical and chemical properties such as metallic conductivity [133], strong anti-ferromagnetism [134] and ferromagnetism [20] in material science.

There are internal degrees of freedom of charge and spin distributions in binuclear part of MMX chain that contains metal-metal bond, so this system shows four electronic phases such as averaged-valence phase (AV), alternate-charge-polarization phase (ACP), charge-polarization phase (CP) and charge-density-wave phase (CDW). Very recently, my group reported electronic structures, CDW/CP stability and magnetic properties of $K_4[Pt_2(pop)_4X]\cdot 2H_2O$ (X = Cl, Br) complexes, by using the cluster model [135]. Calculated results indicated that the CDW state was a ground state and the CP state was a excited state for both complexes, and also indicated a strong anti-ferromagnetic intra-chain interaction. The artificial M-DNA is the system that contains metal ions in the middle of DNA, which is substituted by an artificial ligand, so that metal ions can arrange one-dimensionally [20, 21]. In 2004, Tanaka et al. succeeded in the complexation of up to five $Cu^{2+}$ ions using hydroxypyridone as a ligand inside an artificial DNA double helix (below transcribed [**H**-$Cu^{2+}$-**H**]), and reported that [**H**-$Cu^{2+}$-**H**] shold a ferromagnetic interaction by using electron paramagnetic resonance (EPR) spectra [20]. However, Zhang et al. reported that the ferromagnetic (**F**) and the anti-ferromagnetic (**AF**) phases were energetically degenerated but the anti-ferromagnetic phase was a ground state [91]. my group demonstrated that the thermal excitation from the **AF** state to the **F** state would occur in the system by calculated $J_{ab}$ values with the cluster model and the result of the Boltzmann distribution simulation [93].

Many groups have often utilized $J_{ab}$ value, which are defined by the Heisenberg model, for elucidating magnetism. Calculation of $J_{ab}$ value for a "periodic" system such as a MMX and an artificial M-DNA, are usually classified into two ways. One is the method that divides the periodic system into a small cluster (fragment) model. The other is the method using the periodic boundary conditions. However, it is very difficult to calculate $J_{ab}$ value for periodic systems. So, to estimate Jab value of those systems, I have to construct the corresponding cluster model.

In general, there is arbitrariness which method a scientist uses (mostly a chemist often use the former method, and a physicist tends to use the latter one). However, to my knowledge, there has been no report about a comparison with cluster model and the periodic boundary condition approaches for the effective exchange integral value. In this paper, I compare an effective exchange integral ($J_{ab}$) value of cluster model and the periodic boundary conditions.

I examine differences between various hydrogen cluster models $H_2$, $H_4$ and $H_{100}$, and the models with the periodic boundary conditions in term of $J_{ab}$ values of Heisenberg and Ising model.

## 9.2 Theoretical Background

### 9.2.1 UHF and UDFT Solutions for Polyradicals

Here I briefly explain basic concept of ab initio calculations of Jab value. I start to consider the potential curve of linear clusters with a variation of the interatomic distance as illustrated in Figure 9.1.

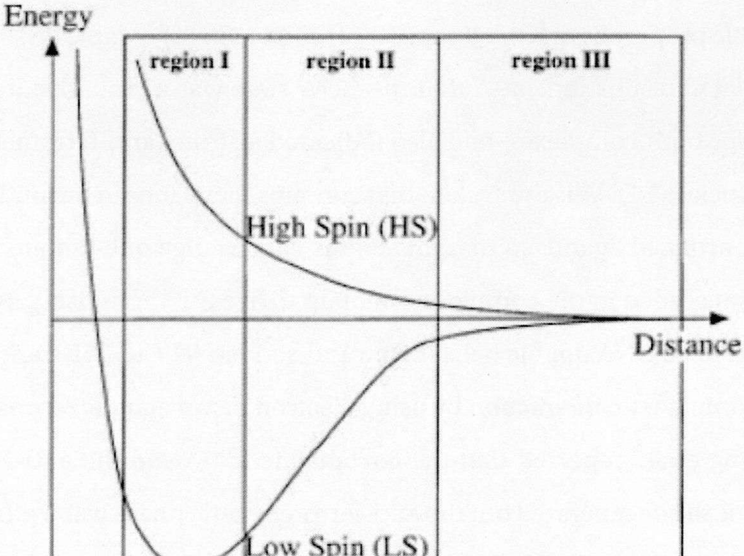

Figure 9.1: The illustration of the potential curve of one-dimension cluster with various interatomic distance (quotation from ref. [119])

The interaomic distance is often classified into three regions [119,136]. Region I is a nonmagnetic or weak correlation region which is characterized by strong orbital interaction and the formation of strong covalent bond. Region III is regarded as being a magnetic region where component radicals exhibit weak intermolecular interactions. Region II is characterized as a transition region from the nonmagnetic region I to the magnetic region III. However, the intrinsic difficulties arise in the dissociation process of a covalent bond from region I to III using restricted HF and DFT (RHF and RDFT). These methods cannot express the dissociation process Ill. Improved this point, it is often used the broken-symmetry (BS) method such as unrestricted density functional theory (UDFT) and unrestricted Hartree-Fock (UHF) approximately involves the static correlation correction by splitting $\alpha$ and $\beta$ electrons into two different orbitals, namely different orbitals for different spins (DODS) approach. The bifurcation of the RHF or RDFT close shell MOs into the UHF or UDFT MOs occurs at the triplet (T) instability threshold where the lowest eigenvalues of the T-instability matrix is zero. This means that $J_{ab}$ value around the instability threshold involves a difficulties.

The UHF and UDFT methods offer qualitatively correct orbital pictures and the orbital correlation diagram for the dissociation of a covalent bond being applicable to biradical and polyradical species. However, the low-spin (LS) species of BS method suffer from a spin contamination of higher spin states, which influence total energy, optimized geometry, excited energy and so on.

## 9.3 Computation Details

I calculated $J_{ab}$ values of $[\mathrm{H}]_n$ (n = 2, 4, 100) cluster models, and ones of $H_2$ and $H_4$ models with the periodic boundary conditions (below transcribed PBC such as pbc-$H_2$ and pbc-$H_4$) as shown Figure 9.2.

For all models, the total energies and $\langle \hat{S}^2 \rangle$ values are calculated by UBLYP [137], UBHandHLYP [138], UB3LYP [38], and UHF methods with the use of 6-31G**. The calculation that was not PBC (below transcribed non-PBC) was performed with Gaussion03 program [82]. The PBC calculation was performed with CRYSTAL06 program [139].

For calculated spin states of $H_{100}$ model are the highest (s = 50) and BS LS (alternate spin (↑ ↓ ↑ ↓ . . . ↑ ↓ ↑ ↓) states. I estimated $J$, $J'$ and $J''$ values of $H_4$ models with and without the PBC by considering four types spin direction such as (a, b, c, d) = (↑ ↑ ↑ ↑), (↑ ↓ ↑ ↓), (↑ ↓ ↓ ↑), (↑ ↑ ↓ ↓) as shown Figure 9.2(b).

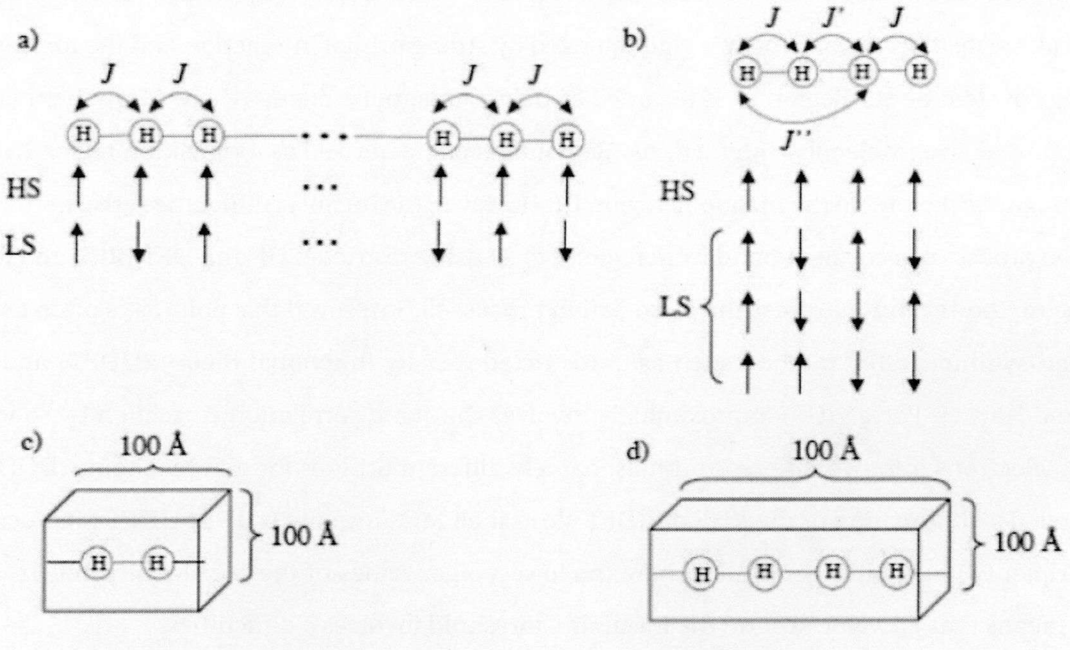

Figure 9.2: Calculated models. a) Two spin states (HS and BS LS) required for the calculation of $J_{ab}$ of $[\mathrm{H}]_n$ (n = 2, 100) model. b) Four spin states (HS and BS LS) required for the calculation of $J_{ab}$ of a) $H_4$ model. c) Unit cell and two spin states (HS and BS LS) required for the calculation of $J_{ab}$ of pbc-$H_2$. d) Unit cell and four spin states (HS and BS LS) required for the calculation of $J_{ab}$ of pbc-$H_4$.

## 9.4 Results and Discussion

### 9.4.1 Discussion on $H_2$, $H_{100}$ and pdc-$H_2$ models

**Potential Energies**

I investigated the potential energies of the HS and the BS LS solutions for $H_2$, $H_{100}$ and pdc-$H_2$ models.

I show the relative energies of the HS and the BS LS states for $H_{100}$ defined as $\Delta E = E(H_{100}) - 100E(H)$ in Figure 9.3. $\langle \hat{S}^2 \rangle$ values of BS LS state for $H_2$ and $H_{100}$ was also summarized in Table .

The potential energies of the HS state of $H_{100}$ and $H_2$ do not have a minimum value because there is no covalent bond between hydrogen atoms as shown Figure 9.3(a). The relative energies of BS LS state with AP procedure are almost equal to BS LS state without AP procedure as shown Figure 9.3. This is understood as the following procedure. The total energy for many spin sites with AP procedure is given by

$$\Delta E(AP) = E^{LS}(AP) - E^{LS} = J_{ab}^{(2)}\left[\langle \hat{S}^2 \rangle^{LS} - S_r(S_r+1)\right][1 - h(N)]. \tag{9.1}$$

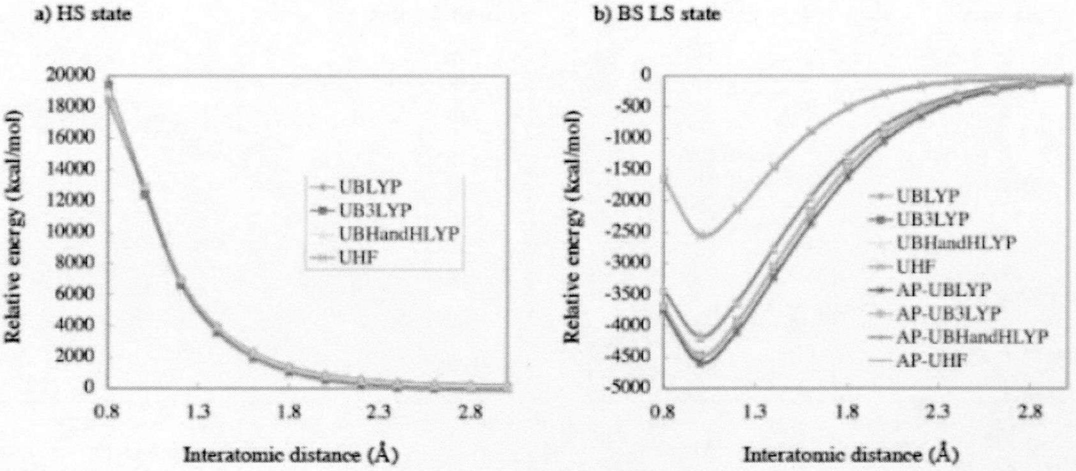

Figure 9.3: Relative energies of a) the HS and b) the BS LS states with and without the AP procedure for $H_{100}$.

where

$$h(N) = (N-2)^2/N^2 \quad \text{(for N > 2 and even number)}, \tag{9.2}$$

or

$$h(N) = (N-3)/(N+1) \quad \text{(for N > 2 and odd number)}, \tag{9.3}$$

And substitute Eq. 9.2, 9.3 for Eq. 9.1. Then I can gain the following equation.

$$\Delta E(AP) = J_{ab}^{(2)}\left[\langle \hat{S}^2 \rangle^{LS} - S_r(S_r+1)\right]\left[1-\left(1-\frac{4}{N}+\frac{4}{N^2}\right)\right], \tag{9.4}$$

or

$$\Delta E(AP) = J_{ab}^{(2)}\left[\langle \hat{S}^2 \rangle^{LS} - S_r(S_r+1)\right]\left[1-\left(\frac{1-3/N}{1+1/N}\right)\right]. \tag{9.5}$$

Finally, I take a limit for N,

$$\lim_{x\to\infty} \Delta E(AP) = 0 \tag{9.6}$$

Therefore the modified energy by spin projection has little advantage for a large cluster model. The potential energies of the BS LS state of $H_{100}$ have a minimum value around 1.0 Å regardless of the calculation methods. However the value of $H_2$ is around 0.8 Å. An order of $|\Delta E|$ in each calculation methods is $|\Delta E(\mathrm{UHF})| \ll |\Delta E(\mathrm{UBHandHLYP})| < |\Delta E(\mathrm{UB3LYP})| < |\Delta E(\mathrm{UBLYP})|$. DFT methods often tend to stabilize the LS state than HF method since the hybridization parameters involved in the exchange-correlation term are fitted to evaluate usual bonding energies, so that $\Delta E$ is quite different between HF and DFT methods. The $|\Delta E|$ for DFT methods became large with the increase of the rate of Hartree-Fock exchange term.

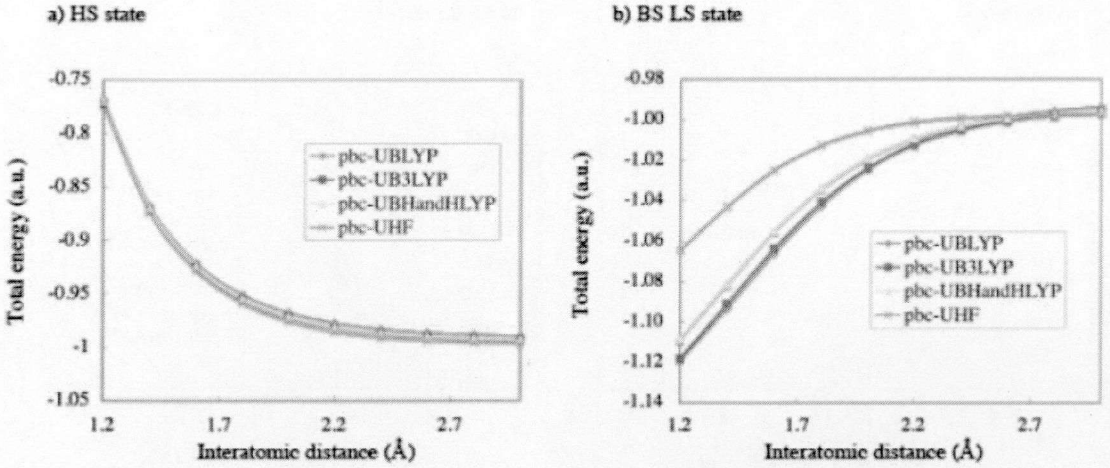

Figure 9.4: Total energies of a) the HS and b) the BS LS states for pbc-$H_2$.

I show the total energies of the HS and the BS LS states of pbc-$H_2$ in Figure 9.4.

The tendency of pbc-$H_2$, that is the following order; $|\Delta E(\mathrm{UHF})| \ll |\Delta E(\mathrm{UBHandHLYP})| < |\Delta E(\mathrm{UB3LYP})| < |\Delta E(\mathrm{UBLYP})|$, are almost equal to non-PBC models for both the HS and the BS LS states.

**Effective Exchange Integral Value**

I next investigated the dependency of the $J_{ab}$ values on interatomic distance for $H_2$, $H_{100}$ and pbc-$H_2$ models. The pbc-$H_2$ was estimated the spin-unprojected $J_{ab}$ values. $J_{ab}^{(1)}$ and $J_{ab}^{(2)}$ values based on the AP procedure are given by Eq. 8.2 or 8.3. $J_{ab}^{(3)}$ value based on spin-unprojected procedure is obtained by following scheme. On dealing with the spin operator of Eq. 8.1 as a classical spin, $J_{ab}^{(1)}$ value is calculated by the following equation (called Ising model),

$$J_{ab}^{(3)} = \frac{E^{LS} - E^{HS}}{4(N-1)S_a S_b}. \tag{9.7}$$

I show the calculated results of the various $J_{ab}$ values with the change of interatomic distance in Figure 9.5.

In the strong overlap region I (R ≤ 1.8 Å) in Figure 9.5(a), $J_{ab}^{(1)}$ and $J_{ab}^{(3)}$ values of $H_2$ are quite different, while in the weak bonding region III ( 2.7 ≤ R ≤ 3.0 Å) their values are similar, The difference between and originates a spin contamination. On the other hand, in the region I in Figure 5b, $J_{ab}^{(1)}$ and $J_{ab}^{(3)}$ values of $H_{100}$ are completely different. This is because of both a spin contamination and a long-distance interaction between local spins described later.

There are edge effects in a cluster model, but not in PBC model. As a chain becomes longer, the effects hardly influence it. $J_{ab}^{(3)}$ values of pbc-$H_2$ are almost equal to that of $H_{100}$, but not equal to $H_2$

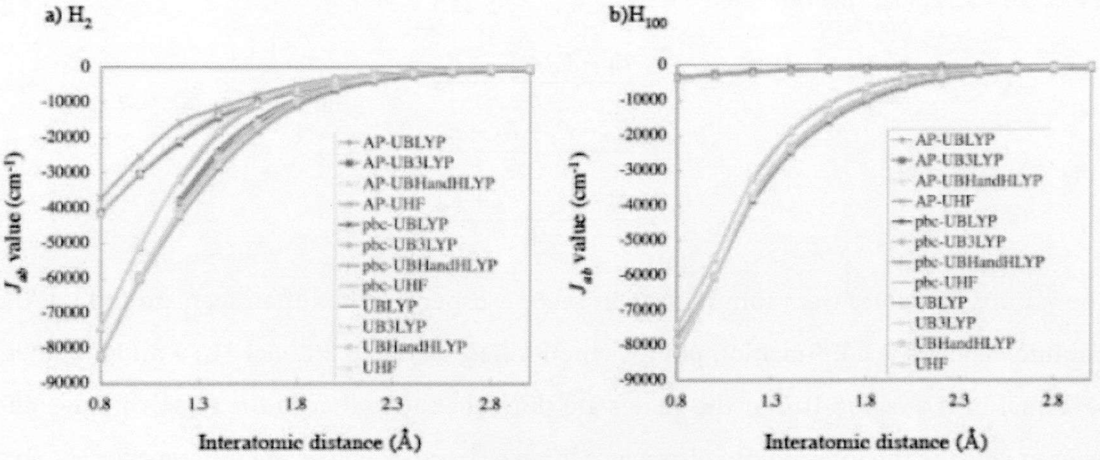

Figure 9.5: $J_{ab}$ values for a) $H_2$ and b) $H_{100}$ with and without the AP procedure.

of cluster model. This seems to be caused by edge effects of local spins, that is, in $H_2$ edge effects become larger than $H_{100}$. In this sense, $J_{ab}^{(3)}$ values in Ising model of the cluster model $H_{100}$ and the pbc-$H_2$ become the similar values.

### 9.4.2 Discussion on $H_4$ and pbc-$H_4$ Models

I finally examined the various $J_{ab}$ interaction in $H_4$ and pbc-$H_4$ models using total energies of the HS and the BS LS solutions.

On dealing with the spin operator of Eq. 8.1 as a classical spin, spin unprojected $J_{ab}$ values for four spin sites are given by the following equation,

$$E = -2(JS_aS_b + J'S_bS_b + JS_cS_d + J''S_aS_c + J''S_bS_d) \tag{9.8}$$

where $S_x$ (x = a, b, c, d) denotes the spin magnitude. When four spin sites have (a, b, c, d) = (↑ ↑ ↑ ↑) spin alignment, Eq 9.8 becomes,

$$E^a = -J - \frac{1}{2}J' - J''. \tag{9.9}$$

Similarly, (a, b, c, d) = (↑ ↓ ↑ ↓):

$$E^b = J + \frac{1}{2}J' - J''. \tag{9.10}$$

(a, b, c, d) = (↑ ↓ ↓ ↑):

$$E^c = J - \frac{1}{2}J' + J''. \tag{9.11}$$

(a, b, c, d) = (↑ ↑ ↓ ↓):

$$E^d = -J + \frac{1}{2}J' + J''. \tag{9.12}$$

From Eqs 9.9 - 9.12, I simply obtained

$$J = \frac{E_b - E_d + E_c - E_a}{4}, \tag{9.13}$$

$$J' = \frac{E_d - E_c + E_b - E_a}{2}, \tag{9.14}$$

$$J'' = \frac{E_c - E_a - E_b + E_d}{4}. \tag{9.15}$$

The various $J_{ab}$ values were summarized in Table 1. Especially, it is often seen around 1.4 Å. This interatomic distance is a bifurcation point as mentioned section 9.2.1. For $H_4$, $J$ and $J'$ values are almost equal in the region III but the values are different each other in the region I. Edge effects becomes smaller as the interatomic distance is longer. $J$ and $J''$ values are different for $H_4$, so that it is found that a long-distance interaction between spin sites is important. On the other hand, for pbc-$H_4$, $J$ values are twice as large as $J'$ ones although these should be equal to each other because the edge effects do not exist in the PBC. The differences of $J$ and $J''$ values are a long-distance interaction illustrated in Figure 9.2(b). The difference between $J'$ values of non-PBC and PBC calculation stems from the model Hamiltonian. I have to construct more appropriate Hamiltonian to estimate $J'$ values quantitatively. On the other hand $J$ values of non-PBC and PBC models are almost same in the region III.

Table 9.1: *J*, *J*′ and *J*″ values calculated with and without the periodic boundary conditions. Calculation methods are UHF, UBLYP, UB3LYP and UBHandHLYP.

a) $H_4$ cluster model

| | UHF | | | UBLYP | | | UB3LYP | | | UBHandHLYP | | |
|---|---|---|---|---|---|---|---|---|---|---|---|---|
| Distance[a] | $J^b$ | $J'^b$ | $J''^b$ | $J^b$ | $J'^b$ | $J''^b$ | $J^b$ | $J'^b$ | $J''^b$ | $J^b$ | $J'^b$ | $J''^b$ |
| 0.8 | −49746.8 | −99493.7 | −49746.8 | −59719.3 | −98443.6 | −49221.8 | −54447.8 | −108895.7 | −54447.8 | −54403.1 | −108806.3 | −54403.1 |
| 1.0 | −34761.5 | −69522.9 | −34761.5 | −45994.7 | −69347.0 | −34673.5 | −40073.1 | −80146.1 | −40073.1 | −39660.9 | −79321.7 | −39660.9 |
| 1.2 | −22060.9 | −44121.8 | −21370.1 | −34442.8 | −44140.4 | −22070.2 | −27746.6 | −55493.3 | −27746.6 | −26933.8 | −53867.5 | −26933.8 |
| 1.4 | $MH^c$ | $H^c$ | $H^c$ | $H^c$ | $H^c$ | $H^c$ | $H^c$ | $H^c$ | $H^c$ | $H^c$ | $H^c$ | $H^c$ |
| 1.6 | −10098.5 | −10780.2 | −1850.9 | −19941.8 | −9044.6 | −4193.8 | $H^c$ | $H^c$ | $H^c$ | $H^c$ | $H^c$ | $H^c$ |
| 1.8 | −5805.4 | −5962.0 | −562.5 | −12194.9 | −6499.9 | −1887.9 | $H^c$ | $H^c$ | $H^c$ | $H^c$ | $H^c$ | $H^c$ |
| 2.0 | −3249.9 | −3308.5 | −182.6 | −6841.5 | −5352.2 | −784.7 | −5646.5 | −5986.6 | −926.7 | −5277.3 | −5343.6 | −568.2 |
| 2.2 | −1797.5 | −1819.3 | −59.6 | −3700.8 | −4116.7 | −514.1 | −3424.3 | −3455.6 | −259.3 | −3145.0 | −3154.9 | −180.3 |
| 2.4 | −986.1 | −993.5 | −19.1 | −1903.8 | −3124.0 | −512.3 | −2044.2 | −2049.2 | −79.0 | −1870.6 | −1871.7 | −58.4 |
| 2.6 | −537.8 | −540.0 | −5.9 | −872.7 | −2449.9 | −556.3 | −1225.9 | −1226.2 | −24.7 | −1117.1 | −1116.4 | −18.9 |
| 2.8 | −291.9 | −292.5 | −1.7 | −271.4 | −2018.7 | −591.6 | −739.9 | −739.4 | −7.8 | −669.7 | −668.9 | −6.0 |
| 3.0 | −157.6 | −157.7 | −0.5 | 84.8 | −1741.4 | −611.6 | −448.1 | −447.6 | −2.5 | −401.7 | −401.2 | −1.9 |
| b) $H_4$ with the periodic boundary conditions | | | | | | | | | | | | |
| 1.2 | −32110.3 | −64220.6 | −29506.5 | −38745.7 | −77491.4 | −38584.2 | −38101.3 | −76202.7 | −37772.3 | −37237.6 | −74475.3 | −36367.9 |
| 1.4 | $H^c$ | $H^c$ | $H^c$ | $H^c$ | $H^c$ | $H^c$ | −24155.5 | −48310.9 | −23546.5 | −23221.6 | −46443.1 | −21513.9 |
| 1.6 | −10661.3 | −21322.6 | −3819.3 | $H^c$ | $H^c$ | $H^c$ | −15261.4 | −30522.8 | −13964.6 | −14406.7 | −28813.4 | −11211.6 |
| 1.8 | −5987.2 | −11974.5 | −1167.4 | −10128.2 | −20256.3 | −8928.8 | −9490.3 | −18980.7 | −6919.8 | −8798.5 | −17596.9 | −3400.1 |
| 2.0 | −3318.0 | −6636.1 | −373.9 | $H^c$ | $H^c$ | $H^c$ | −6075.1 | −10990.7 | −1619.9 | −5284.1 | −10568.1 | −1138.3 |
| 2.2 | −1821.8 | −3643.7 | −120.8 | $H^c$ | $H^c$ | $H^c$ | −3475.2 | −6950.4 | −556.3 | −3143.5 | −6287.0 | −360.8 |
| 2.4 | −994.0 | −1988.0 | −38.4 | −2306.3 | −4612.7 | −229.1 | −2078.6 | −4157.1 | −169.1 | −1868.9 | −3737.7 | −116.4 |
| 2.6 | −540.1 | −1080.2 | −11.8 | −1397.1 | −2794.3 | −64.4 | −1247.7 | −2495.4 | −52.4 | −1115.6 | −2231.2 | −37.5 |
| 2.8 | −292.5 | −585.0 | −3.4 | −853.1 | −1706.2 | −18.8 | −753.1 | −1506.2 | −16.3 | −668.7 | −1337.3 | −11.9 |
| 3.0 | −157.7 | −315.3 | −0.9 | −523.5 | −1047.0 | −5.6 | −455.9 | −911.7 | −5.1 | −401.0 | −802.0 | −3.8 |

## 9.5 Conclusion

I investigated differences of $J_{ab}$ values of $[\mathrm{H}]_n$ (n = 2, 4, 100) cluster models and pbc-$\mathrm{H}_n$ (n = 2, 4) models based on the periodic boundary conditions. To my knowledge, this is a first report of quantitative calculation for difference of Jab value with and without the periodic boundary conditions. In Ising model $J_{ab}^{(3)}$ values of pbc-$\mathrm{H}_2$ are almost equal to that of $\mathrm{H}_{100}$. Also, for $\mathrm{H}_4$, $J$, $J''$ values with and without the PBC are almost equal to each other as edge effects become small or a long-distance interaction becomes smaller. These calculated results strongly indicated that $J_{ab}$ values of cluster model were quite similar to ones of PBC calculations in region III. In this sense, I can demonstrate that the use of cluster model for the calculations of $J_{ab}$ values in reasonable.

# Part VI

# General Conclusion

# Chapter 10

# General Conclusion

In this thesis, I described the electron conductivity calculation method for open-shell molecules, and I applied the developed method to the following various systems; i) the extended metal atom chain (EMAC) complex, the problems on the connection the electrodes and the molecules and the artificial metal-DNA. In the artificial metal-DNA, there is the report on the magnetism, so that I studied the magnetism for the system.

In chapter 4, I described the derivation of the developed method. In order to define the model Hamiltonian, I think the electrode-molecule-electrode system. Whole Hamiltonian is divided in three Hamiltonian ( left electrode, molecule and right electrode). I introduce the spin index in order to describe the open-shell system. This view is to split $\alpha$ and $\beta$ electrons into two different orbitals. Assuming that the electrodes directly intact with the end-site of the molecule only, the transition matrix element can be given simply. For the estimation of the interaction between the electrodes and the molecule, I referred to the Luo′ idea. This idea is that the occupied orbitals of the electrodes interact with LUMO of the molecule according to the frontier orbital theory. However, in their idea, there is the problem. Their idea strongly depends on the LUMO, so if there is the generating LUMO, it gives an unsuitable result. In order to resolve it, I extended to the generating LUMO using the Boltzmann distribution.

In chapter 5, I investigated the validity of the developed method for the EMAC complex containing 5 nickels. In this molecule, the LUMO and LUMO+1 are generating, so that it needs using the method based on the Boltzmann distribution. The calculated results are close to the experimental results. However, considering the LUMO only, the calculated current value is considerably different from the experimental result.This indicates that the method based on the Boltzmann distribution is useful for the generating LUMO.

In chapter 6, I investigated the effect on the connection between the electrodes and the molecule.

In general, the interaction is interpreted as the electron coupling between the electrodes and the end-site atom of the molecule. It is well-known the the electron coupling strongly depends on the distance between the electrode and the end-site atom of the molecule. In calculated results, the spin polarization stems when the distance between the electrode and the end-site is longer. The electron conductivity becomes small if the spin generates on the end-site.

In chapter 7, I investigated the current-voltage *I-V* characteristics between adjacent bases in two types of artificial metal-DNA (M-DNA) models, i.e. hydroxypyridone (= 2-methyl-3-hydroxy-4-pyridone, **H**) and salen (= N,N' -bis(salicylidene)ethylenediamine, **S**) complexes, using an elastic scattering Green's function method together with a density functional theory. In order to estimate quantitative behaviors of the *I-V* characteristics of the artificial M-DNAs, I considered *I-V* characteristics from the following several viewpoints: the effect of spin states, the effect of backbone and the effect of metal ions. I have found that the magnitude of the current of the **H** complex tends to become larger than that of the **S** complex. I also found that a difference in the spin states drastically changes the *I-V* characteristics. These behaviors suggest the possibility of the control of the *I-V* characteristics in the artificial M-DNA by an external magnetic field.

In chapter 8, The origin of a ferromagnetic interaction between $Cu^{2+}$ ions in the $Cu^{2+}$-DNA system which reported by Tanaka el. al. is examined by using DFT calculations. The calculated results show that $J_{ab}$ values are weak anti-ferromagnetic couplings. Boltzmann distribution simulation indicates that the high spin (HS) species exist 21% at 1.5K by thermal excitation within the model structure. The magnetic and other physical properties between $Cu^{2+}$ ions coordinated by salen-base pairs ($Cu^{2+}$-DNA) are examined by using DFT calculations. The calculated results show that $J_{ab}$ values are weak anti-ferromagnetic couplings, and agreed with experimental results presented by Clever et al.

In chapter 9, $J_{ab}$ values calculated by cluster models were compared with values calculated under the periodic boundary conditions. So far, to estimate the $J_{ab}$ value of a macro system, I have considered that of the corresponding to cluster one. However, they will get absolutely nothing out of it if a cluster model and the periodic boundary conditions method give different results to us. The main aim of this report is to give an opinion to this issue using a one-dimensional polyhydrogen system as example.

This thesis would lead to the understanding the knowledge of the electron conductivity for open-shell molecules, and I hope this thesis will be help for the development in material science.

# References

[1] A. Aviram and M. A. Ratner, *Chem. Phys. Lett.*, **29**, 277 (1974).

[2] M. A. Reed, C. Zhou, C. J. Muller, T. P. Burgin, J. M. Tour, *Science*, **278**, 252 (1997).

[3] J. Reicher, R. Ochs, D. Bechmann, H. B. Weber, M. Mayor, H. V. Lohneysen, *Phys. Rev. Lett.*, **88**, 153901 (2005).

[4] X. Xiao, B. Xu, N. J. Tao, *Nano Lett.*, **4**, 1105 (2004).

[5] M. Dorogi, J. Gomez, R. P. Andres, R. Reifenberger, *Phys. Rev. B*, **52**, 9071 (1995).

[6] R. P. Andres, T. Bein, M. Dorogi, S. Feng, J. I. Henderson, C. P. Kubiak, W. Mahoney, R. G. Osifchin, R. Reifenberger, *Science*, **272**, 1323 (1996).

[7] H. Kondo, H. Kino, J. Nara, T. Ozaki, T. Ohno, *Phys. Rev. B*, **73**, 235323 (2006).

[8] C. Yin, G. C. Huang, C. K. Kuo, M. D. Fu, H. C. Lu, J. H. Ke, K. N. Shih, Y. L. Huang, G. H. Lee, C. Y. Yeh, C. H. Chen, S. M. Peng, *J. Am. Chem. Soc.*, **130**, 10090 (2008).

[9] C. J. Murphy, M. R. Arkin, Y. Jenkins, N. D. Ghatlia, S. H. Bossman, N. J. Turro, J.K. Barton, *Science*, **262**, 1025 (1993).

[10] D. B. Hall, R. E. Holmlin, J. K. Barton, *Nature*, **82**, 731 (1996).

[11] O. K. Shana, J. K. Barton, *Science*, **283**, 375 (1999).

[12] P. J. Dandliker, R. E. Holmlin, J. K. Barton, *Science*, **275**, 1465 (1997).

[13] Y. Zhang, R. H. Austin, J. Kraeft, E.C. Cox, N. P. Ong, *Phys. Rev. Lett.*, **89**, 198102 (2002).

[14] F. D. Lewis, T. Wu, Y. Zhang, R. L. Letsinger, S. R. Greenfield, W. R. Wasielewski, *Science*, **277**, 673 (1997).

[15] M. R. Arkin, E. D. A. Stemp, R. E. Holmlin, J. K. Barton, A. Hörmann, E. J. C. Olson, P. F. Barbara, *Science*, **273**, 475 (1996).

[16] D. Porath, S. Bezryadin, S. D. Vries, C. Dekker, *Nature*, **403**, 635 (2000).

[17] Y. D. Kasumov, M. Kociak, S. Gueron, B. Reulet, V. T. Volkov, D. V. Klinov, H. Bouchiat, *Science*, **291**, 280 (2001).

[18] T. Tada, M. Kondo, K. Yoshizawa, *ChemPhysChem.*, **4**, 1256 (2003).

[19] P. J. De Pablo, F. Moreno-Herrero, J. Colchero, J. G. Herrero, P. Herrero, A. M. Baro, P. Ordejon, J. M. Soler, E. Artacho, *Phys. Rev. Lett.*, **85**, 4992 (2000).

[20] K. Tanaka, A. Tengeiji, T. Kato, N. Toyama, M. Shionoya, *Science*, **299**, 1212, (2003).

[21] G. H. Clever and T. Carell, *Angew. Chem., Int. Ed.*, **46**, 250 (2007).

[22] H. A. Wagenknecht, *Angew. Chem. Int. Ed.*, **42**, 3204 (2003).

[23] A. Szabo and N. S. Ostlund, *Modern Quantum Chemistry*, Dover, (1996).

[24] T. Koopmans, *Physica*, **1**, (1934).

[25] C. C. J. Roothaan, *Rev. Mod. Phys.*, **23**, 69 (1951).

[26] J. A. Pople and R. K. Nesbet, *J. Chem. Phys*, **22**, 571 (1954).

[27] R. G. Parr and W. Yang, *Density-Functional Theory of Atoms and Molecules*, Oxford Science Publications (1989).

[28] C. Fiolhais, F. Nogueira, M. Marques, *A primer in density functional theory*, Springer (2003).

[29] M. Reiher, *Atomistic approaches in modern biology: from quantum chemistry to molecular*, Springer (2007).

[30] L. H. Thomas, *Proc. Camb. phil. Soc.*, **23**, 542 (1927).

[31] E. Fermi, *Rend. Accad. Lincei.*, **6**, 602 (1927).

[32] P. A. M. Dirac, *Proc. Camb. phil. Soc.*, **26**, 376 (1930).

[33] P. Hohenberg and W. kohn, *Phys. Rev.*, **136**, B864, (1964).

[34] M. Levy, *Proc. Natl. Acad. Sci. USA*, **76**, 6062, (1979).

[35] M. Levy, *Phys. Rev. A*, **26**, 1200, (1982).

[36] W. Kohn and L. J. Sham, *Phys. Rev.*, **140**, A1133, (1965).

[37] C. Lee, W. Yang, R. G. Parr, *Phys. Rev. B*, **37**, 785 (1988).

[38] A. D. Becke, *J. Chem. Phys*, **98**, 5648, (1993).

[39] A. D. Becke, *Phys. Rev. A*, **38**, 3098 (1988).

[40] S. H. Vosko, L. Wilk, and M. Nusair, Can. *J. Phys.*, **58**, 1200 (1980).

[41] V. Balzani, M. Credi, M. Venturi, *Molecular Devices and Machines*, Cambridge (2003).

[42] S. Datta, *Electronic transport in mesoscopic systems*, Cambridge University Press (1995).

[43] S. Datta, *Quantum transport: atom to transistor*, Cambridge University Press (2005).

[44] R. Landauer, IBM *J. Res. Dev.*, **1**, 223 (1957).

[45] C. J. Muller, J. M. van Ruitenbeek, L. J. de Jongh, *Physica C*, **191**, 485 (1992).

[46] J. Ulrich, D. Esrail, W. pontius, L. Venkataramen, D. Millar, L. H. Doerrer, *J. Phys. Chem. B*, **110**, 2462 (2006).

[47] S. Ghosh, H. Hamimun. A. K. Mahapatro, J. Choi, S. Lodha, D. Janes, *Appl. Phys. Lett.*, **87**, 233509 (2005).

[48] M. Tsutsui, Y. Teramae, S. Kurokawa, A. Sakai, *Appl. Phys. Lett.*, **89**, 163111 (2006).

[49] C. Joachim, J. K. Gimzewski, A. Aviram, *Nature*, **408**, 541 (2000).

[50] C. Joachim, J. K. Gimzewski, R. R. Schlittler, C. Chavy, *Phys. Rev. Lett.*, **74**, 2102 (1995).

[51] C. Kergueris, J. P. Bourgoin, S. Palacin, D. Esteve, C. Urbina, M. Magoga, C. Joachim, *Phys. Rev. B*, **59**, 12505 (1999).

[52] E. Coronado, J. R. Galan-Mascaros, C. J. Gomez-Garcia, V. Laukhin, *Nature*, **408**, 447 (2000).

[53] M. Matsushita, H. Kawakami, Y. Kawada, T. Sugawara, *Chem. Lett.*, **36**, 110 (2007).

[54] V. Mujica, G. Doyen, *Int. J. Quantum Chem., Quantum Chem. Symp.*, **27**, 687 (1993).

[55] V. Mujica, M. Kemp, M. A. Ratner, *J. Chem. Phys.*, **101**, 6849 (1994).

[56] V. Mujica, M. Kemp, M. A. Ratner, *J. Chem. Phys.*, **101**, 6856 (1994).

[57] C. K. Wang, Y. Fu, Y. Luo, *Phys. Chem. Chem. Phys.*, **3**, 5017 (2001).

[58] Y. Luo, C. K. Wang, Y. Fu, *J. Chem. Phys.*, **117**, 10283 (2002).

[59] L. L. Lin, J. C. Leng, X.N. Song, Z. L. Li, Y. Luo, C. K. Wang, *J. Phys. Chem. C*, **113**, 14474 (2009).

[60] E. N. Economou, *Green' Function in Quantum Physics*, Springer, (1990).

[61] J. R. Taylor, *Scattering Theory*, Wiley, (1972).

[62] A. S. Davidov, *Quantum Mechanics*, NEO, (1966).

[63] D. M. Newns, *Phys. Rev.*, **178**, 1123 (1996).

[64] T. Dittrich, P. Hänggi, G.L. Ingold, B. Kramer, G. Schön, W. Zwerger, *Quantum Transport and Dissipation*, Wiley-VCH, (1998).

[65] M. Dewar, *Bull. Soc. Chim. France*, **18**, C79 (1951).

[66] J. Chatt and L. Duncanson, *J. Chem. Soc.*, 2939 (1953).

[67] S. Y. Lai, T. W. Lin, Y. H. Chen, C. C. Wang, G. H. Lee, M. H. Yang, M. K. Leung, S. M. Peng, *J. Am. Chem. Soc.*, **121**, 250 (1999).

[68] C. C. Wang, W. C. Lo, C. C. Chou, G. H. Lee, J. M. Chen, S. M. Peng, *Inorg. Chem.*, **37**, 4059 (1998).

[69] F. A. Cotton, T. R. Felthpuse, *Inorg. Chem.*, **19**, 328 (1980).

[70] F. A. Cotton, T. R. Felthpuse, *Inorg. Chem.*, **20**, 600 (1981).

[71] F. A. Cotton, X. Feng, P. A. Kibala, M. Matusz, *J. Am. Chem. Soc.*, **110**, 2807 (1998).

[72] F. A. Cotton, Y. Kim, T. Ren. *Inorg. Chem.*, **31**, 2723 (1992).

[73] F. A. Cotton, Y. Kim, T. Ren, *Polyhedron*, **12**, 607 (1993).

[74] J. K. Bera, K. R. Dunbar, *Angew Chem. Int. Ed.*, **41**, 23 (2002).

[75] K. Mashima, M. Tanaka, T. Tani, A. Nakamura, S. Takeda, W. Mori, K. Yamaguchi, *J. Am. Chem. Soc.*, **119**, 4307 (1997).

[76] S. M. Peng, C. C. Wang, Y. L. Jang, Y. H. Chen, F. Y. Li, C. Y. Mou, M. K. Leung, *J. Magn. Magn. Mater.*, **209**,80 (2000).

[77] Y. Kitagawa, M. Shoji, K. Koizumi, T. Kawakami, M. Okumura, K. Yamaguchi, *Polyhedron*, **24**, 2751 (1995).

[78] E. C. Yang, M. C. Cheng, M. C. Tsai, M. S. Peng, *J. Chem. Soc., Chem. Commun.*, 2377 (1994).

[79] J. T. Sheu, C. C. Liu, I. Chao, C. C. Wang, S. M. Peng, *Chem. Commun.*, 315 (1996).

[80] I. W. P. Chen, M. D. Fu, W. H. Tseng, J. Y. Yu, S. H. Wu, C. J. Ku, C. H. Chen, S. M. Peng, *Angew. Chem. Int. Ed.*, **45**, 5814 (2006).

[81] L. Y. Hsu, Q. R. Huang, B. Y. Jin, *J. Phys. Chem. C*, **112**, 10538 (2008).

[82] M. J. Frisch, G. W. Trucks, H. B. Schlegel, G. E. Scuseria, M. A. Rob, J. R. Cheeseman, J. A. Montgomery Jr., T. Vreven, K. N. Kudin, J. C. Burant, J. M. Millam, S. S. Iyengar, J. Tomasi, V. Barone, B. Mennucci, M. Cossi, G. Scalmani, N. Rega, G. A. Petersson, H. Nakatsuji, M. Hada, M. Ehara, K. Toyota, R. Fukuda, J. Hasegawa, M. Ishida, T. Nakajima, Y. Honda, O. Kitao, H. Nakai, M. Klene, X. Li, J. E. Knox, H. P. Hratchian, J. B. Cross, V. Bakken, C. Adamo, J. Jaramillo, R. Gomperts, R. E. Stratmann, O. Yazyev, A. J. Austin, R. Cammi, C. Pomelli, J. W. Ochterski, P. Y. Ayala, K. Morokuma, G. A. Voth, P. Salvador, J. J. Dannenberg, V. G. Zakrzewski, S. Dapprich, A. D. Daniels, M. C. Strain, O. Farkas, D. K. Malick, A. D. Rabuck, K. Raghavachari, J. B. Foresman, J. V. Ortiz, Q. Cui, A. G. Baboul, S. Clifford, J. Cioslowski, B. B. Stefanov, G. Liu, A. Liashenko, P. Piskorz, I. Komaromi, R. L. Martin, D. J. Fox, T. Keith, M. A. Al-Laham, C. Y. Peng, A. Nanayakkara, M. Challacombe, P. M. W. Gill, B. Johnson, W. Chen, M. W. Wong, C. Gonzalez, and J. A. Pople, Gaussian 03, Revision D.02. Gaussian, Inc., Wallingford, CT, 2004.

[83] Z. Huang, F. Chen, P. A. Bennett, N. Tao, *J. Am. Chem. Soc.*, 129, 13225, (2007).

[84] Y. Qi, J. Qin, G. Zhang, T. Zhang, *J. Am. Chem. Soc.*, 131, 16418, (2009).

[85] I. L. Zilberberg, V. I. Avdeev, G. M. Zhidomirov, *THEOCHEM*, **418**, 73 (1997).

[86] N. S. Hush, J. Schamberger, G. B. Bacskay, Coord. *Chem. Rev.*, **249**, 299 (2005).

[87] T. Matsui, Y. Shigeta, K. Hirao, *Chem. Phys. Lett.*, **423**, 331 (2006).

[88] T. Matsui, Y. Shigeta, K. Hirao, *J. Phys. Chem. B*, **111**, 1176 (2007).

[89] K. Tanaka, A. Tengeiji, T. Kato, N. Toyama, M. Shiro, M. Shionoya, *J. Am. Chem. Soc.* **124**, 12494, (2002).

[90] T. Kawakami, T. Taniguchi, T. Hamamoto, Y. Kitagawa, M. Okumura, K. Yamaguchi, *Int. J.Quantum Chem.*, **105**, 655 (2005).

[91] H. Y. Zhang, A. Calzolari, R. D. Felice, *J. Phys. Chem. B*, **109**, 15345 (2005).

[92] R. A. Jishi, J. Bragin, *J. Phys. Chem. B*, **111**, 5357 (2007).

[93] Y. Nakanishi, Y. Kitagawa, Y. Shigeta, T. Saito, T. Matsui, H. Miyachi, T. Kawakami, M. Okumura, K. Yamaguchi, *Polyhedron*, **28**, 1714 (2009).

[94] S. S. Mallajosyula and S. K. Pati, *Phys. Rev. Lett.*, **98**, 136601 (2007).

[95] T. Matsui, H. Miyachi, T. Sato, Y. Shigeta, K. Hirao, *J. Phys. Chem. B*, **112**, 16960 (2008).

[96] Y. Anderson, D. C. Langreth, B. I. Lundqvist, *Phys. Rev. Lett.* **76**, 102 (1996).

[97] G. H. Clever, K. Polborn, T. Carell, *Angew. Chem., Int. Ed.*, **44**, 7204, (2005).

[98] Y. Nakanishi, Y. Kitagawa, Y. Shigeta, T. Saito, T. Matsui, H. Miyachi, T. Kawakami, M. Okumura, K. Yamaguchi, *Polyhedron*, **28**, 1945 (2009).

[99] S. S. Mallajosyula and S. K. Pati, *Angew. Chem. Int. Ed.*, **48**, 4977 (2009).

[100] G. H. Clever, S. J. Reitmeier, T. Carell, O. Schiemann, *Angew. Chem. Int. Ed.*, 2010, in press.

[101] G. H. Clever and M. Shionoya, *Coord. Chem. Rev.*, 2010, in press.

[102] K. Tanaka, G. H. Clever, Y. Takezawa, Y. Yamada, C. Kaul, M. Shionoya, T. Carell, *Nat.Nanotechnol.*, **1**, 190 (2006).

[103] Y. Takezawa, W. Maeda, K. Tanaka, M. Shionoya, *Angew. Chem. Int. Ed.*, **48**, 1081 (2009).

[104] J. Müller, D. Böhme, P. Lax, M. M. Cerda, M. Roitzsch, *Chem. Eur. J.*, **11**, 6246 (2005).

[105] Y. Takezawa, K. Tanaka, M. Yori, S. Tashiro, M. Shiro, M. Shionoya, M. *J. Org. Chem.*, **73**, 6092 (2008).

[106] F. A. Polonius and J. Müller, *Angew. Chem.*, **119**, 5698 (2007).

[107] F. A. Polonius and J. Müller, *Angew. Chem. Int. Ed.*, **46**, 5602 (2007).

[108] N. Zimmermann, E. Meggers, P. G. Schultz, *J. Am. Chem. Soc.*, **124**, 13684 (2002).

[109] S. S. Mallajosyula and S. K. Pati, *J. Phys. Chem. Lett.*, **1**, 1881 (2010).

[110] F. L. Gervasio, P. Carloni, M. Parrinello, *Phys. Rev. Lett.*, **89**, 108102 (2002).

[111] G. H. Clever, Y. Söltl, H. Burks, W. Spahl, T. Carell, *Chem. Eur. J.*, **12**, 8708 (2006).

[112] Y. Nakanishi, T. Matsui, Y. Shigeta, Y. Kitagawa, T. Saito, Y. Kataoka, T. Kawakami, M. Okumura, K. Yamaguchi, *Int. J. Quantum Chem.*, **110**, 2221 (2010).

[113] Y. Shigeta, T. Kawakami, H. Nagao, K. Yamaguchi, *Chem. Phys. Lett.*, **315**, 441 (1999).

[114] H. Tatewaki and S. Huzinaga, *J. Chem. Phys.*, **72**, 339 (1980).

[115] J. W. Steed, J. L. Atwood, *Supermolecular Chemistry*, Chichester (2000).

[116] K. Mizoguchi, S. Tanaka, T. Ogawa, N. Shiobara, H. Sakamoto, *Phys. Rev. B*, **72**, 033106, (2005).

[117] K. Yamaguchi, *Self-Consistent Field Theory and Applications*, Elsevier, p.727 (1990).

[118] T. Kawakami, S. Yamanaka, S. Yamada, W. Mori, K. Yamaguchi, *Molecular-based Magnetic Materials, Theory, Technique and Applications*, American Chemical Society, **644**, p.30 (1996).

[119] Y. Kitagawa, T. Soda, Y. Shigeta, S. Yamanaka, Y. Yoshioka, K. Yamaguchi, *Int. J. Quantum Chem.*, **84**, 592 (2001).

[120] A. D. Becke, *J. Chem. Phys.*, **98**, 1372, (1993).

[121] J. P. Perdew, J. A. Chevary, S. H. Vosko, K. A. Jackson, M. R. Pederson, D. J. Singh, C. Fiolhais, *Phys. Rev. B*, **46**, 6671, (1992).

[122] C. Adamo and V. Barone, *J. Chem. Phys.*, **116**, 5933 (2002).

[123] M. Head-Gordon, J. A. Pople, M. J. Frisch, *Chem. Phys. Lett.*, **153**, 503 (1988).

[124] W. Saenger, *Principles of Nucleic Acid Structure*, Springer (1984).

[125] Y. Kitagawa, T. Kawakami, Y. Yoshioka, K. Yamaguchi, *Polyhedron*, **20**, 1189 (2001).

[126] S. Tsuzuki, T. Uchimaru, K. Matsumura, M. Mikami, K. Tanabe, *Chem. Phys. Lett.*, **319**, 547 (2000).

[127] S. Tsuzuki, K. Honda, T. Uchimaru, M. Mikami, K. Tanabe, *J. Am. Chem. Soc.*, **124**, 104 (2001).

[128] S. Nakano, Y. Kitagawa, T. Kawakami, M. Okumura, H. Nagao, K. Yamaguchi, *Molecules*, **9**, 792 (2004).

[129] S. Tsuzuki, T. Uchimaru, K. Matsumura, M. Mikami, K. Tanabe, *Chem. Phys. Lett.*, **319**, 547 (2000).

[130] S. Tsuzuki, K. Honda, T. Uchimaru, M. Mikami, K. Tanabe, *J. Am. Chem. Soc.*, **124**, 104 (2001).

[131] N. C. Seeman, *Nature*, **421**, 427 (2003).

[132] C. Bellitto, G. Dessy, V. Fares, *Inorg. Chem.*, **24**, 2815 (1985).

[133] H. Kitagawa, N. Onodeta, T. Sonoyama, M. Yamamoto, T. Fukawa, T. Mitani, M. Seto, Y. Maeda, *J. Am. Chem. Soc.*, **121**, 10068 (1999).

[134] M. Yamashita, Y. Wada, K. Toriumi, T. Mitani, *Mol. Cryst. Liq.*, **216**, 207 (1992).

[135] Y. Kitagawa, M. Ito, Y. Nakanishi, T. Saito, S. Yamada, T. Kawakami, M. Okumura, K. Yamaguchi, *Polyhedron*, **28**, 1668 (2009).

[136] T. Kawakami, S. Yamanaka, Y. Takano, Y. Yoshioka, K. Yamaguchi, *Bull. Chem. Soc. Jpn.*, **71**, 2097, (1998).

[137] A. D. Becke, *Phys. Rev. A*, **38**, 3098 (1998).

[138] A. D. Becke, *J. Chem. Phys.*, **98**, 1372 (1993).

[139] R. R. Dovesi, et al. CRYSTAL 2006 User's Manual; University of Torino: Torino (2006).

# Publication List

## Main Papers

1. Y. Nakanishi, Y. Kitagawa, Y. Shigeta, T. Saito, T. Matsui, H. Miyachi, T. Kawakami, M. Okumura, K. Yamaguchi, Theoretical studies on magnetic interactions between Cu(II) ions in hydroxypyridone nucleobases, *Polyhedron*, **28**, 1714-1717 (2009).
2. Y. Nakanishi, Y. Kitagawa, Y. Shigeta, T. Saito, T. Matsui, H. Miyachi, T. Kawakami, M. Okumura, K. Yamaguchi, Theoretical studies on magnetic interactions between Cu(II) ions in salen nucleobases, *Polyhedron*, **28**, 1945-1949 (2009).
3. Y. Nakanishi, Y. Kitagawa, T. Saito, Y. Kataoka, T. Matsui, T. Kawakami, M. Okumura, K. Yamaguchi, Estimation of effective exchange integral value of polyradical systems based on the band calculation, *Int. J. Quant. Chem.*, **109**, 3632-3640 (2009).
4. Y. Nakanishi, T. Matsui, Y. Shigeta, Y. Kitagawa, T. Saito, Y. Kataoka, T. Kawakami, M. Okumura, K. Yamaguchi, Sequence-Dependent Proton-Transfer Reaction in Stacked GC Pair III: The Influence of Proton Transfer to Conductivity, *Int. J. Quant. Chem.*, **110**, 2221-2230 (2010).
5. Y. Nakanishi, T. Matsui, Y. Kitagawa, Y. Shigeta, T. Saito, Y. Kataoka, T. Kawakami, M. Okumura, K. Yamaguchi, Electron Conductivity in Modified Models of Artificial Metal-DNA using Green's Function-Based Elastic Scattering Theory, *Bull. Chem. Soc. Jpn.*, accepted.

## Others

1. M. Yano, Y. Nakanishi, K. Matsushita, M. Tatsumi, M. Oyama, K. Sato, T. Takui, Organic high-spin systems of oligoarylamines: Properties of tetraaryl-m-phenylendiamine oligocations as examined by electron transfer stopped-flow method, *Polyhedron*, **24**, 2116-2120 (2005).
2. Y. Kitagawa, T. Saito, Y. Nakanishi, M. Ito, M. Shoji, K. Koizumi, S. Yamanaka, T. Kawakami, M. Okumura, K. Yamaguchi, Geometry Optimization without Spin Contamination Error - Approximately Spin Projected Optimization Method -, *AIP conference proceedings*, **963**, 334-337 (2007).
3. T. Saito, Y. Kitagawa, M. Shoji, Y. Nakanishi, M. Ito, T. Kawakami, M. Okumura, K. Yamaguchi, Theoretical studies on the structure and effective exchange integral (Jab) of an active site in oxyhemocyanin (oxyHc) by using approximately spin-projected geometry optimization (AP-opt) method, *Chem. Phys. Lett.*, **456**, 76-79 (2008).

4. Y. Kitagawa, M. Shoji, T. Saito, Y. Nakanishi, K. Koizumi, T. Kawakami, M. Okumura, K. Yamaguchi, Theoretical studies on effects of hydrogen bonds attaching to cysteine ligands on 4Fe-4S clusters, *Int. J. Quant. Chem.*, **108**, 2881-2887 (2008).

5. Y. Kitagawa, Y. Nakanishi, T. Saito, K. Koizumi, M. Shoji, S. Yamada, T. Kawakami, M. Okumura, K. Yamaguchi, Theoretical Study of Magnetic Interaction between $C_{60}$ Anion Radicals, *Polyhedron*, **28**, 1750-1753 (2009).

6. Y. Kitagawa, M. Ito, Y. Nakanishi, T. Saito, S. Yamada, T. Kawakami, M. Okumura, K. Yamaguchi, Theoretical Studies on Electronic Structures and Magnetic Interactions of $K_4[Pt_2(pop)_4X]{\cdot}2H_2O$ (X=Cl, Br) Complexes, *Polyhedron*, **28**, 1668-1671 (2009).

7. Y. Kitagawa, Y. Nakanishi, T. Saito, T. Kawakami, M. Okumura, K. Yamaguchi, BS DFT and BS HDFT studies of Cr-Cr sextuple bond from the viewpoint of electron correlation effects, *Int. J. Quant. Chem.*, **109**, 3315-3324 (2009).

8. S. Takaishi, M. Hosoda, T. Kajiwara, H. Miyasaka, M. Yamashita, Y. Nakanishi, Y. Kitagawa, K. Yamaguchi, A. Kobayashi, H. Kitagawa, Electroconductive Porous Coordination Polymer Cu[Cu(pdt)2] Composed of Donor and Acceptor Building Units, *Inorg. Chem.*, **48**, 9048-9050 (2009).

9. T. Saito, Y. Kataoka, Y. Nakanishi, T. Matsui, Y. Kitagawa, T. Kawakami, M. Okumura, K. Yamaguchi, Theoretical studies on chemical bonding between Cu(II) and oxygen molecule in type 3 copper proteins, *Int. J. Quant. Chem.*, **109**, 3649-3658 (2009).

10. Y. Kitagawa, T. Saito, Y. Nakanishi, Y. Kataoka, M. Shoji, K. Koizumi, T. Kawakami, M. Okumura, K. Yamaguchi, Approximately Spin Projected Hessian for Broken Symmetry Method and Stretching Frequencies of $F_2$ and Singlet $O_2$, *Int. J. Quant. Chem.*, **109**, 3641-3648 (2009).

11. T. Matsui, H. Miyachi, Y. Nakanishi, Y. Shigeta, T. Sato, Y. Kitagawa, M. Okumura, K. Hirao, Theoretical Studies on Sulfur and Metal Cation (Cu(II), Ni(II), Pd(II), and Pt(II))-Containing Artificial DNA, *J. Phys. Chem. B*, **113**, 12790-12795 (2009).

12. T. Saito, S. Nishihara, Y. Kataoka, Y. Nakanishi, T. Matsui, Y. Kitagawa, T. Kawakami, M. Okumura, K. Yamaguchi, Transition state optimization based on approximate spin-projection (AP) method, *Chem. Phys. Lett.*, **483**, 168-171 (2009).

13. Y. Kitagawa, T. Saito, Y. Nakanishi, Y. Kataoka, T. Matsui, T. Kawakami, M. Okumura, K. Yamaguchi, Spin Contamination Error in Optimized Geometry of Singlet Carbene ($^1A_1$) by Broken-Symmetry Method, *J. Phys. Chem. A*, **113**, 15041-15046 (2009).

14. T. Saito, Y. Kataoka, Y. Nakanishi, T. Matsui, Y. Kitagawa, T. Kawakami, M. Okumura, K. Yamaguchi, Which hybrid GGA DFT is suitable for Cu2O2 systems if the spin contamination error is removed?, *Chem. Phys.*, **368**, 1-6 (2010).

15. T. Saito, S. Nishihara, Y. Kataoka, Y. Nakanishi, Y. Kitagawa, T. Kawakami, S. Yamanaka, M. Okumura, K. Yamaguchi, Reinvestigation of the Reaction of Ethylene and Singlet Oxygen by the Approximate Spin Projection Method. Comparison with Multireference Coupled-Cluster Calculations, *J. Phys. Chem. A*, **114**, 7967-7974 (2010).

16. T. Saito, Y. Kataoka, Y. Nakanishi, T. Matsui, Y. Kitagawa, T. Kawakami, M. Okumura, K. Yamaguchi, Theoretical studies of the effect of orientation of ligands and spin contamination error on the chemical bonding in the $FeO_2$ core in oxymyoglobin, *J. Mol. Struct. Theochem*, **954**, 98-104 (2010).

17. Y. Kitagawa, T. Saito, Y. Nakanishi, Y. Kataoka, T. Matsui, T. Kawakami, M. Okumura, K. Yamaguchi, Development of approximately spin projected energy derivatives for biradical systems, *Int. J. Quant. Chem.*, **110**, 3053-3060 (2010).

18. T. Saito, S. Nishihara, Y. Kataoka, Y. Nakanishi, Y. Kitagawa, T. Kawakami, Yamanaka, M. Okumura, K. Yamaguchi, Multireference Character of 1,3-Dipolar Cycloaddition of Ozone with Ethylene and Acrylonitrile, *J. Phys. Chem. A*, **114**, 12116-12123 (2010).